The Versatile Roles of Sulfate-Reducing Bacteria for Uranium Bioremediation

by

Chen Zhou

A Dissertation Presented in Partial Fulfillment
of the Requirements for the Degree
Doctor of Philosophy

Approved March 2014 by the
Graduate Supervisory Committee:

Bruce Rittmann, Chair
Rosa Krajmalnik-Brown
César Torres

ARIZONA STATE UNIVERSITY

May 2014

ABSTRACT

Uranium (U) contamination has been attracting public concern, and many researchers are investigating principles and applications of U remediation. The overall goal of my research is to understand the versatile roles of sulfate-reducing bacteria (SRB) in uranium bioremediation, including direct involvement (reducing U) and indirect involvement (protecting U reoxidation). I pursue this goal by studying *Desulfovibro vuglaris*, a representative SRB. For direct involvement, I performed experiments on uranium bioreduction and uraninite (UO_2) production in batch tests and in a H_2-based membrane biofilm reactor (MBfR) inoculated with *D. vulgaris*. In summary, *D. vulgaris* was able to immobilize soluble U(VI) by enzymatically reducing it to insoluble U(IV), and the nanocrystallinte UO_2 was associated with the biomass. In the MBfR system, although *D. vulgaris* failed to form a biofilm, other microbial groups capable of U(VI) reduction formed a biofilm, and up to 95% U removal was achieved during a long-term operation. For the indirect involvement, I studied the production and characterization of and biogenic iron sulfide (FeS) in batch tests. In summary, *D. vulgaris* produced nanocrystalline FeS, a potential redox buffer to protect UO_2 from remobilization by O_2. My results demonstrate that a variety of controllable environmental parameters, including pH, free sulfide, and types of Fe sources and electron donors, significantly determined the characteristics of both biogenic solids, and those characteristics should affect U-sequestrating performance by SRB. Overall, my results provide a baseline for exploiting effective and sustainable approaches to U bioremediation, including the application of the novel MBfR technology to U sequestration from groundwater and biogenic FeS for protecting remobilization of sequestrated U, as well as the microbe-relevant tools to optimize U sequestration applicable in reality.

ACKNOWLEDGMENTS

The research presented here was supported by Office of Science, U.S. Department of Energy (DOE), Grant No. DE-FG02-09ER64803.

First and foremost, I would like to thank Dr. Bruce Rittmann for the opportunity to conduct this research under his guidance during the past six years in the Swette Center for Environmental Biotechnology (SCEB) in Biodesign Institute, Arizona State University. His vision, personality, and philosophy to be a successful top researcher has been critic in the success of my research, and all of this fostered my personal and professional growth significantly during the past six years.

I am particularly grateful to Dr. Raveender Vannela, the co-principal investigator of the DOE project, for his guidance and contribution that were critical to my preparation of the research proposal and experimental plans, as well as to the completion of my research and thesis.

I would like to thank Drs. Rosa Krajmalnik-Brown and César Torres for accepting to be members of my committee and for the opportunity to obtain advice and feedback from them throughout my graduate study.

I would also like to express my gratitude to the collaborative team of the DOE project in University of Michigan, including Dr. Kim Hayes as the PI, Dr. Sung Pil Hyun, Yuqiang Bi, and Julian Carpenter as the researchers. I have learned a lot from them particularly in mineral characterization.

I am also grateful to Aura Ontiveros-Valencia, a PhD student collaborating with me on the uranium-reducing MBfR project, was a critical asset to the research.

My gratitude is also given to our lab manager, Diane Hagner, for efficiently facilitating and supporting my experiments over years.

I am also indebted to my former professors at Nanjing University, China for "paving the road" for my academic career.

I am honored to acknowledge the help of many people throughout my research, including but not limited to, Dr. Steve Van Ginkel, Dr. Michal Ziv-El, Dr. Prathap Parameswaran, Dr. Youneng Tang, Dr. Jianyong Liu, Dr. Heping Zhao, Dr. Ang Li, Dr. Anca Delgado, Dr. Dae Woo

Kang, Alexander Zevin, Sara Carey, Xiaoyin Xu, Zhuolin Liu, Michelle Young, and all members in SCEB.

Lastly, I want to thank my family and friends for all their support. This research has required me to be away from my wife Jie Pu and my daughter Dorothy. Their understanding and contribution mean too much to me. Our parents and dear friends both in the US and in China provided moral support. All of these together make possible the completion of my graduate study.

TABLE OF CONTENTS

Page

LIST OF TABLES viii

LIST OF FIGURES ix

CHAPTER

1. INTRODUCTION 1

1.1. Uranium in Our Environment 1

1.1.1. Uranium in Nature 1

1.1.2. Physical and Chemical Properties 1

1.1.3. U Applications and Consequent Environmental Contamination 2

1.1.4. Radiological and Chemical Toxicities of Uranium to Human Beings 2

1.1.5. Regulations of Uranium Concentration in Drinking Water 3

1.2. Bioremediation of Uranium in Contaminated Groundwater 4

1.2.1. Fundamental Principle 4

1.2.2. Adsorption and Complexation 4

1.2.3. Reductive Precipitation 5

1.2.4. Drawback: Reoxidation 9

1.3. Iron-sulfide Solids for U Remediation 9

1.3.1. Iron-Sulfide Minerals in Nature 9

1.3.2. Derivation of Iron-Sulfide Minerals 11

1.3.3. Contribution of Iron-Sulfide Solids in U Remediation 112

1.4. Desulfovibrio vulgaris and U Reduction 14

1.4.1. Sulfate-Reducing Microorganisms 13

1.4.2. Desulfovibrio vulgaris 14

1.5. Membrane BioFilm Reactor (MBfR) 17

CHAPTER Page

1.6. Objectives and Organization 18

2. U (VI) REDUCTION BY D. VULGARIS IN BATCH REACTORS 20

2.1. Introduction 20

2.2. Experimental Setup 20

2.2.1. Strain, Growth Medium, and Culturing Conditions 20

2.2.2. Biomass Cuspensions 21

2.2.3. Assay Solution 21

2.2.4. Analytical Methods 22

2.2.5. Separation of Uraninite Solids from Culture Medium 23

2.2.6. Removal and Quantification of Biomass Associated with UO_2 23

2.2.7. XRD Analysis 24

2.2.8. XPS Analysis 24

2.2.9. TEM/EDX Analysis 24

2.2.10. XAS Analysis 25

2.3. Results for U(VI) Reduction and Uraninite Formation 26

2.3.1. U(VI) Alone 26

2.3.2. In Presence/Absence of Sulfate and Soluble Fe(II) 32

2.4. Conclusion 38

3. U(VI) REDUCTION IN A MBFR INOCULATED WITH D. VULGARIS 39

3.1. Introduction 39

3.2. Experimental Setup 39

3.2.1. MBfR Setup 39

3.2.2. Strain, Culturing, and Biomass Preparation 41

3.2.3. Feeding Medium 41

CHAPTER Page

3.2.4. Inoculation, Startup, and Operation 41

3.2.5. Sampling and Analyses 42

3.2.6. Flux Calculation 43

3.2.7. DNA Extraction and Pyrosequencing Analysis 43

3.2.8. Solid Separation and Characterization 43

3.3. Results 44

3.3.1. Stage 1 – U(VI) as the Sole Electron Acceptor 44

3.3.2. Stage 2 – U(VI) and Sulfate as Concomitant Electron Acceptors 47

3.3.3. Solid Characterization of Biofilm Samples 49

3.3.4. Microbial Community Structure of the Biofilm 55

3.4. Conclusion 57

4. BIOGENIC IRON-SULFIDE UNDER VARIOUS CONDITIONS 58

4.1. Introduction 58

4.2. Experimental Setup 58

4.2.1. Strain, Growth Medium, and Culturing Conditions 58

4.2.2. Medium Modification 59

4.2.3. Analytical Methods 61

4.2.4. Separation of Iron-Sulfide Solids from Culture Medium 61

4.2.5. X-Ray Diffraction (XRD) Analysis 62

4.2.6. Stoichiometry Equations for Mass Balance Calculation 62

4.3. Results for Bacteria Growth and Solid Formation 64

4.3.1 Various Lactate-to-Sulfate Mole Rratios 64

4.3.2 Various Iron-to-Sulfate Mole Ratios 68

CHAPTER Page

4.3.3 Various pHs 72

4.3.4 Various Electron Donor Candidates 75

4.4. Summary 79

5. BIOGENIC IRON-SULFIDE FROM VARIOUS IRON SOURCES 80

5.1. Introduction 80

5.2. Experimental setup 80

5.2.1. Strain, Growth Medium, and Culturing Conditions 80

5.2.2. Medium Modification and Iron Sources 80

5.2.3. Analytical Methods 81

5.2.4. Separation of Iron-Sulfide Solids from Culture Medium 81

5.2.5. X-Ray Diffraction (XRD) Analysis 81

5.2.6. TEM/EDX Analysis 82

5.2.7. Mass-Distribution Calculations 82

5.3. Bacterial Growth and Solid Formation with Soluble Fe Sources 87

5.3.1. Lactate as the Electron Donor 87

5.3.2. Pyruvate as the Electron Donor 90

5.4. Bacterial Growth and Solid Formation with Fe(III) (Hydr)oxides 94

5.4.1. Lactate as the Electron Donor 94

5.4.2. Pyruvate as the Electron Donor 103

5.5. Summary 112

6. SUMMARY 113

6.1. Summary of Results 1133

6.2. Future Research 116

REFERENCES 117

LIST OF TABLES

Table Page

1.1 Known Microorganisms Responsible for U(VI) Reduction. 6

1.2 Theoretical Redox Potential (Eh) Values at Neutral pH and 25℃ for Coupled Reduction Oxidation Reactions. 8

2.1 The Presence or Absence of SO_4^{2-}, Fe^{2+}, And Inoculum In the Media of the Five Serum Bottles in the Second Test. 21

2.2 Protein Concentration and Uraninite Thickness of the Biogenic Solids with or without NaOH Washing. 27

2.3 Ph, Concentrations Of Soluble U, SO_4^{2-}, Fe^{2+} and Biomass in the Five Assay Bottles in the Second Test under the Initial Conditions (Day 0) and the Final Conditions (Day 7); the UO2 Thickness of the Biogenic Solids from the Four Inoculated Bottles Estimated on Basis of XRD Data. 35

3.1 The Average Performance Parameters at Steady State for the Two Flow Rates. 46

3.2 The Average Performance Parameters at Steady State under Two HCO_3^{2-} Conditions. 48

4.1 Initial Concentrations of Lactate, Sulfate And Fe^{2+}, Initial and Final pHs, Experimental Durations, Estimated Concentrations of Final FeS Solids and Free Sulfide, Particle Thicknesses of Biogenic Mackinawite, Presence/Absence of Greigite and Vivianite under All Growth Conditions. 60

5.1 Measured Sulfate, Soluble Fe^{2+}, Formate Concentrations; pH; Experimental Durations; and Particle Thicknesses of Biogenic Mackinawite for All Iron-Source Conditions When Lactate or Pyruvate Was the Electron Donor. 85

5.2 Mass Distributions of Iron, Sulfur, and Solid Phases at the End of the Experiments Using Goethite, Hematite, or Ferrihydrite as the Iron-Based e^- Acceptor and Lactate or Pyruvate As the e^- Donor. 86

LIST OF FIGURES

Figure Page

1.1 Phase Relationships in the Low-T Fe–S System. 10

1.2 Schematic Models Describing the Intracellular Network of Electron Flow in D. vulgaris When Lactate and Pyruvate Are the Electron Donors. 16

1.3 Schematic of How the H_2 Diffuses through A Bubbleless Membrane Fiber (Left) and How The Electrons Are Transferred From H_2 to Reduce U(VI) by Bacteria (Right). 18

2.1 Concentrations of Soluble U, Lactate, and Protein in the Assay Bottles Inoculated with D. vulgaris. 26

2.2 X-Ray Diffraction Spectra of the Biogenic Solids with And without NaOH Washing. 27

2.3 XPS Spectra of the Biogenic Solids Associated with Biomass (without NaOH Washing). The Red Arrow Indicates the Characteristic Uraninite Shake-Up Satellite Peak. 28

2.4 The TEM Image And EDX Spectrum of the Biogenic Solids Associated with Biomass (without NaOH Washing). 29

2.5 U L_{III}-Edge Data for the Biogenic Solids Associated with Biomass (without NaOH Washing). (A) EXAFS Spectra (Solid Line) Collected at 77 K With Fit to Data (Dots); (B) Corresponding Fourier Transforms (Solid Line) and Fit to Data (Dots); (C) Corresponding Fourier Transforms of the Biogenic Solids (Red Line) and the Standard Uranyl [U(VI)] Solution (Black Line); and (D) Structural Parameters of Biogenic UO_2 (Produced In ASU) and Synthetic UO_2 (Produced In Uofm) Extracted from the EXAFS Analysis. 31

2.6 Concentrations of Soluble U(VI), Sulfate, Lactate and Acetate for Scenarios 1 (UO_2^{2+} Alone, ●), 2 (UO_2^{2+} + Fe^{2+}, ▲), 3 (UO_2^{2+} + SO_4^{2-}, ●), 4 (UO_2^{2+} + SO_4^{2-} + Fe^{2+}, ▲), and 5 (Abiotic Control, -); And Concentrations of Ferrous (Bars) Under Scenarios 2 and 4. 34

2.7 XRD Spectra of Solids Separated from the Bottles for Scenarios 1 (UO_2^{2+} Alone), 2 (UO_2^{2+} + Fe^{2+}), 3 (UO_2^{2+} + SO_4^{2-}), and 4 (UO_2^{2+} + SO_4^{2-} + Fe^{2+}). 37

3.1 Schematic of the Bench-Scale MBfR System Used to Investigate U(VI) Reduction. 40

Figure Page

3.2 Measured Flow Rate (Top), U Concentrations in Influent and Effluent (Middle), and Calculated U-Removal Percentage, U Surface Loading, and U-Removal Flux (Bottom) in Stage 1. 45

3.3 A Photograph of A Part of the Main Fiber Bundles in the MBfR, with Associated Black-Colored Solids, Taken After 9 Days of Continuous Operation in Stage 1. 45

3.4 Top: Concentrations of Soluble U (Orange Color) and Sulfate (Green Color) in Influent (Bars) and Effluent (Circles) of the MBfR in Stage 2. Bottom: Reduction Fluxes (Bars) and Average Surface Loadings (Dashed Lines) of Soluble U (Orange Color) and Sulfate (Green Color) in the MBfR In Stage 2. 48

3.5 X-Ray Diffraction Spectrum of the Solids Separated from the Whole Coupon Fiber Bundle in the MBfR. 49

3.6 Transmission Electron Microscopy Images of Various Locations in the Fixed Cross Section of A Single Fiber with Biofilm. 51

3.7 EDX Spectra Of Different Locations Near The Outside Wall Of The Fiber, As Indicated In The Cropped TEM Image Of Fig 5.6B On Left. 52

3.8 EDX Spectra Of Different Locations Around A Rod-Shaped Cell, As Indicated In The Cropped TEM Image Of Fig 5.6C On Left. 53

3.9 EDX Spectra Of Different Locations Around The Encrusted Round Spore, As Indicated In The Cropped TEM Image Of Fig 5.6E On Left. 54

3.10 Relative Abundances of the Most Abundant Microbial Phylotypes of the Biofilm Samples at the Family Level in Stage 1 and Stage 2. 56

4.1 Concentrations Of Lactate, Sulfate, Acetate, Soluble Fe^{2+}, Ph, And Protein During The Growth Of D. vulgaris With Initial Lactate-To-Sulfate Mole Ratios Of 0.5:1 (●), 0.8:1 (▲), And 1.9:1 (■). 65

4.2 XRD Patterns Of Solids Separated From The D. vulgaris Cultures With Lactate-To-Sulfate Mole Ratios Of 0.5:1, 0.8:1, And 1.9:1. 67

Figure Page

4.3 Concentrations of Lactate (A), Sulfate (B), Acetate (C), Soluble Fe^{2+} (D), Optical Density (E), and pH (F) During the Growth of D. vulgaris with Initial Iron-to-Sulfate Mole Ratios of 0.11:1 (●), 0.25:1 (■), 0.5:1 (▲), and 0.9:1 (◆). 69

4.4 XRD Patterns of Solids Separated from the D. vulgaris Cultures with Iron-to-Sulfate Mole Ratios of 0.1:1, 0.25:1, 0.5:1, and 0.9:1. 71

4.5 Concentrations of Lactate (A), Sulfate (B), Acetate (C), Soluble Fe^{2+} (D), pH (E), and Protein (F) During the Growth of D. vulgaris with Initial pHs of 5.6 (●), 6.5 (▲), 6.9 (■), 7.3 (◆) and 8.6 (*) within 8 Days. 73

4.6 XRD Patterns of Solids Separated from the D. Vulgaris Cultures with Initial pHs of 6.5 (A), 6.9 (B), 7.3 (C), and 8.6 (D). 74

4.7 (A) Pyruvate (●), Sulfate (■), and Acetate (▲) in the Culture of D. vulgaris Growing Exclusively on Pyruvate; (B) XRD Spectra of Solids Produced by D. vulgaris Growing Exclusively on Pyruvate. 76

4.8 (A) H_2 (●), Sulfate (■), and Acetate (▲) in the Culture of D. vulgaris Growing Exclusively on Hydrogen Gas; (B) XRD Spectra of Solids Produced by D. vulgaris Growing Exclusively on Hydrogen Gas. 78

5.1 Concentrations of Soluble Fe(II) (Black Bars), Soluble Fe(III) (White Bars), and Sulfate (○) During the Growth of D. vulgaris with Lactate as the Electron Donor Plus Soluble Fe^{2+} as the Iron Source (A) or Soluble Fe^{3+} As the Iron Source (B). 88

5.2 XRD Spectra of Solids Separated from Media with Soluble Fe^{2+} as the Iron Source (A) Or with Soluble Fe^{3+} as the Iron Source (B). 89

5.3 Concentrations of Soluble Fe(II) (Black Bars), Soluble Fe(III) (Grey Bars), and Sulfate (○) During the Growth of D. vulgaris with Pyruvate as the Electron Donor Plus Soluble Fe^{2+} as the Iron Source (A) or Soluble Fe^{3+} as the Iron Source (B). 92

5.4 XRD Spectra of Solids Separated from Media with Pyruvate as the Electron Donor Plus Soluble Fe^{2+} as the Iron Source (A) or with Soluble Fe^{3+} as the Iron Source (B). 93

Figure Page

5.5 Concentrations of Soluble Fe(II) (Bars), Sulfate (○), Lactate (▲), and Acetate (◇) During the Growth Of D. vulgaris with Lactate as the Electron Donor and with Goethite (α-FeOOH, A1 and A2), Hematite (α-Fe_2O_3, B1 and B2), or Ferrihydrite ($Fe_2O_3 \cdot 0.5H_2O$, C1 and C2) Solids as the Solid-Phase Electron Acceptor. 96

5.6 TEM Images (Left Column) and EDX Spectra (Right Column) of Solids Separated from Media with Goethite Plus Lactate (G+L), Hematite Plus Lactate (H+L), and 2-Line Ferrihydrite Plus Lactate (F+L). 99

5.7 XRD Spectra of Synthetic Goethite (α-FeOOH, Top Line in A), Hematite (α-Fe_2O_3, Top Line in B), 2-Line Ferrihydrite ($Fe_2O_3 \cdot 0.5H_2O$, Top Line in C), and Biogenic Solids from Bottles G+L (Bottom Line in A), H+L (Bottom Line in B), and F+L (Bottom Line in C). Lactate Was the Electron Donor in All Cases. 100

5.8 The TEM Image and the EDX Spectrum of A nm-Level Spot Showing Crystal Lattices in the Solids from Bottle with Hematite Plus Lactate (H-L). The Red Dot Indicates the Selected Area for EDX Scanning, and the Red Arrow Indicates the Lattice Fringes. 101

5.9 TEM Images and the Comprehensive EDX Results of Spots in the Solids Produced from the Bottle with Goethite Plus Lactate (G-L). 102

5.10 Concentrations of Soluble Fe(II) (Bars), Sulfate (○), Phosphate (✚), Pyruvate (▼), Acetate (◇), and Formate (⊙) During the Growth Of D. vulgaris with Pyruvate as the Electron Donor Plus Goethite (A1 And A2), Hematite (B1 And B2), or Ferrihydrite (C1 And C2) Solids as the Solid-Phase Electron Acceptor. 106

5.11 XRD Spectra of Synthetic Fe(III) (Hydr)oxides (Top Lines) and Final Solid Products (Bottom Lines) with Pyruvate As the Electron Donor Plus Goethite (α-FeOOH, A), Hematite (α-Fe_2O_3, B), or Ferrihydrite ($Fe_2O_3 \cdot 0.5H_2O$, C) Solids as the Solid-Phase Electron Acceptor. 107

5.12 TEM Images (Left) and EDX Spectra (Right) of Solids Separated from Media with Goethite Plus Pyruvate (G+P), Hematite Plus Pyruvate (H+P), and 2-Line Ferrihydrite Plus Pyruvate (F+P). 121

Figure Page

5.13 The TEM Images and the Comprehensive EDX Results of Two Spots in the Solids Produced from the Bottle With Hematite Plus Pyruvate. 109

5.14 Solid Lines: the Simulated Mimimum Soluble Fe(II) Concentration Allowing Vivianite Precipitation Given the Actual Phosphate Concentration and pH Value in the G-P, H-P, and F-P Bottles Featuring 0.3 M Inonic Strength; Square Dots: the Actual Soluble Fe(II) Concentration in the G-P, H-P, and F-P Bottles. 110

5.15 The TEM Image and the EDX Spectrum of A nm-Level Spot Showing Crystal Lattices in the Solids from Bottle with Goethite Plus Pyruvate (G-P). 111

CHAPTER 1. INTRODUCTION

1.1. Uranium in our environment

1.1.1. Uranium in nature

Uranium (U) is the heaviest naturally occurring element in the universe. Although a low-abundance element, it is widely and uniformly distributed in the Earth's crust at an average range of 2-4 ppm[1, 2]. U is the core component of several minerals, such as uraninite (UO_2), carnotite [$K_2(UO_2)_2(VO_4)_2 \cdot 3H_2O$], autunite [$Ca(UO_2)_2(PO_4)_2 \cdot 10\text{-}12H_2O$], torbernite [$Cu(UO_2)_2(PO_4)_2 \cdot 12H_2O$] uranophane [$Ca(UO_2)_2(SiO_3OH)_2 \cdot 5H_2O$], and coffinite [$U(SiO_4)_{1-x}(OH)_{4x}$]. U is also found in great accumulation in phosphate-rock deposits, lignite, and monazite sands, particularly in uranium-rich ores[3].

1.1.2. Physical and chemical properties

Uranium has six isotopes (U-233 through U-238). Among them, U-234, U-235, and U-238 are found in nature, with relative abundances of 0.005%, 0.7% and 99.3%, respectively[4]. All isotopes have unstable nuclei and decay slowly. U-238 and U-235 undergo alpha decay, emitting alpha particles (ionized helium), and their half-lives are about 4.468×10^9 years (roughly the age of the Earth) and 7.13×10^8 years, respectively[4].

Uranium has four oxidation states: +3, +4, +5, and +6. The most important oxidation states are U(IV) and U(VI), and the most common species in the aqueous chemistry is the uranyl ion (UO_2^{2+}), in the +6 oxidation state. The insoluble uraninite (UO_2), with the U oxidation state of +4, is a major ore of uranium[5].

Organic and inorganic U(VI)-complexes are important to uranium aqueous chemistry because they change its solubility and mobility[6, 7]. The uncomplexed uranyl ion forms complexes with citric, fulvic, and humic acids[8-10]. The uranyl ion also can form complexes with inorganic anions such as hydroxyl, carbonate, phosphate, sulfate, chloride, and fluoride[7, 11-13]. The uranyl complexes with hydroxyl, carbonate, and phosphate are most important due to their higher stability, and they strongly affect the distribution of uranyl species in groundwater[7, 14]. In hard (i.e.,

rich in calcium) groundwater contaminated by uranium, a ternary calcium-uranyl-carbonate species [$Ca_2UO_2(CO_3)_{3\ (aq)}$] also is present, but is less soluble than the binary uranyl-carbonate species [UO_2CO_3, $UO_2(CO_3)_2^{2-}$, and $UO_2(CO_3)_3^{4-}$] [15-19].

1.1.3. U applications and consequent environmental contamination

Although uranium was used as a colorant in glass as early as in the Roman era and was used for tinting and shading in early photography, its radioactive properties were not recognized until the end of the 19th century, and its potential application as an energy source was realized only in the middle of the 20th century[20]. Today, uranium primarily fuels nuclear power reactors that generate electricity and smaller-sized nuclear reactors that produce isotopes for medical and industrial purposes[20]. Highly enriched uranium, which contains more than 20% U-235, is a primary component of certain nuclear weapons. The enrichment process leaves a residual having a higher content of U-238 than natural uranium; it is called depleted uranium (DU)[20, 21]. Because of its unique physical properties -- such as a high mass-to-volume ratio (1 cm^3 = 19 g, a density 1.68 times greater than lead), high combustibility, and high ignitability -- DU has multiple military and commercial applications[22]. The enrichment process also has a byproduct referred to as *raffinate*, which is an acidic waste stream containing trace amounts of toxic heavy metals, including uranium and its decay products. When not disposed of properly, this waste can leach into the groundwater to cause large-scale contamination[23].

After the Cold War, the United States partially shut down nuclear weapons production and initiated efforts for the decommissioning and reprocessing of weapons material[24]. The U.S. Department of Energy (DOE) has taken charge of identifying and remediating 120 uranium-contaminated sites covering 7280 km^2 in 36 states and territories[24, 25].

1.1.4. Radiological and chemical toxicities of uranium to human beings

U-238 and U-235 are weakly radioactive because they decay with long half-lives and produce weak alpha particles which can be shielded by a sheet of paper[26, 27]. U^{235}-deficient DU has 40% less radioactivity than natural uranium[28].

Health effects from external exposure to uranium are considered low and limited to skin contact[29-31]. Health effects related to internal exposure/deposition, however, are much more severe and can result from either chemical or radiological toxicity[22, 29]. Internal exposure can occur through three pathways: ingestion of food and water, inhalation of aerosol, and embedded fragments or contaminated wounds. The toxicity is strongly affected by oxidation state and the solubility: metallic uranium is relatively non-toxic compared to hexavalent uranyl ion, which is the most stable species only present in the mammalian body[32-34].

The health effects of uranium in drinking water are chronic rather than acute[35]. Studies on animals indicate that most ingested uranium is rapidly eliminated, while only 2–5% soluble U and 0.2% insoluble U are absorbed into the blood from the intestine[29, 36, 37]. Most U absorbed into the blood is rapidly cleared and leaves the body in urine within the first week after intake. The rest is distributed to tissues and organs such as the kidneys and the bones; it remains much longer in the bones[29, 38]. Uranium is genotoxic, mutagenic, and carcinogenic. Toxicity studies on rats suggest that ingestion of high-level uranium may be associated with an increased risk of kidney damage by loss of tubular re-absorptive ability or increased glomerular permeability[39-43]. In addition, uranium is proven to have impacts on reproduction and development in mammals by disturbing cell division or enzyme systems, changing/inhibiting protein or steroid synthesis, and disrupting behavioral patterns involved in normal reproduction[44-50].

1.1.5. Regulations of uranium concentration in drinking water

The World Health Organization (WHO) limits the uranium concentration in drinking water to 2 µg/l, with the goal to protect against possible renal effects[51]. The United States Environmental Protection Agency (USEPA) finalized the maximum contamination level (MCL) for uranium of 30 µg/L in December 2000[52]. Furthermore, USEPA has estimated that the additional lifetime risk associated with U-contaminated drinking water at the concentration allowed in a public water supply is about 1 in 10,000, which means the occurrence of 1 additional fatal cancer in 10,000 persons who consume two liters of this water per day for 70 years[35].

1.2. Bioremediation of uranium in contaminated groundwater

1.2.1. Fundamental principle

Uranium, similar to several metal contaminants (e.g., chromium, lead, and mercury) cannot be degraded to innocuous components. Instead, its *in situ* remediation immobilizes the soluble U(VI) in the groundwater in order to reduce exposure risks to human health, environment, and property[7, 24, 53]. In general, soluble U can be immobilized and retained through adsorption, complexation, and reductive precipitation[7, 54-56].

1.2.2. Adsorption and complexation

Previous studies found that uranium was adsorbed to the surface of natural minerals such as goethite, ferrihydrite, hematite, kaolinite, phyllite, zeolite, lepidocrocite, muscovite, mackinawite, pyrite, calcite, attapulgite, and halloysite. Acidic conditions (4-6 as the optimal pH range) are favorable[57-72]. Adsorption also was affected by uranyl complexation with humic acid and phosphate[57, 61, 73]. Microbial biomass also can bind soluble uranium. Extracellular biosorption was observed in *Pseudomonas aeruginosa*, *Rhizopus arrhizus*, *Aspergillus fumigatus*, *Myxococcus xanthus*, *Penicillium digitatum*, and even macro marine algae (*Ulva* and *Sargassum* spp.)[7, 19, 66, 74-83]. Soluble uranium was adsorbed to the surfaces containing carboxyl groups ($>COO–UO^{2+}$) or phosphate groups ($>PO_4H–UO^{2+}$), proteinaceous surface layers featuring cell-wall chitins structure, and extracellular polymetric substances (EPS), and the processes were pH-dependent as well. Thermodynamic modeling also suggested that uranyl hydroxides, uranyl carbonates, and calcium-U-carbonates can form stable surface complexes on the bacterial cell of *Bacillus subtilis*[18].

Besides extracellular biosorption, intracellular biosorption of uranium has been reported. Because uranium has no essential biological function in metabolism – in contrast to Fe, Cu, Zn, Co, and Mn -- the transport and accumulation of uranium into microbial cells is considered to be a metabolism-independent process caused by increased membrane permeability from uranium toxicity[19, 84, 85]. Once U is inside the cell, inorganic polyphosphates (poly P), an intracellular

energy-storage material, is able to chelate uranium, which improves cellular tolerance to uranium[19, 86-88].

1.2.3. Reductive precipitation

Soluble U(VI) can be reduced to U(IV) chemically by sulfide, iron(II), elemental iron, and elemental zinc. The U(IV) precipitates as uraninite[71, 89-95]. U(VI) reduction also occurs concomitantly with citrate photodegradation by visible light[96, 97]. Nevertheless, these abiotic reductions are inhibited by negatively charged U(VI)–CO_3 complexes in nature, mostly $UO_2(CO_3)_3^{4-}$ and $UO_2(CO_3)_2^{2-}$ at neutral pH[7, 98].

In the past decades, many studies have established that a variety of prokaryotes can enzymatically reduce U(VI) to U(IV)[24]. This biological process has been recognized more economic, efficient, and sustainable in practical application to *in situ* remediation of U-contaminated groundwater and soil, in spite of the lack of complete understanding the biochemistry in the process[24]. Table 1, modified from Wall and Krumholz[24], lists the microorganisms (mostly bacteria) that have been discovered to enzymatically reduce U(VI) so far, and the number is still growing. Those microorganisms including dissimilatory sulfate reducers (*Desulfovibrio*, *Desulfomicrobium*, and *Desulfosporosinus*), dissimilatory iron(III) reducers (*Geobacter* and *Shewanella*), hyperthermophilic archaea (*Pyrobaculum islandicum*), acidotolerant bacteria (*Salmonella subterranean*), fermentative bacteria (*Clostridium* sp.), myxobacteria (*Anaeromyxobacter dehalogenans*), and even a family of denitrifiers (*Rhodocyclaceae*)[19]. Sulfate and iron(III) reducers have been most thoroughly investigated and are thought to play significant roles in both degradation of organic contaminants (e.g. fatty acids and aromatic hydrocarbons) and immobilization of uranium in the subsurface[7, 24, 99].

Table 1.1 Known microorganisms responsible for U(VI) reduction.

Microorganism	Type	References
Anaeromyxobacter dehalogenans	Dehalogenator	100-102
Clostridium sp.	Fermenters	103-105
Deinococcus radiodurans	Iron(III) reducer	106, 107
Desulfomicrobium norvegicum	Sulfate reducer	108
Desulfotomaculum reducens	Sulfate reducer	109-111
Desulfosporosinus orientis	Sulfate reducer	112
Desulfovibrio baarsii	Sulfate reducer	108
Desulfovibrio desulfuricans	Sulfate reducer	113-119
Desulfovibrio sulfodismutans	Sulfate reducer	108
Desulfovibrio vulgaris	Sulfate reducer	108, 120, 121
Geobacter metallireducens	Iron(III) reducer	122, 123
Geobacter sulfurreducens	Iron(III) reducer	124
Geobacter uraniireducens	Iron(III) reducer	125, 126
Geobacter daltonii	Iron(III) reducer	127
Pseudomonas putida	Iron(III) reducer	128
Pyrobaculum islandicum	Iron(III) reducer	86
Salmonella subterranea	Denitrifier	129
Shewanella alga	Iron(III) reducer	130-132
Shewanella oneidensis	Iron(III) reducer	133-139
Shewanella putrefaciens	Iron(III) reducer	133, 134, 140-142
Veillonella alcalescens	Denitrifier	143, 144
Thermoterrabacterium ferrireducens	Iron(III) reducer	145, 146
Thermus scotoductus	Iron(III) reducer	146-148
Rhodocyclaceae family	Denitrifier	149

Some bacteria gain energy for cell synthesis and growth by coupling oxidation of electron donors (organic compounds or H_2) with reduction/respiration of U(VI) to U(IV), subsequently resulting in UO_2 precipitation[7, 19, 24, 133, 150-155]. The reductive reactions of dominant uranyl-carbonate species in groundwater include[156]:

$$UO_2CO_3 + 6H^+ + 2e^- \rightarrow UO_{2(s)} + HCO_3^- \quad (1.1)$$

$$UO_2(CO_3)_2^{2-} + 2H^+ + 2e^- \rightarrow UO_{2(s)} + 2HCO_3^- \quad (1.2)$$

$$UO_2(CO_3)_3^{4-} + 3H^+ + 2e^- \rightarrow UO_{2(s)} + 3HCO_3^- \quad (1.3)$$

$$Ca_2UO_2(CO_3)_3 + 3H^+ + 2e^- \rightarrow UO_{2(s)} + 3HCO_3^- + 2Ca^{2+} \quad (1.4)$$

$$CaUO_2(CO_3)_3^{2-} + 3H^+ + 2e^- \rightarrow UO_{2(s)} + 3HCO_3^- + Ca^{2+} \quad (1.5)$$

Several factors are reported to affect microbial U(VI) reduction:

Carbonate. The very stable binary uranyl-carbonate complexes greatly enhance the uranium solubility, making the U(VI) more available for bioreduction than complexes with hydroxide, phosphate, and some minerals[157-160]. However, a study reported that a high concentration of carbonate (100 mM) fully inhibited enzymatic U(VI) reduction, although a concentration of 33 mM had no effect[161, 162]. In addition, U(VI) biosorption became predominant over bioreduction in the absence of carbonate[163].

Calcium/hardness. Ca^{2+} and carbonate, released from calcite dissolution in sediments[7, 67], facilitate the formation of ternary Ca-U(VI)-CO_3 complexes especially the predominant $Ca_2UO_2(CO_3)_{3\ (aq)}$, at circumneutral to alkaline pH conditions in the groundwater[16, 17, 67, 164]. Studies reported that ternary Ca-U(VI)-CO_3 complexes made U as a less energetically favorable electron acceptor among U(VI) species[165-167]. Quantitatively, 0.4 – 0.8 mM Ca (equal to the hardness of 40 – 80 mg/l as $CaCO_3$) had a significant inhibitive effect on U(VI) reduction by *Shewanella putrefaciens* with or without Fe(III) (hydr)oxides as additional electron acceptors[165].

Uranium concentration. Uranium is chemically toxic to bacteria, including U(VI) reducers[117, 119, 168-170]. The absence of acetate production (from ethanol fermentation) and U reduction by mixed sulfate-reducing bacteria (SRB) occurred when the U(VI) concentration was above 1.6 mM, and the inhibition constant for U(VI) was ~100 μM[170]. The minimum inhibiting concentration (MIC; the toxicant concentration that completely inhibits microbial growth) of U(VI) to *Desulfovibrio desulfuricans* has been reported in a wide range, from 140 to 5,000 μM[117, 119]. Elias et al. reported successful U(VI) reduction without retardation by *D. vulgaris* at an initial concentration of 2 mM, but complete inhibition of U(VI) reduction at an initial concentration of 5 mM[121]. In addition, highly soluble U(VI) in uranium carbonate complexes showed no toxicity,

while less soluble U(VI) complexes in PIPES buffer exerted severe toxicity to *Desulfovibrio desulfuricans*[119].

Other electron acceptors. When multiple electron acceptors are present, competition for electrons takes place and affects the enzymatic activities. According to the redox potential summarized in Table 1.2, O_2, Mn(IV), Fe(III), and NO_3^- are preferential electron acceptors over U(VI), whereas U(VI) is preferred over SO_4^{2-}, S^0, or CO_2[24]. U(VI) reduction was found to completely inhibit sulfate reduction when lactate was the electron donor for *D. vulgaris,* but only slowed sulfate reduction when H_2 was the electron donor[121]. On the other hand, U(VI) reduction was halted by the presence of either soluble Fe(III) or Fe(III) minerals (such as Fe(III) (hydr)oxides) for sulfate and iron reducers[108, 121, 132]. Other studies revealed that nitrate was preferred over U(VI), and U(VI) was not rapidly consumed until nitrate was nearly depleted[162, 171-173].

Table 1.2 Theoretical redox potential (Eh) values at neutral pH and 25℃ for coupled reduction-oxidation reactions of interest.

Coupled Reaction	***Eh*** (V)	Reference
acetyl-CoA + CO_2 + 2e^- → pyruvate	–0.500	[174]
H^+ + e^- → 1/2 H_2	–0.414	[175]
cytochrome c_3 ox/red	–0.290	[176]
goethite (α-FeOOH) + e^- → Fe^{2+}	–0.274	[177]
hematite (α-Fe_2O_3) + e^- → Fe^{2+}	–0.284	[177]
SO_4^{2-} + 6e^- → S^{2-}	–0.220	[174]
Pyruvate + 2e^- → lactate	–0.190	[174]
ferrihydrite (Fe_2O_3·0.5H_2O) + e^- → Fe^{2+}	±0.100	[177]
UO_2^{2+} + 2e^- → UO_2	+0.411	[166]
$Ca_2UO_2(CO_3)_{3\,(aq)}$ + 2e^- → UO_2	+0.424	[166]
$UO_2(CO_3)_3^{2-}$ + 2e^- → UO_2	+0.521	[166]
$CaUO_2(CO_3)_3^{2-}$ + 2e^- → UO_2	+0.576	[166]
$UO_2(CO_3)_3^{4-}$ + 2e^- → UO_2	+0.689	[166]
Fe^{3+} + e^- → Fe^{2+}	+0.772	[177, 178]

Previous studies discovered that biogenic uraninite was mainly nanocrystalline, with physical properties (smaller particle size and large specific surface area) quite different from bulk uraninite[137, 179, 180]. These particles tended to associate with bacterial cells by 1) precipitation in

the periplasm of Gram-negative and Gram-positive bacterial cells[102, 181, 182]; 2) intracellular deposition in the cytoplasm, albeit with unknown mechanism[183, 184]; and 3) accumulation on extracellular polymeric substances (EPS), forming dense covers over the thin (nm) filamentous structures surrounding cells[185, 186]. The surface structure and reactivity of biogenic UO_2 also was affected by the presence of surface-associated organic matter on its surface[187-189].

Although uraninite was long assumed to be the sole product of either microbial or chemical U(VI) reduction, recent studies revealed that, besides uraninite, noncrystalline U(IV) species referred to as monomeric or mononuclear U(IV) also were produced when either biological or chemical U(VI) reduction took place[190-198]. The mechanism remains unknown and needs further investigation.

1.2.4. Drawback: reoxidation

A serious drawback to bioremediation based on U(VI) reduction and immobolization is the potential for uraninite to be re-oxidized (and thus re-mobilized) to U(VI) by exposure to O_2 or a variety of other oxidants present in the groundwater, including nitrate, nitrite, and Fe(III) (hydr)oxides[171, 199-210]. Though under reducing conditions, U(IV) oxidation is thermodynamically favorable in theory[7]. Humic substances, siderophores, and accumulation of carbonate species arising from microbial respiration also may stimulate and promote uraninite oxidation by forming highly stable U(VI) complexes[18, 156, 211].

1.3. Iron-sulfide solids for U remediation

1.3.1. Iron-sulfide minerals in nature

Iron sulfide minerals are abundant in anaerobic environments, such as freshwater and marine sediments[212-214]. Iron-sulfide solids vary in morphological characteristics and chemical composition. For example, major authigenic iron sulfides in sediments include small nanocrystallites of poorly ordered FeS, mackinawite ($Fe_{1+x}S$, where x = 0 to 0.11[215]), greigite (Fe_3S_4), and pyrite (FeS_2, or iron disulfide)[216, 217]. In addition, pyrrhotite ($Fe_{1-x}S$, where x = 0 to 0.2[215]) and marcasite (FeS_2) can occur, but are rare[218]. Berner revealed that, due to its poor

crystallinity, amorphous FeS usually is the initial precipitate formed in anoxic sedimentary environments[219]. Within days, the small FeS nanocrystallites develop long-range order, and more stable, but disordered mackinawite particles form[220, 221]; however, the complete transformation to crystalline mackinawite can take up to two years in aqueous solution at 25℃ [221].

Due to its thermodynamic instability, mackinawite slowly transforms into more stable phases, greigite and pyrite, under reduced conditions at low temperatures[212]. Pyrite, often considered the most abundant iron sulfide, is widespread in sediments and sedimentary rocks deposited in geological record[220]. Greigite is generally thought to form via the aging of mackinawite[212], while pyrite seems to be the product of a rapid crystallization process from greigite[222, 223] or directly from mackinawite[223, 224]. However, the abiotic formation of greigite from mackinawite in laboratory studies has been questioned, since it may be the result of accidental oxygen exposure during solid phase characterization[217]. Nonetheless, (micro)biologically controlled mineralization has been considered responsible for the transformation of mackinawite to greigite in some systems: e.g., reaction of dissolved sulfide produced by SRB with Fe^{2+} led to either poorly ordered (i.e., nanocrystalline) mackinawite[225] or mixtures of mackinawite and greigite[226]. Fig 1.1 illustrates the relationship of different iron-sulfide solids.

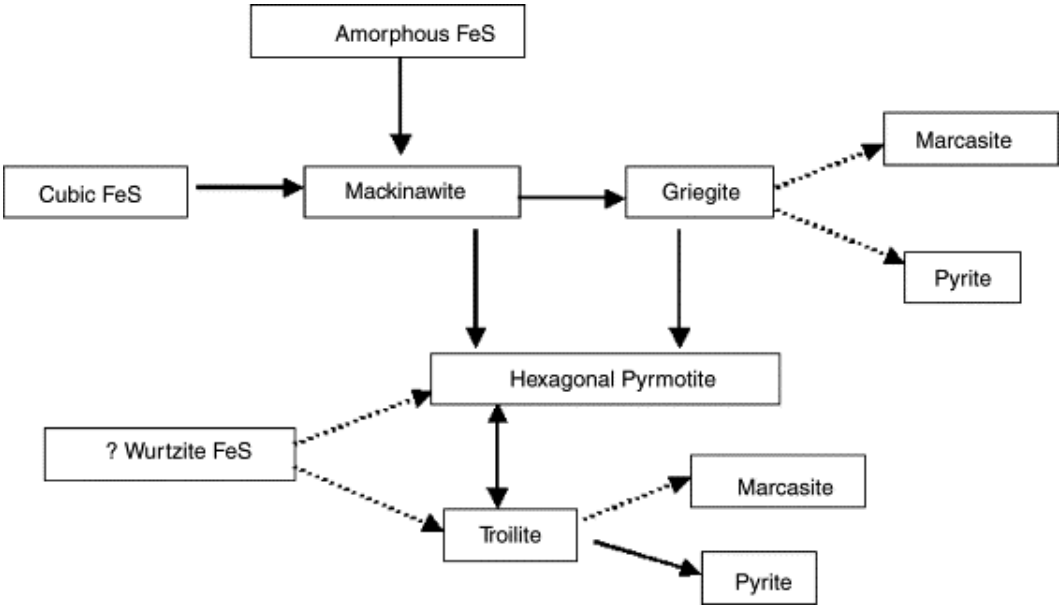


Fig 1.1 Phase relationships in the low-T Fe–S system[227, 228].

1.3.2. Derivation of iron-sulfide minerals

The source of the sulfide for biogenic iron sulfides typically is sulfate reduction by sulfate-reducing bacteria (SRB). Precipitation of iron sulfide often causes the blackening of water, which, along with the smell of hydrogen sulfide, indicates the presence of SRB with a high metabolic activity[229]. Similarly, Fe^{2+} comes from bio-reduction of soluble Fe^{3+} or Fe(III)-(hydr)oxide solids. Fe^{3+} reduction is carried out by some SRB, as well as iron-reducing bacteria[230, 231]. Microbial Fe(III) reduction, especially of Fe(III) (hydr)oxides such as goethite (α-FeOOH), hematite (α-Fe_2O_3), and ferrihydrite ($Fe_2O_3 \cdot 0.5H_2O$), significantly influences the availability of Fe(II) for the subsequent formation of FeS and may affect the characteristics of the iron-sulfide formed[232-235].

Bioreduction of Fe(III)-(hydr)oxides can occur by two mechanisms[236-239]: directly by enzymatic catalysis (Eqns 1.6 – 1.8) and indirectly via chemical reaction with biogenic sulfide (Eqns 1.9 – 1.11):

$$\alpha\text{-FeOOH} + 3H^+ + e^- \rightarrow Fe^{2+} + 2H_2O \qquad (1.6)$$

$$Fe_2O_3 + 6H^+ + 2e^- \rightarrow 2Fe^{2+} + 3H_2O \qquad (1.7)$$

$$Fe_2O_3 \cdot 0.5H_2O + 6H^+ + 2e^- \rightarrow 2Fe^{2+} + 3.5H_2O \qquad (1.8)$$

$$\alpha\text{-FeOOH} + 0.5HS^- + 2.5H^+ \rightarrow Fe^{2+} + 0.5S^0 + 2H_2O \qquad (1.9)$$

$$Fe_2O_3 + HS^- + 5H^+ \rightarrow 2Fe^{2+} + S^0 + 3H_2O \qquad (1.10)$$

$$Fe_2O_3 \cdot 0.5H_2O + HS^- + 5H^+ \rightarrow 2Fe^{2+} + S^0 + 3.5H_2O \qquad (1.11)$$

The mechanisms and kinetics of enzymatic and chemical reductions of Fe(III) (hydr)oxides have been well studied. For enzymatic reductions, three possible mechanisms (direct contact, formation of electron shuttles such as nanowires or redox-active organic matters, and formation of soluble complex ligands) have been proposed for how electrons transfer from the microbes to the solid surface[231, 240-242]. For chemical reductions by dissolved sulfide, an iron-sulfide complex on the solid surface is rapidly formed prior to the Fe(III) reduction / sulfide

oxidation, and the subsequent dissolution / detachment of Fe(II) has been identified as the rate-limiting step[238, 243-246].

1.3.3. Contribution of iron-sulfide solids in U remediation

Iron-sulfide solids are thought to play significant and diverse roles in uranium bioremediation[24, 199, 230, 247].

1.3.3.1. Immobilization of soluble uranyl

Either natural occurring or synthetic iron-sulfide solids were proven to adsorb soluble U(VI) on the surfaces. Moyes et al. reported that uptake of uranium on 10-g/l mackinawite increased linearly, exceeding 99% when the initial U(VI) concentrations was from 0.5 to 5.0 mM[66]. Livens et al. further discovered that uranium formed uranyl surface complexes on oxidized regions of the mackinawite surface at low concentrations, whereas they promoted further surface oxidation and formed a mixed U(VI)/U(IV) oxide phase at higher concentrations[228]. Hua and Deng's study on U(VI) uptake by amorphous FeS under CO_2-free conditions revealed rapid removal of soluble U(VI) accompanied by a simultaneous release of Fe(II), and they proposed an ion exchange mechanism (i.e., Fe(II) is replaced by U(VI)) for the observed U(VI) phase transfer[248].

Although Wersin et al. observed a patchy distribution of adsorbed uranium at the surface of pyrite, which was mainly associated with oxidized surface species of sulfur and iron, and had higher relative amounts of unreduced surface-uranyl (above 97% of initial uranyl) at pH above 6[71]. Another study further confirmed that the sorption of uranyl on pyrite surfaces was concomitant with partial reduction of U with the formation of a hyper-stoichiometric $UO_{2+x\,(s)}$ and that S groups governed U(VI) sorption and reduction[72]. *In situ* U sorption as U(VI) and U(IV) on the surface of biogenic framboidal pyrite in U-contaminated sediments was also reported[249].

Some studies reported significant reductive immobilization of uranyl by iron-sulfide solids. Hua and Deng revealed that rapid sorption of soluble U(VI) within 1 hour was followed by a slower U(VI) reduction to form $U_3O_8/U_4O_9/UO_2$, polysulfide, and ferric iron[248]. In addition, Hyun et

al. confirmed uraninite formation through abiotic reduction by iron(II) monosulfide mackinawite, and they proposed a mechanism similar to homogeneous U(VI) reduction by aqueous sulfide[250].

1.3.3.2. Protection of uraninite reoxidation

The potential for iron-sulfide solids to act as redox buffers to protect reduced UO_2 solids from reoxidation has been recognized in the bioremediation arena. Abdelouas et al. found that, in the presence of mackinawite, most oxygen was depleted in oxygen-saturated groundwater, and UO_2 oxidation was inhibited[199]. Sediment-column experiments conducted by Moon et al. confirmed that biogenic iron sulfides were capable of buffering against U(IV) oxidation[251]. Batch studies conducted by Bi et al. (2012) revealed that synthetic nanoparticulate mackinawite protected uraninite from rapid oxidation by dissolved oxygen, with dissolved U maintained below 0.4 µM for up to 60 hr[252]. The reactive properties of different iron sulfides may affect their capacity to protect uraninite against re-oxidation, although how has been less studied and remains largely unknown.

1.4. *Desulfovibrio vulgaris* and U reduction

1.4.1. Sulfate-reducing microorganisms

Sulfate-reducing microorganisms refer to a unique, but diverse group of prokaryotes with the capability of respiring SO_4^{2-} as the terminal electron acceptor for growth and energy. The three major groups of sulfate-reducing microorganisms are Gram-negative eubacteria (e.g., the genera *Desulfovibrio*, *Desulfobacter*, *Desulfobacterium*, and *Desulfobulbus*), Gram-positive eubacteria (e.g., *Desulfotomaculum* spp.), and archaea (e.g. *Archaeoglobus* spp.)[253]. The SRB also can be classified into two broad nutritional groups: 1) those that have an incomplete TCA cycle and carry out only fermentation (to acetate) of a limited range of organic substrates, such as lactate, ethanol, and pyruvate; and 2) those capable of performing complete oxidation to CO_2 (i.e., respiration and mineralization) of a much wider range of organic substrates[254].

Widely distributed in anaerobic terrestrial and aquatic environments, SRB play a complex and significant role in the sulfur and other major biogechemical and nutrient cycles[253]. They also are important in bioremediation, wetlands and wastewater treatment, and fuel production due to

their versatile abilities to degrade harmful organic contaminants and reduce inorganic contaminants[253]. Those organic contaminants include a variety of aromatic compounds from petroleum (e.g., benzene, toluene, ethylbenzene, xylenes, naphthalene, phenanthrene, and alkanes)[255-262]. The inorganic contaminants include sulfate, nitrate, iron, mercury, selenate, uranium, and chromate[263-267]. In particular, reductive dehalogenation of a wide ranged halogenated organics by SRB has been reported[268-272].

1.4.2. Desulfovibrio vulgaris

Desulfovibrio vulgaris is one of the most studied SRB species. Unlike some SRB that are able to completely oxidize organic electron donors, this species, as well as other Gram-negative *Desulfovibrio* spp., generates hydrogen gas (H_2) by fermentation of organic substrates (such as lactate and pyruvate). It is the subsequent oxidation of H_2 that is directly coupled with SO_4^{2-} respiration[273-275]. In addition, *Desulfovibrio* can gain energy exclusively from fermentation process when no electron acceptor is present[276-279].

Figure 1.2 illustrates schematically the intracellular network of electron flow in *D. vulgaris* when it couples SO_4^{2-} reduction with oxidation of lactate or pyruvate. When lactate is the electron donor, lactate and SO_4^{2-}diffuse from the periplasm to the cytoplasm, and lactate is fermented to pyruvate, releasing protons and electrons (step □ in the top part of Fig 1.2); Pyruvate is then fermented to acetate and CO_2, releasing protons and electrons (□); The protons and electrons produced in fermentations react with membrane-bound hydrogenases to form molecular hydrogen (H_2), which then diffuses to the periplasm (□):

$$CH_3CHOHCOO^- \rightarrow CH_3COCOO^- + H_2 \qquad (1.12)$$

$$CH_3COCOO^- + 2H_2O \rightarrow CH_3COO^- + H_2 + HCO_3^- + H^+ \qquad (1.13)$$

The molecular H_2 is re-oxidized by periplasmic hydrogenases to produce electrons transported to cytochrome c_3 and protons for ATP synthesis (□). Fe(III) and U(VI) are reduced by cytochrome c_3 (□):

$$Fe^{3+} + 1/2H_2 \rightarrow Fe^{2+} + H^+ \qquad (1.14)$$

$$UO_2(CO_3)_2^{2-} + H_2 \rightarrow UO_{2(s)} + 2HCO_3^- \qquad (1.15)$$

Electrons are transported through the cytochrome network to the cytoplasm (□), where sulfate is reduced to sulfide (□):

$$SO_4^{2-} + 4H_2 + 3/2H^+ \rightarrow 1/2HS^- + 1/2H_2S + 4H_2O \qquad (1.16)$$

When H_2 is the exogenetic electron donor, its oxidation and electron flow are identical to the H_2 generated from lactate fermentation (steps □-□).

When pyruvate is the electron donor, it is fermented to acetate, releasing protons and electrons (□ in the bottom part of Fig 1.2); the protons and electrons react with membrane-bound hydrogenases to form molecular hydrogen (H_2), which is then transported to the periplasm (□; Eqn 1.13). In the periplasm, the H_2 is re-oxidized by periplasmic hydrogenases to produce electrons transported to cytochrome c_3 and protons for ATP synthesis (□). Alternatively, pyruvate fermentation produces acetate and formate (instead of H_2):

$$CH_3COCOO^- + H_2O \rightarrow CH_3COO^- + CHOO^- + H^+ \qquad (1.17)$$

The formate diffuses to the periplasm and is oxidized by the formate dehydrogenase to produce electrons (□). The subsequent electron transfer processes (□-□) are identical to the lactate condition.

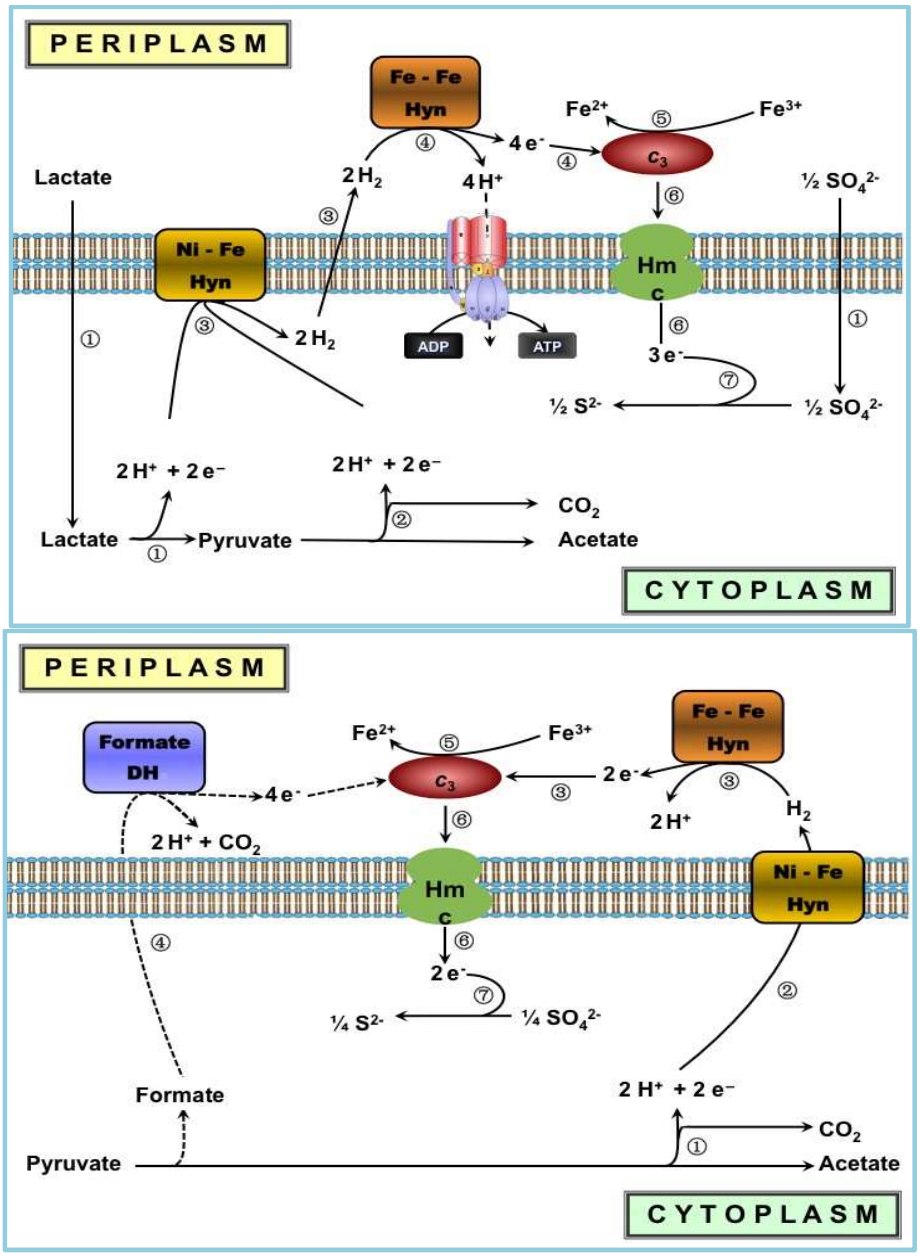


Fig 1.2 Schematic models describing the intracellular network of electron flow in *D. vulgaris* when lactate (top) and pyruvate (bottom) are the electron donors. These models are modified from previous work[121, 273-275]. Ni-Fe Hyn is the membrane-bound hydrogenase containing Ni and Fe; Fe-Fe Hyn is the periplasmic hydrogenase containing Fe only; Formate DH is the periplasmic formate dehydrogenase; c_3 is cytochrome c_3; and Hmc is the high-molecular-weight cytochrome complex.

1.5. Membrane biofilm reactor (MBfR)

The Membrane Biofilm Reactor (MBfR) is a novel technology to reduce oxidized contaminants in water and wastewater treatment. H_2 is an excellent electron donor, possessing multiple advantages: being nontoxic, having low biomass yields, and being an electron donor used by a diverse population of bacteria that can reduce many electron acceptors[280]. As shown in Figure 1.3, H_2 gas is delivered into the reactor by diffusion through the wall of a bubbleless gas-transfer membrane. The outside surface of the membrane accumulates H_2-oxidizing autotrophic bacteria as a biofilm[281, 282]. The oxidation of H_2 couples with reduction of oxidized contaminants in the bulk solution. This demand for H_2 to reduce electron acceptors is the driving force to pull H_2 through the membrane, and it eliminates practical problems in over- or under-dozing the electron donor, a shortcoming inherent to heterotrophic reactors[283, 284].

So far, many bench- and pilot-scale studies have documented that the H_2-based MBfR can be used to reduce a broad spectrum of oxidized contaminants, including nitrate, nitrite, sulfate, perchlorate, selenite, arsenate, chromate, dibromochloropropane, chloroform, tetrachloroethene (PCE), trichloroethene (TCE), and *N*-nitrosodimethylamine (NDMA)[280, 281, 284-296]. Along with ongoing bench-scale and pilot-scale studies focusing on testing more contaminants or optimizing the performance and devices, MBfR applications are now moving towards field testing and full-scale implementation[297].

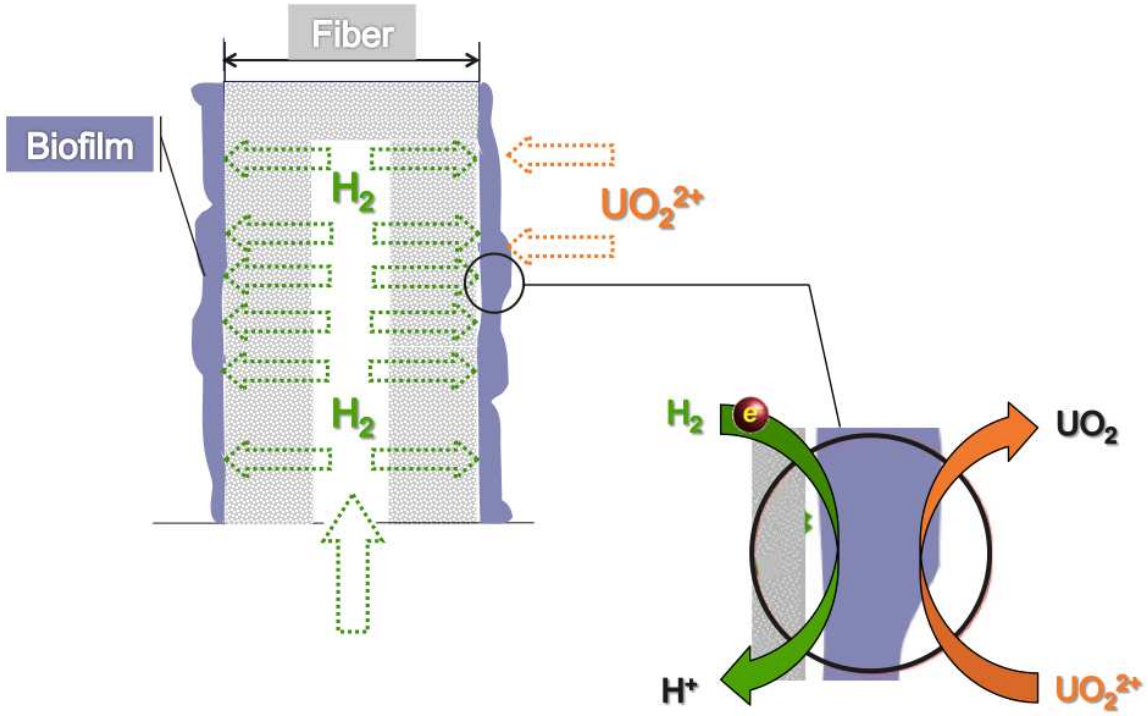


Fig 1.3 Schematic of how the H_2 diffuses through a bubbleless membrane fiber (left) and how the electrons are transferred from H_2 to reduce U(VI) by bacteria (right).

Among the interesting new applications to the MBfR is to remove U(VI) from the groundwater through bioreduction by U-reducing microorganisms. I chose *D. vulgaris* to test this application because 1) *D. vulgaris* is known to achieve U(VI) reduction coupled with oxidation of H_2 gas as the only electron donor[108, 120, 121]; and 2) it was abundant in the biofilm of an MBfR used for nitrate and sulfate reductions[298].

1.6. Objectives and organization

This dissertation presents achievements for my research on evaluating the direct and indirect roles of SRB on U bioremediation during my PhD study. Chapters 2 and 3 present my completed research on the direct contribution of *D. vulgaris* in U bioremediation: U(VI) Bioreduction to U(IV). Chapters 2 presents batch experiments on the production and characterization of biogenic UO_2, and the effects of sulfate and Fe(II) on U(VI) bioreduction and biogenic UO_2 characteristics. Chapter 3 presents the performance of an MBfR inoculated with *D. vulgaris* for U removal, along with post analyses on microbial community structures and solid

characterization.These results and the biogenic products are used by collaborative researchers in University of Michigan for their tests on uraninite re-oxidation with FeS protection. Chapters 4 and 5 present my completed research on the indirect contribution of *D. vulgaris* in U bioremediation: production of FeS which protects U(IV) reoxidation. Chapter 4 presents experiments on how controllable environmental parameters -- lactate-to-sulfate mole ratio, iron-to-sulfate mole ratio, pH, and electron donor -- affect SRB growth, iron sulfide solid formation, and the characteristics of the iron sulfides. Chapter 5 presents experiments on how a range of iron sources (soluble Fe^{2+} and Fe^{3+}, goethite, hematite, and ferrihydrite) affect iron-sulfide precipitation and the characteristics of the precipitates when lactate or pyruvate was the electron donor.

Chapter 6 summarizes the overall achievements in previous five chapters and proposes a few examples of future work.

CHAPTER 2. U(VI) reduction by *D. vulgaris* in batch reactors

2.1. Introduction

The goal of this chapter is to present the results of batch experiments I conducted to achieve enzymatic U(VI) reduction and UO_2 formation. Furthermore, the experiments investigated how the presence of SO_4^{2-} and/or Fe^{2+} affected the rate of U(VI) reduction and crystallization of biogenic UO_2. These completed experiments were the third part of the three-year collaborative project between ASU team and UofM team.

I prepared one manuscript based on these results. The title is "Growth of *D. vulgaris* on respiring U(VI) and characterization of the biogenic uraninite under various conditions". The authors are Chen Zhou, Raveender Vannela, Sung Pil Hyun, Kim F. Hayes, and Bruce E. Rittmann. The manuscript is being reviewed by all authors and will be submitted to *Environmental Science and Technology (ES&T)*. The methods, results, and discussion in the chapter are the same as in the manuscript, although the introductory material was relocated to Chapter 1.

2.2. Experimental setup

2.2.1. Strain, growth medium, and culturing conditions

Desulfovibrio vulgaris subsp. *vulgaris* Postgate and Campbell (ATCC 29579) was purchased from the American Type Culture Collection (Rockville, Md.) and grown in 160-ml serum bottles with 100 ml medium and a headspace of N_2. The serum bottles were sealed with rubber stoppers and aluminum caps and mixed in a shaker (200 rpm) at 30℃. For providing biomass in the experiments, *D. vulgaris* was cultured in the standard ATCC 1249 medium, which contains 2 g/l $MgSO_4$, 5 g/l sodium citrate, 1 g/l $CaSO_4$, 1 g/l NH_4Cl, 0.5 g/l K_2HPO_4, 3.5 g/l sodium lactate, 1 g/l yeast extract, and 2 ml/l 5% ferrous ammonium sulfate (FAS) solution. The pH of medium was adjusted to 7.5 before autoclaving and FAS addition. The medium contained 31.2 mM lactate, 19.4 mM citrate, 31.0 mM SO_4^{2-}, and 3.5 mM Fe(II). The cells were transferred

to new serum bottles every four to seven days by injecting 2 to 3 ml inoculum into the new bottles containing freshly prepared media.

2.2.2. Biomass suspensions

The procedure for preparing biomass suspensions was modified from Lovley and Phillips[113]. After complete lactate consumption was observed (usually three days after inoculation), the serum bottles were placed in an anaerobic glove box (Coy laboratory products Inc. Grass Lake, MI) overnight, during which time most of the solids settled to the bottom, while the biomass remained suspended in the liquid phase. Without re-suspending the settled solids, the bottles were opened in the anaerobic glove box, and the supernatant was transferred with a pipette to the autoclaved polycarbonate centrifuge tubes (Beckman coulter, Brea, CA). The tubes were then capped and centrifuged at 10,000 g for 5 min. The supernatant was removed with a pipette, and the pellet (i.e., the cells) was washed by the anoxic sterile 30 mM $NaHCO_3$ solution. The tubes were then capped, vortexed, and centrifuged again at 10,000g for 5 min. The washing steps were repeated two more times. As a result, 10 mL of biomass concentrate from two serum bottles was prepared for subsequent inoculation into the assay bottles, providing ca. 10 – 15 mg/L protein per assay bottle.

2.2.3. Assay solution

The basic assay solution consisted of (in mM) UO_2Cl_2 1, $NaHCO_3$ 30, NaLac 20, K_2HPO_4 0.014, $FeCl_2$ 0.03, and NH_4Cl 1. In the first test, the medium contained only the basic assay solution. In the second test, five bottles were designed for the assay using different combinations of the presence or absence of 1 mM Na_2SO_4, additional 1 mM $FeCl_2$, and biomass suspensions, as summarized in Table 2.1.

Table 2.1 The presence or absence of SO_4^{2-}, Fe^{2+}, and inoculum in the media of the five serum bottles in the second test.

Bottle #	SO_4^{2-}	Fe^{2+}	Biomass suspensions
1	–	–	**+**
2	–	+	**+**
3	+	–	**+**
4	+	+	**+**
5 (abiotic control)	**+**	**+**	**–**

All the chemical components except UO_2Cl_2 and $FeCl_2$ were added at the beginning into each assay bottle. Immediately after being boiled for 15 minutes and sparged by 80% N_2 / 20% CO_2 gas for 1 hour, each assay bottle was sealed with a rubber stopper to be air-tight, crimped with an aluminum cap, autoclaved for sterilization, and then put into the glove box overnight to cool to room temperature. $UO_2(Ac)_2$ and $FeCl_2$ concentrates were prepared with anoxic DI water in the glove box beforehand, and, after filtration through 0.2 μm membrane filters (LC+PVDF membrane, Whatman Inc., Haverhill, MA), were added along with the inoculum into assay bottles. The assay bottles were then moved out of the glove box and then mixed in a shaker (200 rpm) at 30℃.

2.2.4. Analytical methods

Routine analyses of liquid samples were carried out daily or every second day. 3-ml liquid samples were collected in an anaerobic glove box using a sterile syringe and stored in 15-ml centrifuge tubes for pH measurement with an Epoxy Semi-Micro Combination pH Electrode (Beckman Coulter BKA57187) and a pH meter (BKA58734). The samples were then centrifuged at 200 g for 6 minutes to remove the Fe-S solids, but not biomass, which had a lower density. The centrate was analyzed with a UV–Visible spectrophotometer (Cary 50 Bio, Varian, Inc., Santa Clara, CA) at 600-nm wavelength for optical density (OD), protein concentration with Coomassie (Bradford) reagents, and soluble iron (III) plus total soluble iron by the colorimetric 5-sulfosalicylic acid (SSA) method[299]. The standard deviations of the measurements for protein, iron (III), and total iron concentrations were 0.04 mg/l, 0.20, and 0.31 mM, respectively (n = 3 samples).

Samples diluted 200-fold after filtration were used for analyses of U concentrations by inductively coupled plasma optical emission spectrometer (ICP-OES, Thermo iCAP6300) at the wavelength of 385.9 nm, concentrations of anions (including sulfate, chloride, nitrate, and phosphate) by ion-exchange chromatography (IC, Dionex ICS2000) and for concentrations of volatile fatty acids (acetic acid, lactic acid, citric acid, pyruvic acid, formic acid, and butyric acid) by high-performance liquid chromatography (HPLC, Shimadzu 20AT) with a refractive index detector (RID). The standard deviations of the measurements for sulfate, lactate, acetate, and

pyruvate concentrations were 0.02, 0.01, 0.04, and 0.00 mM, respectively (n = 3 samples). H_2 was measured using a gas chromatograph (GC 2010, Shimadzu) equipped with a thermal conductivity detector and a packed column (ShinCarbon ST 100/120 mesh, Restek Corporation) for separating sample gases. The standard deviation of the measurement for hydrogen concentrations was 0.06 atm (n = 6 samples).

2.2.5. Separation of uraninite solids from culture medium

After no soluble U(VI) was detected, the serum bottles were placed in an anaerobic glove box and left there overnight, during which time most of the solids settled to the bottom. Without re-suspending the settled solids, bottles were opened (while still in the anaerobic glove box), and the supernatant was removed with a pipette. The solids and residual liquid (~ 10 mL) were transferred to 50-ml centrifuge tubes. About 40 ml anoxic sterile deionized water was used in order to rinse out any solids adhering to the walls inside the bottles and then transferred into the centrifuge tubes. The tubes were then capped, vortexed, and centrifuged at 1,800 g for 6 minutes. The supernatant was removed with a pipette, and the rinsing steps were repeated two more times. The tubes were then placed in an air-tight glass container, taken out of the glove box, and attached to a freeze dryer (Labconco FreeZone) for freeze drying at -50℃ under 10 Pa vacuum for 2 days. The dried solids were weighed, ground by the mortar and pestle in anaerobic chamber, and stored in 10-ml serum bottles sealed with rubber stoppers for further analysis on X-ray diffraction (XRD)..

2.2.6. Removal and quantification of biomass associated with UO_2

In order to dissolve the biomass associated with uraninite solids for quantification, we first washed the solids with a anoxic sterile $NaHCO_3$ solution three times (in order to remove remaining uranyl associated to the UO_2 surface) and then separated into two groups: Group A with further NaOH washing (three times, ten minutes per time; to destroy the cells and proteins) and Group B without NaOH washing. Afterwards, solids in both groups were separately washed with a $NaHCO_3$ solution three times again and then with anoxic sterile DI water three times. These solids were then freeze dried for two days. The dried powders were digested in 0.125 M

NaOH at 90℃ for 30 min and then filtered for prote in measurement using the same Coomassie protein blue method as described in 2.2.4.

2.2.7. X-ray diffraction (XRD) analysis

XRD was performed using a Rigaku D/Max-IIB diffractometer with monochromated Cu *K*α radiation. The powdered solids were packed into glass slides and immobilized by a steamed mixture of white petroleum jelly and n-hexane. The X-ray scanning featured a constant scanning speed of 0.75 deg/min from 5° to 90° 2 *Θ* and a step interval of 0.02° 2 *Θ*. XRD patterns were processed using the computer programs Jade (Materials Data, Inc., Livermore, CA) and Microsoft Excel (Microsoft Corp., Redmond, WA). The average particle sizes of the mackinawite in those samples were estimated by Jade on the basis of the Scherrer equation:

$$t = \frac{0.9\lambda}{B\cos\theta_{\mathrm{B}}} \qquad (2.1)$$

where t = thickness of the particles (Å), λ = wavelength of the incident X-ray (Å), B = full width at half maximum (FWHM) of the (0 0 1) peak (radian) based on instrumental correction using LaB6 standard powder, and θ_{B} is the Bragg angle (degrees) at the (0 0 1) peak[300-302].

2.2.8. X-ray photoelectron spectroscopy (XPS) analysis

X-ray photoelectron spectroscopy (XPS) was used to analyze surface elemental composition and chemical state of the dried solids. It was performed on a Vacuum Generators ESCALAB 220i-XL (Thermofisher, USA) with a monochromatic Al Kα source (hv = 1486.6 eV, line width = 0.7 eV for Ag 3d 5/2) at a base pressure = 7×10^{-10} mbar.

2.2.9. Transmission electron microscopy (TEM) analysis

The powdered sample was loaded on a Lacey carbon 300-mesh copper TEM grid (Ted-Pella, Inc., Redding, CA, USA). TEM images were captured using a Philips CM200-FEG high resolution TEM/STEM (FEI Corp., Eindhoven, The Netherlands) operated at 200 kV, and elemental compositions at selected areas were identified using an EDX detector (EDAX Inc., Mahwah, NJ, USA).

2.2.10. X-ray absorption spectroscopy (XAS) analysis

X-ray absorption spectroscopy (XAS) analysis of wet pastes of the solid materials was performed at the Stanford Synchrotron Radiation Lightsource (SSRL) under the help of researchers in University of Michigan. Uranium L_{III}-edge absorption spectra were collected in fluorescence mode at beamline 4-1 or 11-2 with a Lytle or 30-element Ge detector. The beam energy was calibrated to the maximum of the first feature of a $NaS_2O_3 \cdot 0.5H_2O$ sample at 2472.02 eV prior to data collection. During data collection, all samples were cooled using a liquid nitrogen cryostat (77 K) and underwent multiple scanning in order to improve the signal to noise ratios[252].

2.3. Results for U(VI) reduction and uraninite formation

2.3.1. Bacterial growth and UO_2 formation on U(VI) alone

Figure 2.1 illustrates the concentration changes of soluble U, lactate, and protein along the incubation time. U(VI) reduction started up with no delay and reached over 80% within 5 hours. After 30 hours, no soluble U was detectable, and the protein concentration had doubled. The estimated maximum specific rate of U(VI) utilization was approximately 1.89 e^- eq/gVSS-d. The value is close to what other researchers obtained in their tests under similar conditions, except that their initial protein concentrations were 4 – 5 times higher[108, 269, 303, 304] or even over 100 times higher[121]. This indicates that initial biomass did not limit U(VI) reduction when its concentration was over 15 mM as protein.

According to the stoichiometry in Eqns. 2.1 and 2.2, only 0.5 mole lactate is required to reduce 1 mole U(VI) to U(IV):

$$CH_3CHOHCOO^- + 2H_2O \rightarrow CH_3COO^- + H^+ + HCO_3^- + 2H_2 \qquad (2.1)$$

$$(UO_2)^{2+} + H_2 \rightarrow UO_{2(s)} + 2H^+ \qquad (2.2)$$

In this test, complete U(VI) reduction required about 0.4 mM lactate. Consequently, the 2-3% loss of lactate was not detectable on HPLC due to the limited sensitivity of the instrument.

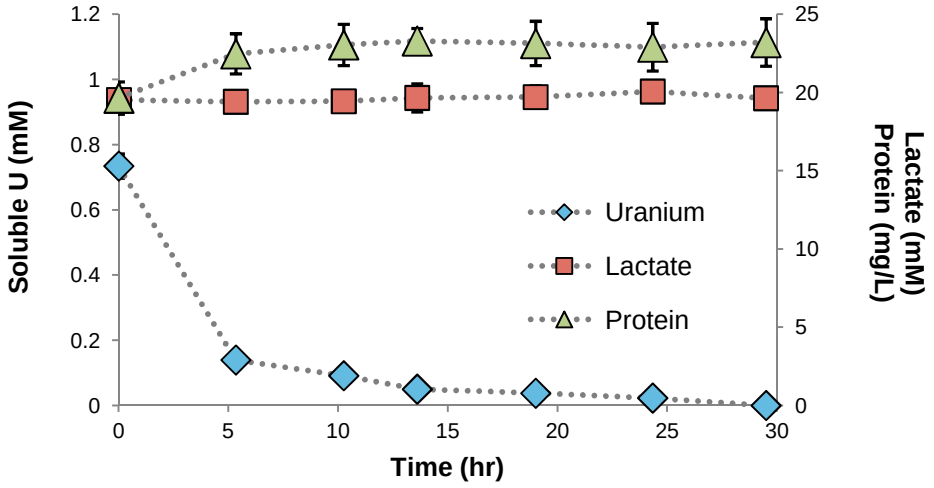


Fig 2.1 Concentrations of soluble U, lactate, and protein in the assay bottles inoculated with *D. vulgaris*.

Figure 2.2 illustrates the XRD spectra of the biogenic solids, and Table 2.2 summarizes the measured concentrations of protein associated with solids and calculated crystallite thickness. These data verify the presence of uraninite nanocrystallites with particle thickness of 3.9 – 4.0 nm. The proteins associated with the UO_2 solids were as high as 20 mg/g. With NaOH washing, almost 95% of the biomass was removed, but the characteristics of UO_2 solids, seen with the XRD patterns and particle thicknesses did not change. The underlying significance is that NaOH washing was an effective way to removed biomass from UO_2 solids without affecting crystallization process, and we were able to controllably produce similar-sized biogenic UO_2 nanocrystallites associated or not associated with biomass.

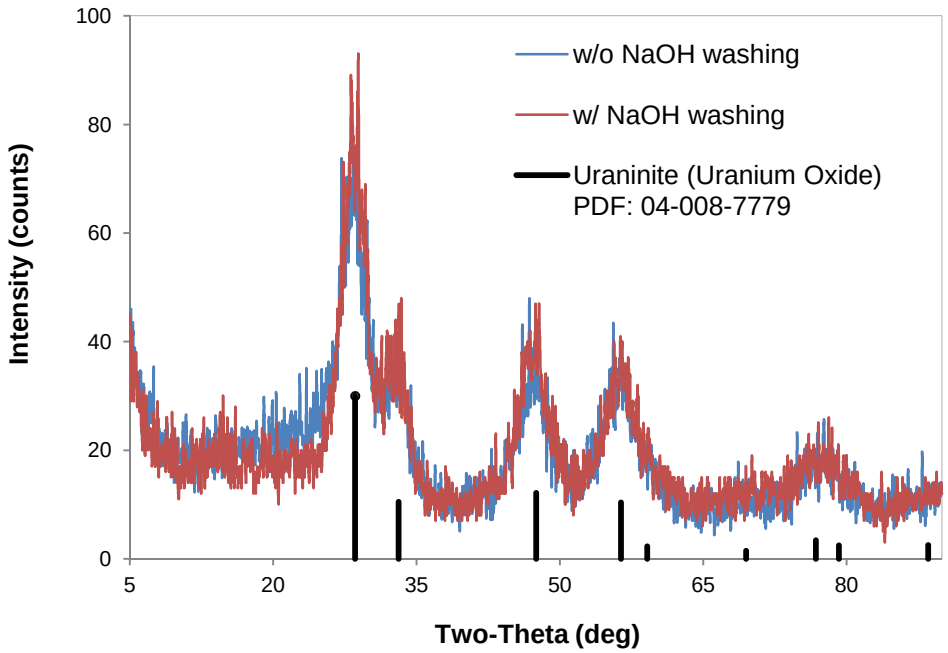


Fig 2.2 X-ray diffraction spectra of the biogenic solids with and without NaOH washing.

Table 2.2 Protein concentration and uraninite thickness of the biogenic solids with or without NaOH washing.

	Protein Conc. (mg / g)	Uraninite thickness (nm)
Solids w/o NaOH washing	20.1±2.6	3.9±0.9
Solids w/ NaOH washing	0.8±0.5	4.0±0.5

Figure 2.3 shows XPS spectra of the biogenic solids associated with biomass (i.e., without NaOH washing). The presence of only three elements -- uranium, oxygen, and carbon -- confirms that uranium oxides and organic matters were predominant at least on the solid surface. In addition, the obvious symmetry of U peaks with no shifting demonstrates the existence of U in only a single oxidation state and chemical bond. The binding energy of the U-$4f_{7/2}$ level, dependent on the oxidation state of U, was less than 380 eV after carbon calibration; this further confirms the single oxidation of +4[305, 306]. Absence of U(VI) indicates that $NaHCO_3$ washing effectively removed uranyl salts from the solid surface, and surface oxidation during solid separation, transferring and drying did not occur. Furthermore, there was a weak peak approximately 7 eV above the U-$4f_{5/2}$ peak, as pointed with the red arrow in Figure 2.3. It was one of the characteristic features of uraninite known as "shake-up satellites"[307].

The carbon-to-uranium atomic ratio from the XPS results was 1:0.4, while the same ratio calculated from the protein concentration (Table 2.2) was 1:4 (assuming a protein composition of $C_5H_7O_2N$, an empirical formula of biomass[308]). A higher carbon portion on the surface means that biomass was primarily located outside the UO_2 aggregates.

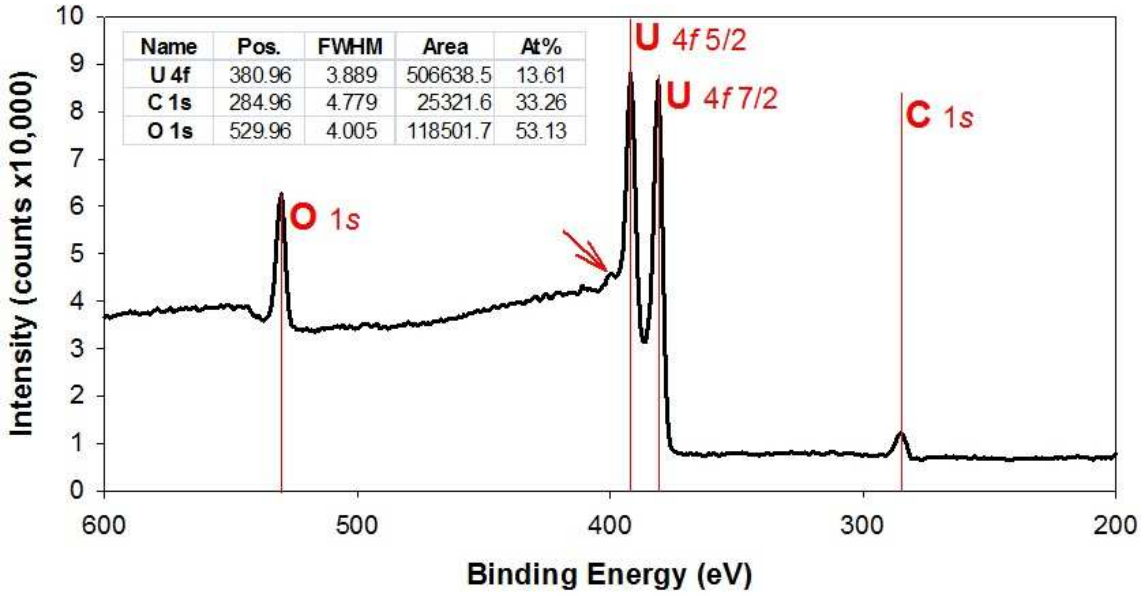


Fig 2.3 XPS spectra of the biogenic solids associated with biomass (without NaOH washing). The red arrow indicates the characteristic uraninite shake-up satellite peak.

Figure 2.4 shows the TEM image and EDX spectrum of the biogenic solids associated with the biomass. The elements detected by EDX scanning, besides C and Cu from the TEM grid, were only U and O. Consistent with the XPS result, this further confirms that uranium oxides and organic matters were most abundant components of the solid sample. The *d*-spacing of the observed particle lattice fringes was 3.12±0.2 Å. This is consistent with the structure of either synthetic uraninite[309] or biogenic UO_2 [189], and it indicates that the particle lattice fringes were dominated by the (111) *d*-spacing[189]. The thickness of individual crystallite calculated by multiplying the number of (111) fringes by the average *d*-spacing was 5.1±1.1 nm. This value is very close to the uraninite thickness calculated on basis of the XRD data (3.9 – 4.0 nm, shown above), and it is consistent with the average size of biogenic uraninite (2-10 nm),[179, 189, 310, 311] but slightly larger than the biogenic uraninite by *Shewanella* spp. in previous research[137, 139, 189, 304].

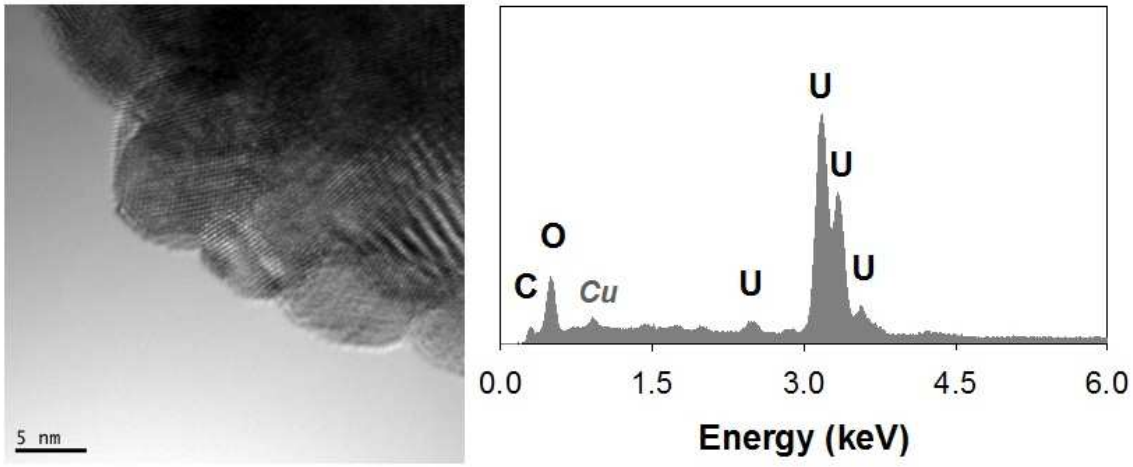
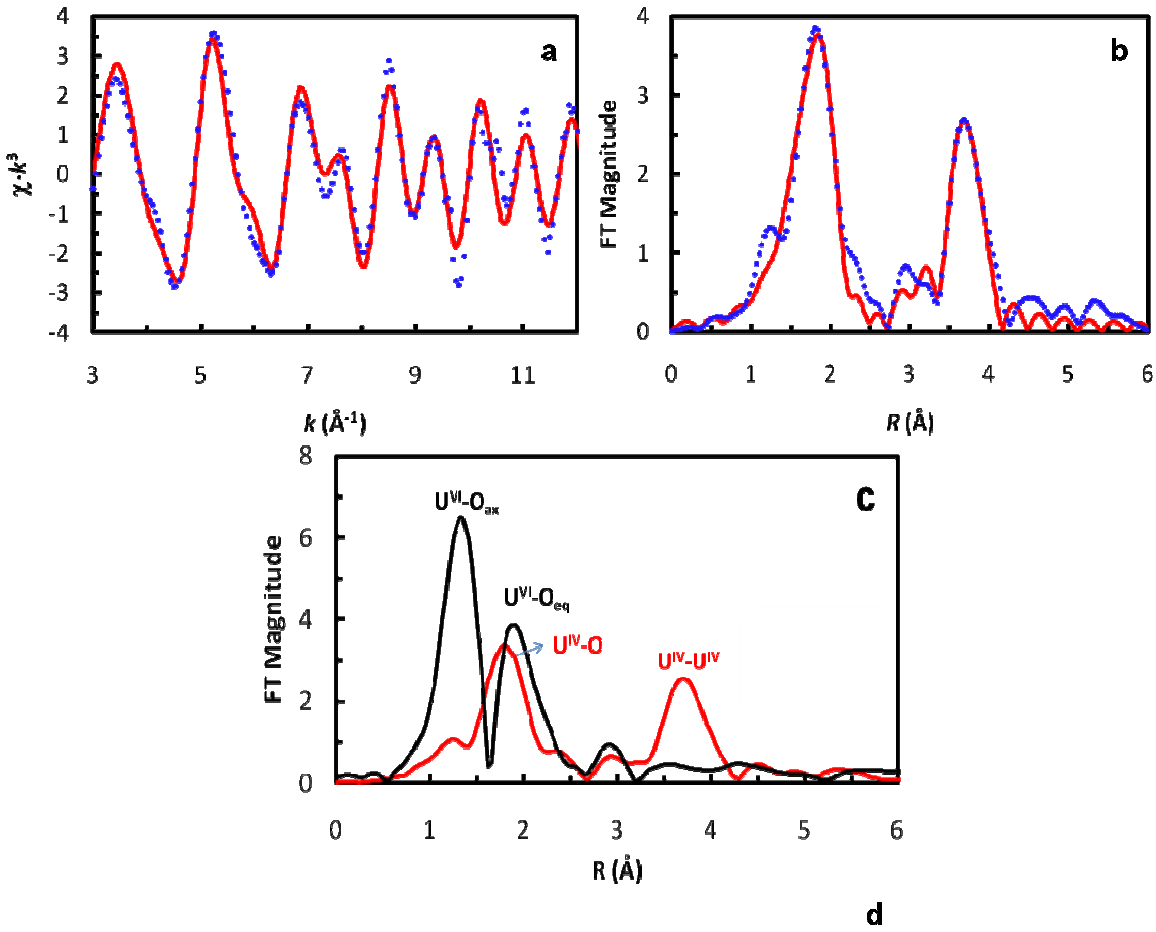


Fig 2.4 The TEM image and EDX spectrum of the biogenic solids associated with biomass (without NaOH washing).

Figure 2.5 shows the L_{III}-edge data for the biogenic solids associated with biomass, including the EXAFS, the associated Fourier transforms (FT) qualitatively compared with U(VI) (UO_2^{2+}), and the quantitative comparison with synthetic UO_2. The biogenic UO_2 shows a distinct FT peak pattern to UO_2^{2+} in the original medium (Fig. 2.5c), which corresponds well with the synthetic UO_2 in previous research[139, 189, 250, 252, 312]: All the FT peaks in synthetic UO_2 also were observed in the biogenic solids up to 6 Å interatomic distances and without energy shift of the adsorption edge. However, in contrast to synthetic UO_2, the biogenic UO_2 features a larger

amplitude of the U-O shell FT peak than the U-U shell FT peak; this conforms with the smaller coordination number of the U-U shell (Fig. 2.5d) and confirms its nanoparticulate size[139]. In addition, the Debye-Waller factors (σ^2) for both U-O and U-U shells of biogenic UO_2 were over twice as high compared to synthetic UO_2 (Fig 2.5d); this indicates the higher static disorder in biogenic UO_2 [189].



d

	Path	Coordination Number	Interatomic Distance (Å)	σ^2
Biogenic Uraninite	U^{IV}-O	7.2(8)	2.33	0.0122
	U^{IV}-U^{IV}	4.8(8)	3.84	0.0105
Synthetic Uraninite	U^{IV}-O	8.4(4)	2.36	0.007
	U^{IV}-U^{IV}	11(2)	3.87	0.0045

Fig 2.5 U L_{III}-edge data for the biogenic solids associated with biomass (without NaOH washing). (a) EXAFS spectra (solid line) collected at 77 K with fit to data (dots); (b) corresponding Fourier transforms (solid line) and fit to data (dots); (c) corresponding Fourier transforms of the biogenic solids (red line) and the standard uranyl [U(VI)] solution (black line); and (d) structural Parameters of biogenic UO_2 (produced in ASU) and synthetic UO_2 (produced in UofM) extracted from the EXAFS Analysis.

2.3.2. Bacterial growth and uraninite formation with presence/absence of sulfate and soluble Fe(II)

Table 2.3 summarizes pH values and concentrations of soluble U, SO_4^{2-}, Fe^{2+}, and biomass in the five assays at the beginning (right after inoculation) and at the end (right before solid separation), as well as the UO_2 thickness of the biogenic solids estimated on basis of XRD data. Figure 2.6 presents the concentration changes of lactate, soluble U, SO_4^{2-}, and Fe^{2+} in the five bottles during incubation. Figure 2.7 illustrates the XRD patterns of biogenic solids separated from the four inoculated bottles.

Fig 2.6 shows that U reduction occurred in all four inoculated assay bottles and went fastest in Bottle 3 (with only SO_4^{2-}), in which 90% uranium reduction took about 20 hours. In the other three inoculated bottles, uranium reductions were quite similar: ~ 70% U(VI) was removed within 80 hours.

Sulfate reduction also occurred in the two sulfate bottles (3 and 4). 90% sulfate reduction occurred within 10 hours in Bottle 3 (with only SO_4^{2-}), while SO_4^{2-} reduction in Bottle 4 (with both SO_4^{2-} and Fe^{2+}) was retarded during the first 2 days, but reached 90% within the third day.

Over 80% loss of soluble Fe^{2+} corresponded with sulfate loss in Bottle 4 (having SO_4^{2-} and Fe^{2+}), indicated the formation of FeS. 30% Fe^{2+} loss was also detected In Bottle 2 (Table 2.3); this is discussed below. Soluble Fe^{3+} was not detected in any bottles, indicating the well-maintained anoxic and reducing conditions (i.e., absence of Fe^{2+} oxidation).

Despite the reduction of most U(VI), lactate loss and acetate accumulation were negligible in Bottles 1 and 2 (without SO_4^{2-}). In contrast, considerable lactate loss and acetate accumulation were detected in bottles 3 and 4 (with SO_4^{2-}). This difference is the result of the electron-accepting equivalents of U(VI) and sulfate. According to stoichiometry, 2 and 8 e^- eq/L are required to completely reduce 1 mole U(VI) and 1 mole SO_4^{2-}, respectively. Thus, only 0.5 mM lactate was needed for total 1 mM U(VI) reduction, and this formed 0.5 mM acetate. These differences were not detectable by HPLC. By contrast, lactate removal and acetate formation for SO_4^{2-} reduction were 2 mM, which was detectable.

These results add weight to the observation by Spear et al. that a *D. desulfuricans* culture exhibited a faster rate of uranium reduction in the presence of sulfate and no lag time, in contrast to U alone[303]. However, sulfate reduction started up without lag in our case, while Elias et al. observed that sulfate reduction by *D. vulgaris* was transiently inhibited until 90% soluble U(VI) loss and the loss rate began to decrease[121]. Free sulfide accelerated the U(VI) reduction rate in Bottle 3, as the abiotic reduction of U(VI) by dissolved sulfide was shown in previous studies[313-315]. Furthermore, Spear et al. showed that *D. desulfuricans* reduced U(VI) faster in the presence of sulfate reduction and suggested that the biogenic sulfide may have been responsible for the increased rate of U(VI) reduction.

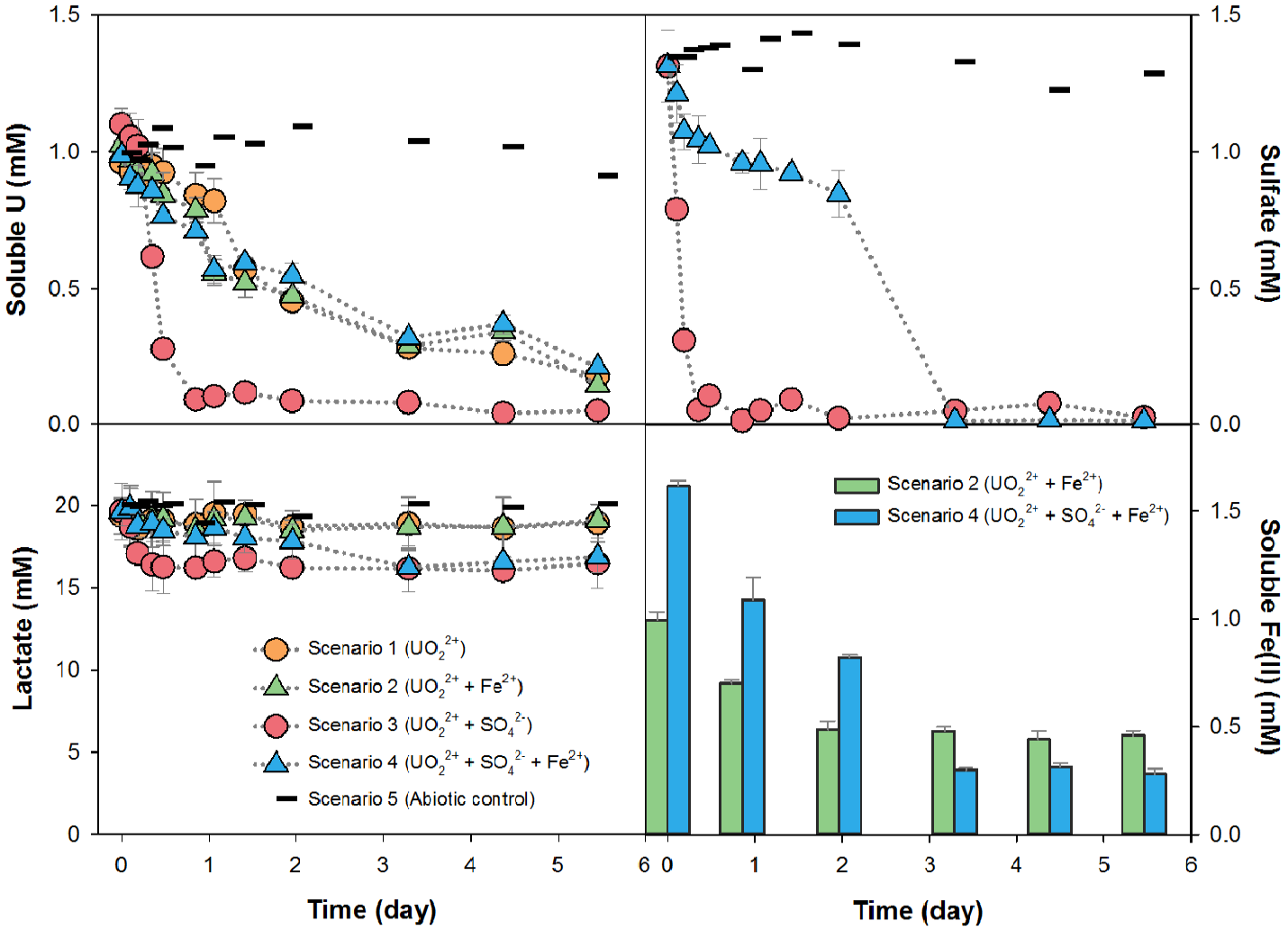


Fig 2.6 Concentrations of soluble U(VI), sulfate, lactate and acetate for Scenarios 1 (UO_2^{2+} alone, ●), 2 (UO_2^{2+} + Fe^{2+}, ▲), 3 (UO_2^{2+} + SO_4^{2-}, ●), 4 (UO_2^{2+} + SO_4^{2-} + Fe^{2+}, ▲), and 5 (abiotic control, -); and concentrations of ferrous (bars) under Scenarios 2 and 4.

Table 2.3 pH, concentrations of soluble U, SO_4^{2-}, Fe^{2+} and biomass in the five assay bottles in the second test under the initial conditions (Day 0) and the final conditions (Day 7); the UO2 thickness of the biogenic solids from the four inoculated bottles estimated on basis of XRD data.

Bottle	Day 0					Day 7					Solids
	Soluble U (mM)	SO_4^{2-} (mM)	Fe^{2+} (mM)	Biomass (mg/L protein)	pH (s.u.)	Soluble U (mM)	SO_4^{2-} (mM)	Fe^{2+} (mM)	Biomass (mg/L protein)	pH (s.u.)	UO_2 thickness (nm)
1	0.96	–	–*	10.0	7.6	0.18	–	–*	15.1	7.6	3.23
2	1.03	–	1.00	7.3	7.3	0.14	–	0.76	9.6	7.5	1.37
3	1.10	1.31	–*	7.6	7.5	0.05	0.03	–*	23.5	7.5	3.10
4	0.99	1.31	1.62	9.0	7.4	0.21	0.01	0.31	16.6	7.4	0.83
control	0.99	1.34	1.42	–	7.4	0.92	1.29	1.37	–	7.5	-

* The 0.03 mM $FeCl_2$ in the basic assay solution was below the detection limit of the SSA method and thus undetectable.

As shown in XRD patterns (Fig. 2.7), biogenic UO_2 was present in all four solid samples. As indicated by the sharper characteristic XRD peaks (Fig. 4.7) and thicker particulates (Table 2.3), UO_2 in Bottles 1 and 3 (no Fe^{2+}) were larger crystallites than UO_2 in Bottles 2 and 4 (with Fe^{2+}). This suggests that the presence of Fe^{2+}, either dissolved or precipitated, may have inhibited the crystallization process of biogenic UO_2. Recent studies featuring UO_2 mixed with cations such as Mn(II)[316] and Zn(II)[189] showed similar inhibitive effects. The proposed mechanisms were the incorporation of impurity ions into UO_2 and/or the adsorption of these ions on the UO_2 surfaces. A 30% loss of soluble Fe^{2+} under the sulfide-free condition (Bottle 2; Table 2.3) was probably due to adsorption and/or incorporation to biogenic UO_2 and thus adds weight to this hypothesis.

Neither mackinawite nor other iron-sulfide crystals was detected in Bottle 4 (with SO_4^{2-} and Fe^{2+}; Fig 2.7D), albeit iron-sulfide precipitation was indicated by concomitant losses of SO_4^{2-} and soluble Fe^{2+} (Fig 2.6), as well as the very black color in the solution. Two hypotheses can be proposed: 1) The FeS was still in an amorphous phase, probably indicating an inhibitory effect of remaining soluble Fe^{2+}; 2) Part of the sulfide was oxidized to elemental sulfur (S^0) during U(VI) reduction, but the S°was amorphous and not detecte d by XRD.

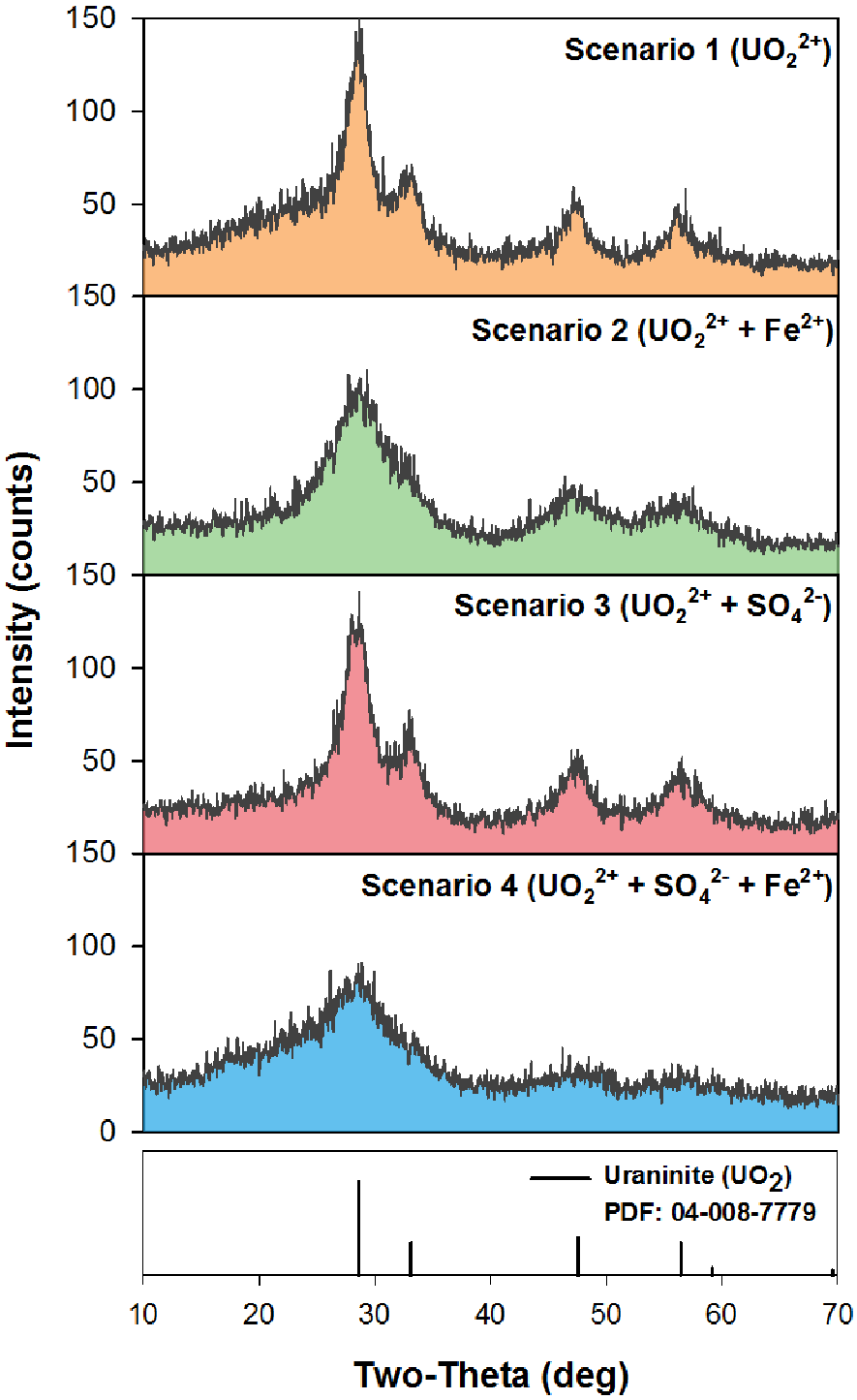


Fig 2.7 XRD spectra of solids separated from the bottles for Scenarios 1 (UO_2^{2+} alone), 2 (UO_2^{2+} + Fe^{2+}), 3 (UO_2^{2+} + SO_4^{2-}), and 4 (UO_2^{2+} + SO_4^{2-} + Fe^{2+}).

2.4. Conclusion

D. vulgaris was able to grow on respiration of U(VI) alone. The estimated maximum specific rate of U(VI) utilization was 0.64 e^- eq/gVSS-d when the initial inoculum was 15 mg/L in protein. *D. vulgaris* reduced uranyl (UO_2^{2+}) to nanocrystallite uraninite (UO_2) with an average thickness of 4-5 nm. Compared to synthetic UO_2, biogenic UO_2 by *D. vulgaris* had smaller size, higher static disorder, and about 20 mg/g associated biomass.

The patterns of U(VI) reduction and UO_2 production by *D. vulgaris* were distinguishable according to the presence or absence of sulfate and Fe(II). *D. vulgaris* reduced U(VI) and sulfate concomitantly when both electron acceptors were present. In addition, biogenic sulfide abiotically reduced U(VI) as well and accelerated the overall U(VI) immoblization; this process, however, did not take place in presence of soluble Fe(II), because Fe(II) rapidly scavenged sulfide by forming FeS precipitates. The presence of Fe(II) probably also inhibited crystallization of biogenic UO_2 and FeS due to the proposed mechanism of adsorption onto UO_2 surfaces and/or incorporation into UO_2 structure.

CHAPTER 3. U(VI) reduction in a MBfR inoculated with *D. vulgaris*

3.1. Introduction

The goal of this chapter is to present and interpret the performance of an MBfR inoculated with *D. vulgaris* for U(VI) reduction. This was a collaborative research project between Aura Ontiveros-Valencia and me. I presented part of the results in the 9th International Conference on Biofilm Reactors held by International Water Association (IWA) in Paris, France, May 28 – 31, 2013. I prepared one manuscript based on these results. The title is "Uranium removal and microbial community in a H_2-based membrane biofilm reactor". The authors are Chen Zhou, Aura Ontiveros-Valencia, Alexander Zevin, Sara Carey, Rosa Krajmalnik-Brown, and Bruce E. Rittmann. The manuscript being reviewed by the co-authors and will be submitted to *Water Research*. The methods, results, and discussion in the chapter are the same as in the manuscript, although the introductory material was relocated to Chapter 1.

3.2. Experimental setup

3.2.1. MBfR Setup

A schematic of the MBfR used in this study is shown in Figure 3.1. The MBfR system consisted of two glass tubes connected with Norprene tubing, polycarbonate stopcocks, and plastic barbed fittings. One glass tube contained a main bundle of 49 hollow-fiber membranes (nonporous polypropylene fiber, 200 μm OD, 100-110 μm ID, wall thickness 50-55 μm; Teijin, Ltd., Japan), each 25 cm long. Biofilm samples are collected by cutting short lengths of a separate fiber from the "coupon" bundle of 10 fibers, located in the second glass tube. This allowed sample collection without disturbing the main bundle of fibers and without causing a significant change in total biofilm surface area in the reactor. The experimental permeability of the polypropylene fiber was 1.8×10^{-7} m^3 H_2 • m membrane thickness / m^2 hollow fiber surface area • d • bar at standard temperature and pressure [317].

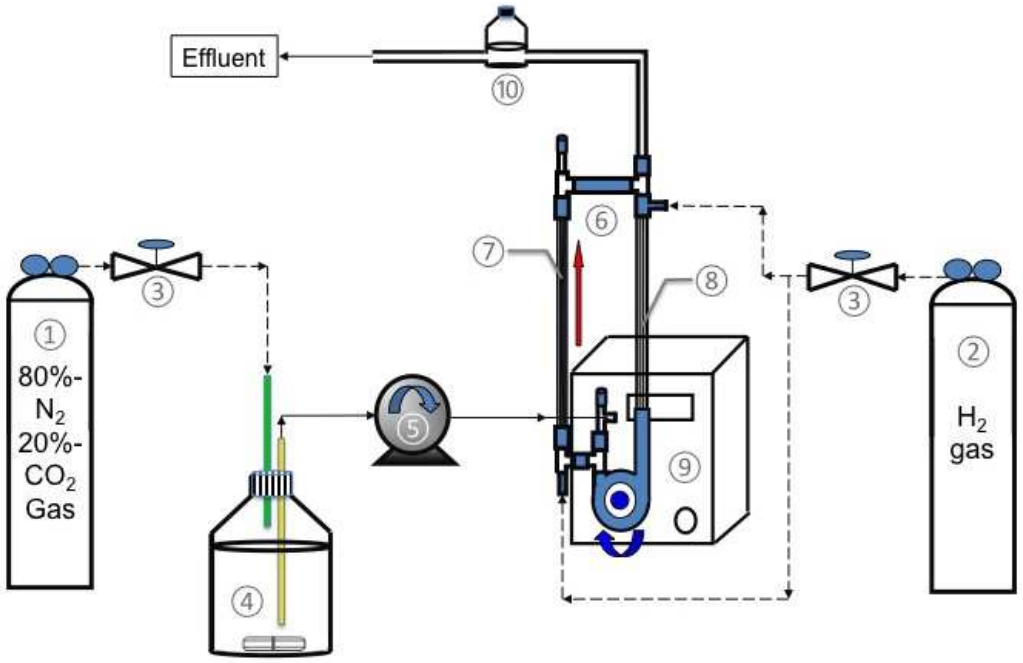


Fig 3.1 Schematic of the bench-scale MBfR system used to investigate U(VI) reduction. The major components include: ① mixed gas tank with 80% N_2 and 20% CO_2 to feed the headspace of the medium bottle; ② pure H_2 gas tank to feed the fiber bundles of the MBfR; ③ gas pressure regulators; ④ medium bottle with a stir bar; ⑤ feeding pump; ⑥ MBfR configuration (the red arrow indicates the flow direction; ⑦ main bundle with 49 fibers; ⑧ biofilm sampling bundle with 10 coupon fibers; ⑨ recirculation pump; and ⑩ small serum bottle for gas sampling. The black solid arrows indicate the liquid flow, and the black dashed arrows indicate the gas flow.

For the main fiber bundle, both ends were glued into an H_2-supply manifold. For the "coupon" bundle, the top was glued into an H_2-supply manifold, but the bottom was sealed and not fixed to the end of the tube. The MBfR was completely mixed using a high recirculation rate of 150 mL/min achieved with a peristaltic pump (Master Flex, model 7520-40, Cole-Parmer Instrument Company, U.S.A); therefore, the concentration in the MBfR was equal to the effluent concentration. A peristaltic pump (Rainin Dynamax Peristaltic pump, model RP-1) and PVC tubing (Rainin Silicone pump tube, Yellow Blue) provided an influent feed rate within the range of 0.03 – 3.00 mL/min. The H_2 pressure supplied to the MBfR was 23 psi (1.6 atm) throughout all experiments. A top-sealed 15-ml serum bottle was connected after the effluent line in order to create inside a ca. 7-ml headspace for collecting gas samples (Fig 3.1, ⑩).

3.2.2. Strain, culturing, and biomass preparation

The MBfR was inoculated with the same *D. vulgaris* culture in the previous studies and followed the same the procedure of biomass preparation in Section 2.2.2.

3.2.3. Feeding medium

We prepared and stored the feeding medium in a 5-L glass bottle (VWR, Radnor, PA). We sealed the bottle air-tight with a rubber stopper containing one outlet from the liquid phase and one inlet to the headspace. The basic medium consisted of (in mM) UO_2Cl_2 0.5, CH_3COONa 0.05, $NaHCO_3$ 30, KCl 1, NH_4Cl 0.2, $CaCl_2$ 0.002, $MgCl_2$ 0.01, $FeCl_2$ 0.01, $NiCl_2$ 0.01, and 5 mL trace metal solution. The acetate concentration was set to be twice that required by stoichiometry for complete reduction of 0.5 mM U(VI)[273]. The composition of the trace metal solution was described by Chung et al.[289]. All the components except UO_2Cl_2, $FeCl_2$, and $NiCl_2$ were added at the beginning. Immediately after being autoclaved for deoxygenation and sterilization, the medium bottle was transferred to the glove box. UO_2Cl_2 powder and $FeCl_2$ + $NiCl_2$ concentrate solution were added in the glove box after the medium cooled to room temperature. Once outside the glove box, the medium bottle was sparged by 80% N_2 / 20% CO_2 premixed gas for 2 hours to make it ready for feeding. The 80% N_2 / 20% CO_2 gas was supplied subsequently to the headspace at <2 psi. The small positive pressures in the sealed medium bottle maintained the soluble carbonate level and minimized oxygen intrusion from outside. In consequence, influent pH was maintained at 7.5±0.3 until we reduced the bicarbonate concentration in the medium in the last month, and influent D.O. levels were maintained minimal (< 10 ppb) during the entire operation.

3.2.4. Inoculation, startup, and operation

We inoculated the MBfR with 10 mL (17% of the total reactor volume) of a freshly prepared *D. vulgaris* biomass suspension after filling the reactor with medium. The initial suspending biomass in the bulk liquid was 120-150 mg/L as protein.

Most denitrifying MBfRs start continuous feeding after short-term batch mode, typically up to 24 hours[284, 295, 318, 319]. However, U(VI) reducers, as well as other metal reducers, grow more

slowly than denitrifiers and may need a more extensive opportunity to colonize the membrane. Furthermore, our preliminary results using the typical start up method (not shown) failed to produce enough biofilm accumulation to allow noticeable U(VI) reduction. Thus, we adapted the startup procedure used successfully for a TCE-reducing MBfR featuring *Dehalococcoides*, a group of slow-growing dehalogenators[296].

In Stage 1, after being inoculated with the freshly prepared biomass suspension, the reactor remained in an extended batch mode for 9 days, followed by semi-continuous operation: in each cycle of semi-continuous operation, we fed the reactor at a flow rate of 0.20 ml/min for 24 hours, and then we stopped feeding for the next three days. Upon observing stable U removal after four cycles of semi-continuous mode, we initiated continuous operation at a flow rate of 0.04 mL/min. This stage lasted 118 days, and we increased the flow rate to 0.08 mL/min on day 113. In Stage 2, we added into the medium 0.125 mM sulfate (in Na_2SO_4) as the additional electron acceptor at the same electron equivalents as uranyl (1 mEq e^-/L). The flow rate was kept at 0.04±0.003 mL/min through this stage.

3.2.5. Sampling and analyses

For routine analyses, we collected liquid samples from the MBfR with 6-mL syringes and filtered part of them immediately through 0.2-μm membrane filters (LC+PVDF membrane, Whatman Inc., Haverhill, MA). The methods for measuring concentrations of soluble U, sulfate, acetate and other volatile fatty acids are described in 2.2.4.

For pH and dissolved oxygen (D.O.) assays, we took 8-mL liquid samples with 10-mL gas-tight syringes (Hamilton Company, Reno, NV), injected them into sealed anaerobic 10-mL serum bottles, and then put the serum bottles into the glove box for analyses. We measured pH values of the unfiltered samples with an Epoxy Semi-Micro Combination pH Electrode (Beckman Coulter BKA57187) and a pH Meter (Beckman Coulter BKA58734). We measured D.O. of the unfiltered samples by the Rhodazine D™ Method test kits (CHEMetrics K-7501, K-7599 and K-7512.

For H_2 and CH_4 analysis, we injected 100-μL headspace samples collected from the post-reactor serum bottles with 500-μL gas-tight syringes (Hamilton Company, Reno, NV) into a gas

chromatography (Shimadzu GC-2010) equipped with a thermal conductivity detector (TCD) and a flame ionization detector (FID), respectively. The standard deviations of the measurements for H_2, and CH_4 concentrations were 0.06 atm and 0.01 atm, respectively (n = 3 samples).

3.2.6. Flux calculation

We calculated the U removal fluxes (e^- mEq/m^2-day) according to Eqn. 3.1

$$J = \frac{(S^0 - S)Q}{A} \quad (3.1)$$

where S^0 and S are the influent and effluent U concentration (e^- mEq/L), Q is the influent flow rate to the MBfR system (L/d), and A is the membrane surface area (m^2). The maximum H_2 delivery capacity (e^- mEq/m^2-day) was calculated from Tang et al.[320].

3.2.7. DNA extraction and pyrosequencing analysis

We sampled the biofilms in Stage 1 and Stage 2. We followed the procedures of biofilm separation and DNA extraction described by Ziv-El et al.,[321] Zhao et al.,[295] and Ontiveros-Valencia et al.[319]. The only exception is that in the end of Stage 2, we stopped the hydrogen gas supply and placed the whole reactor module into the glove box before opening it up.

We sent all DNA samples for pyrosequencing at the Research and Testing Laboratories LLC (Texas, USA). We processed the raw data using QIIME 1.7.0 suite[322] as described in Ontiveros-Valencia et al. [319]. We assigned taxonomy to OTUs with BLAST using the SILVA database and constructed Newick-formatted phylogenetic trees using FastTree[323].

3.2.8. Solid separation and characterization

After sampling the biofilm in the end of Stage 2, we took out the whole coupon fiber bundle and cut off a few fiber pieces in 0.5-1 cm length for TEM-EDX analysis. These fiber samples were directly incubated in the fixative, 2% glutaraldehyde in Dulbecco's phosphate-buffered saline (D-PBS), at pH 7.2 for 30 minutes; this incubating step was repeated after the fibers were encased in 1% agarose. After this, the encased fibers were washed in D-PBS three times (15 minute each) and incubated in 1% osmium tetroxide in D-PBS for 1 hour. After this, the fibers were washed with deionized water four times (10 min each) and dehydrated in graded

acetone series with 20% increments (10 min per step). The fully dehydrated fibers were infiltrated with graded series of Spurr's[324] epoxy resin in 25% increments for 54 hours. All the steps above were at room temperature. The fibers were polymerized in flat molds at 60^{o}C for 24 hours. The polymerized blocks were trimmed and thin-sectioned in a Leica Ultracut-R ultramicrotome at 70 nm thickness. These sections were then ready for TEM-EDX analysis. The detailed information of the analysis is described in 2.2.9.

For XRD analysis, we washed out most of the precipitates on the remaining fibers by vigorously rinsing the bundle in a 200-mL beaker containing freshly-prepared sterile anoxic 15 mM $NaHCO_3$ solution. After overnight precipitation, we removed most supernatant and transferred the rest solids into 50-mL falcon tubes. The subsequent rinse and drying steps were same as described in Chapter 2. After freeze drying, we transferred the grounded solids in 10-mL serum bottles sealed with rubber stoppers in the glove box and stored the bottles in the -20^{o}C freezer. The detailed information of XRD analysis is described in 2.2.7.

3.3. Results

3.3.1. Stage 1 – U(VI) as the sole electron acceptor

Figure 3.2 shows the measured flow rate and U concentrations, as well as calculated U-removal percentage, U surface loading, and U-removal flux, during Stage 1. During the first 6 days in batch mode, 98% of the influent U was removed, and Figure 3.3 shows that black-colored solids were observable around the fiber bundles, verifying successful biofilm formation and U precipitation. After two cycles of semi-continuous operation, the U-removal ratio increased to 99.6%, with the effluent U concentration dropping to 0.002 mM. When continuous mode began, the U removal slightly decreased to 95%, but rebounded and reached steady state at over 97%, with an average effluent U concentration of 0.01 mM and an average U surface loading of 5.9 e^- mEq/m^2-day. The average U surface loading was lower than the nitrate loading in denitrifying MBfRs of similar design (20-200 e^- mEq/m^2-day)[282, 295, 319] mainly due to the lower flow rate.

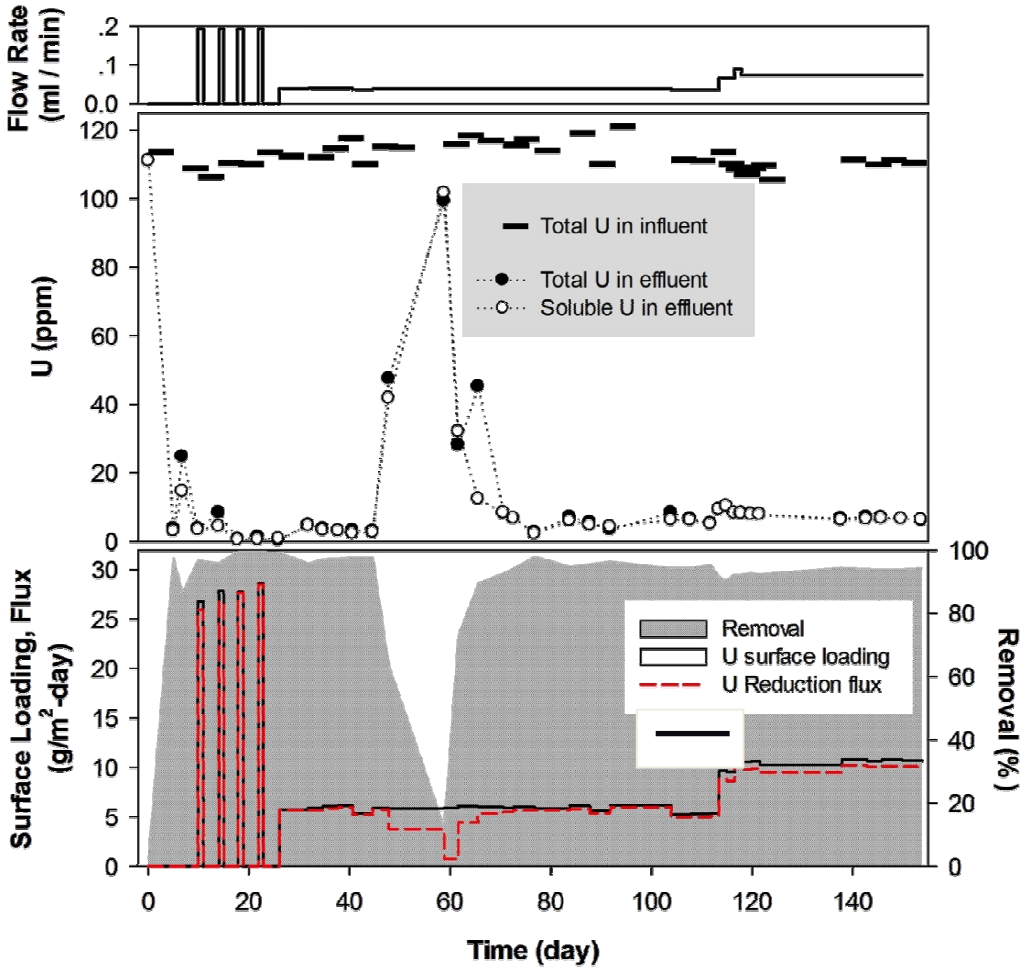


Fig 3.2 Measured flow rate (top), measured U concentrations in influent and effluent (middle), and calculated U-removal percentage, U surface loading, and U-removal flux (bottom) in Stage 1.



Fig 3.3 A photograph of a part of the main fiber bundles in the MBfR, with associated black-colored solids, taken after 9 days of continuous operation in Stage 1.

After 19 days of continuous operation, we sampled the fiber biofilm. This process exposed the reactor to the air for 5 minutes, and this exposure seemed to affect greatly the reactor's performance for up to 28 days. The temporary O_2 intrusion seemed to inhibit the activity of the anaerobic bacteria, perhaps by competing with U(VI) as the electron acceptor for H_2 oxidation. Moreover, some of the precipitated UO_2 was oxidized and dissolved. As a result, the U concentration in the effluent increased to 100 ppm, and net U removal dropped to only 12% for 14 days. Subsequently, the U concentration in the effluent decreased so that the U removal returned to 95% after another 14 days. From that point, the system performed steadily for the next 39 days. Thus, O_2 exposure had far-reaching impacts on microbial activities and UO_2 dissolution, but the biofilm community also had the capacity for self-recovery.

On the 113th day of this stage, we doubled the U surface loading by increasing the flow rate two-fold. U removal dropped to 91% within 3 days, but rapidly rebounded to 93-94% after another 3 days, after which the system performed stably for 35 days.

The average steady-state performance parameters for the two flow rates -- including HRT, U surface loading, U removal flux, effluent U concentration, and U removal -- are summarized in Table 3.1. The fact that the U-removals for the two flow rates were almost the same indicates that a U(VI)-surface loading as high as 11 e^- mEq/m^2-day in MBfR did not approach a loading threshold based on the maximum H_2 delivery capacity (113 e^- mEq/m^2-day at 23 psig in the nonporous polypropylene fiber), U(VI)-reduction kinetics, U(VI) mass transport, or build up of UO_2 in the biofilm.

Table 3.1 The average performance parameters at steady state for the two flow rates.

		Days 73 - 112	Days 119 - 154
Flow rate	10^{-2} mL/min	3.9 (<0.1)*	7.4 (<0.1)
HRT	hr	27 (2)	14 (0)
U surface loading	e^- mEq/m^2-day	5.7 (0.4)	10.7 (0.1)
U removal flux	e^- mEq/m^2-day	5.4 (0.4)	10.1 (0.1)
$[U]_{eff}$	10^{-2} mM	2 (<0.1)	3 (<0.1)
U removal	%	95 (1)	94 (<0.1)

* Numbers in the parentheses are the standard deviations of the average parameter values.

3.3.2. Stage 2 – U(VI) and sulfate as concomitant electron acceptors

In Stage 2, we supplemented the medium with sulfate as a second electron acceptor. Figure 3.4 shows the concentrations and fluxes of U and sulfate in Stage 2. Unexpectedly, sulfate reduction was insignificant throughout the 94 days of operation. U removal reached 96% within 3 days, but slowly decreased during the following 45 days, reaching a steady state at 81±1% for the next 21 days. On the 69th day, we reduced the bicarbonate concentration in the medium from 30 mM to 15 mM. U removal subsequently increased to 95% within 7 days and remained there until we opened up the reactor for sampling 18 days later.

The average performance parameters of these two steady-state conditions with different bicarbonate dosages are summarized in Table 3.2. One factor possibly affecting U-removal is pH. The primary U(VI) species at neutral pH are $(UO_2)_2(CO_3)_2^{2-}$ and $(UO_2)_2(CO_3)_3^{4-}$, but $(UO_2)_2(CO_3)_3^{4-}$ is predominant over $(UO_2)_2(CO_3)_2^{2-}$ when pH is higher than 8.[15-19] U(VI) reduction coupled with H_2 oxidation by biofilms releases free bicarbonate and also consumes protons:

$$UO_2(CO_3)_2^{2-} + H_2 \rightarrow UO_2 + 2HCO_3^- \qquad (5.1)$$

$$UO_2(CO_3)_3^{4-} + H_2 + H^+ \rightarrow UO_2 + 3HCO_3^- \qquad (5.2)$$

These reactions caused a remarkable pH increase in the reactor -- from about 7.5 to 8.8 for 30 mM bicarbonate in influent – even though the measured alkalinity changed little. Halving the bicarbonate addition caused a noticeable pH decrease in the influent medium. However, the reduced buffer capacity, due to less bicarbonate, along with increased bicarbonate release and proton consumption from enhanced U(VI) reduction, caused a sharp pH increase, from 6.6 to 8.8, as high as for 30 mM bicarbonate.

Since the pH was not changed, the decrease of U removal for 30 mM bicarbonate probably was due to direct inhibition of U bioreduction from bicarbonate itself[161, 162]. In particular, earlier research[325] discovered that reducing bicarbonate concentration from 40 mM to 10 mM stimulated sporulation, and our TEM imaging and pyrosequencing data (shown below) support the presence of *Clostridiaceae* spores in the biofilm in Stage 2.

Table 3.2 The average performance parameters at steady state under two HCO_3^{2-} conditions.

		Days 48 - 69	Days 76 - 94
Bicarbonate in influent	mM	30	15
pH in influent	c.a.	7.7 (0.1)	6.6 (<0.1)
pH in effluent	c.a.	8.8 (<0.1)	8.8 (0.1)
Alk. in influent	mg/L as $CaCO_3$	1860 (46)	783 (26)
Alk. in effluent	mg/L as $CaCO_3$	1815 (76)	777 (28)
U removal flux	e^- mEq/m^2-day	4.6 (0.1)	5.6 (<0.1)
$[U]_{eff}$	10^{-2} mM	9.5 (0.8)	5.5 (0.1)
U removal	%	81 (1)	95 (<0.1)

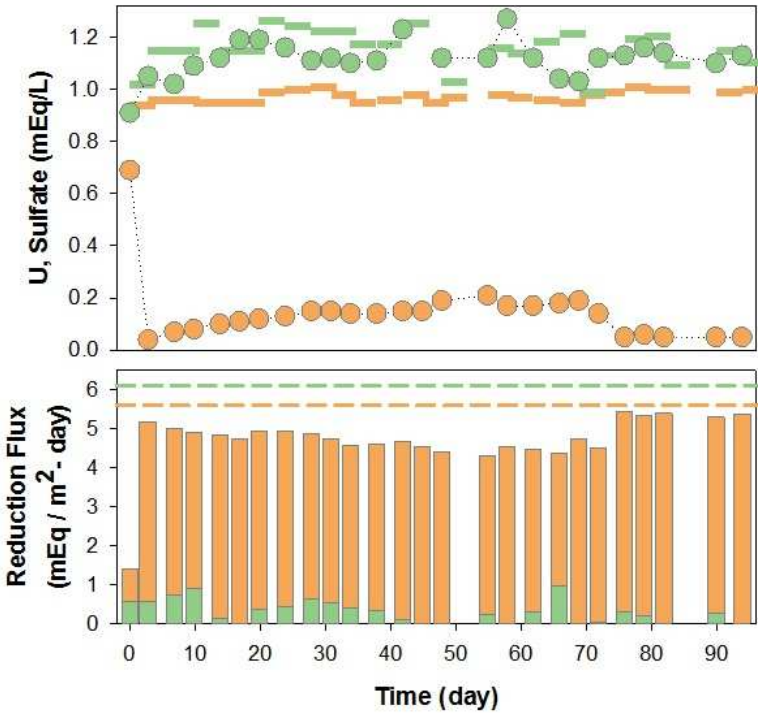


Fig 3.4 Top: concentrations of soluble U (orange color) and sulfate (green color) in influent (bars) and effluent (circles) of the MBfR in Stage 2. Bottom: reduction fluxes (bars) and average surface loadings (dashed lines) of soluble U (orange color) and sulfate (green color) in the MBfR in Stage 2.

3.3.3. Solid characterization of biofilm samples

Fig 3.5, which shows the XRD pattern of the solids separated from the whole coupon fiber bundle, reveals the presence of crystallite UO_2 with a thickness of 4.0±0.2 nm after over 8 months operation. The size is almost the same as for the biogenic UO_2 by *D. vulgaris* in my 30-hour batch tests (Table 2.2); this indicates that crystallization of UO_2 was rapid, but its aging was very slow.

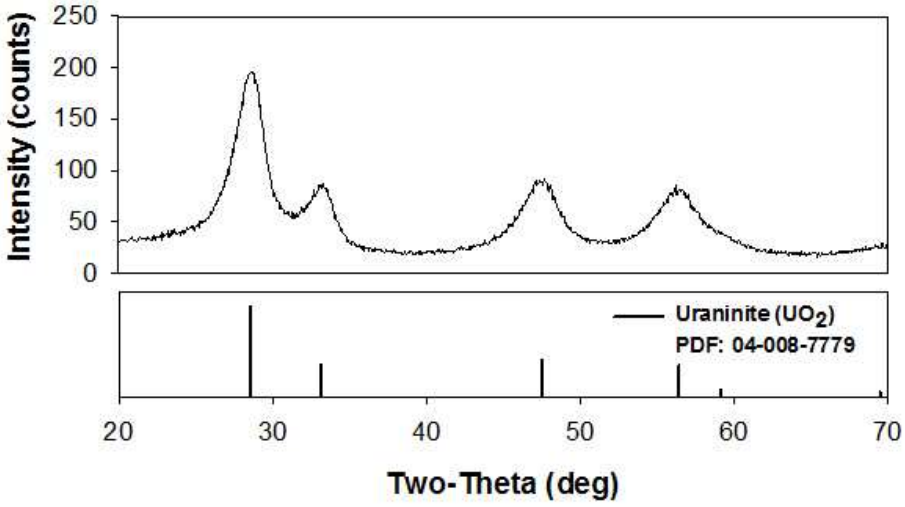


Fig 3.5 X-ray diffraction spectrum of the solids separated from the whole coupon fiber bundle in the MBfR.

Figures 3.6 – 3.9 present the TEM images and EDX spectra of selected locations in the fixed fiber sample. The image of the whole fiber cross-section in Figure 5.6A reveals that a thin layer of biofilms mixed with precipitates was formed around the outside wall of the hollow fiber. Magnified images of selected locations further reveal that most UO_2 crystallites, confirmed by the lattice fringes in Figure 3.6B and EDX patterns in Figure 3.8, formed μm-sized aggregates throughout the biofilm matrix. A significant portion of the aggregates attached directly on the fiber surface in a relatively organized arrangement, while microorganisms grew outside the aggregates and were scarcely able to reach the fiber surface; in some places, two layers of U aggregates sandwiched microbial cells (Figs 3.6C and 3.7).

U precipitates also were strongly associated with microbial cells (Fig 3.6D), and Figure 3.8 reveals that precipitates were located on the cell membrane, inside the cell, or associated with extracellular polymers in-between cells (indicated by higher C-to-U signals in the EDX spectra). In particular, some cells were encrusted by U and probably had undergone lysis as a consequence, a common phenomenon previously observed during metal immobilizations by biofilms[326, 327].

Figs. 5.6C and E show plentiful round-shaped structures that are similar in size and morphology to mature spores produced by *Clostridium* spp.[328-330]. U precipitates also appear in close proximity to the exosporium-like surface, the outermost shell surrounding the mature spore[331] (Figs 3.6F and 3.9); this proximity is consistent with what Vecchia et al.[331] observed in batch tests of U(VI) reduction by spores of *Clostridium acetobutylicum*.

In contrast to crystalline phase of the UO_2 aggregates, the U precipitates associated with cells and putative spores were mostly in amorphous gel-like phases; this indicates the presence of amorphous UO_2 and/or U(VI) immobilized by adsorption. We have not yet been able to access technology (e.g., XANES) that will allow us to differentiate elemental oxidation states and chemical bonds at certain locations of a heterogeneous microenvironment.

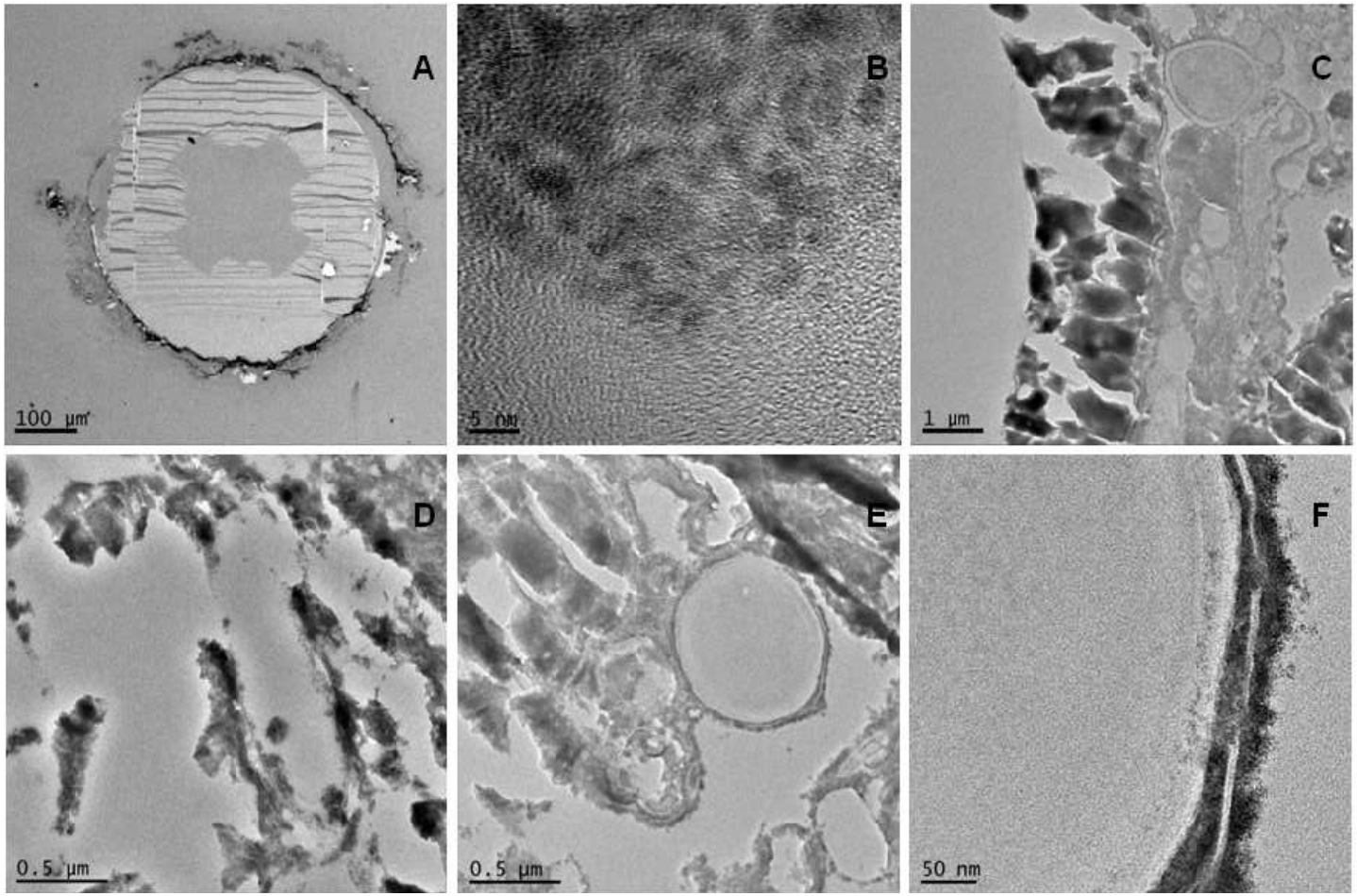


Fig 3.6 TEM images of various locations in the fixed cross section of a single fiber with biofilm. In some places, biofilms look detached from the fiber wall; this was because the epoxy resin we used for TEM did not completely penetrate into the biofilm matrix due to the abundant presence of the U metal, and thus the fixation was not complete. We avoided these areas when capturing magnified images.

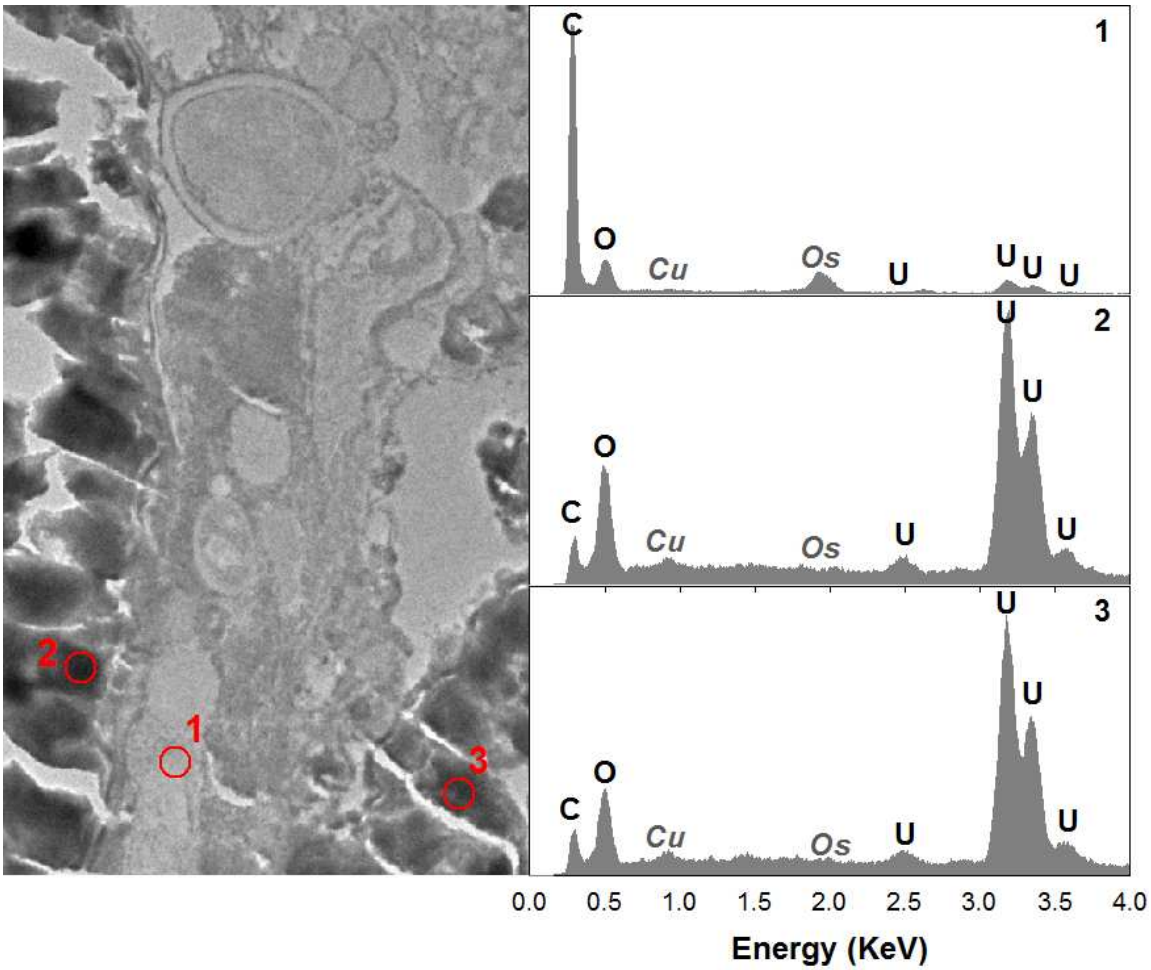


Fig 3.7 EDX spectra of different locations near the outside wall of the fiber, as indicated in the cropped TEM image of Fig 3.6B on left.

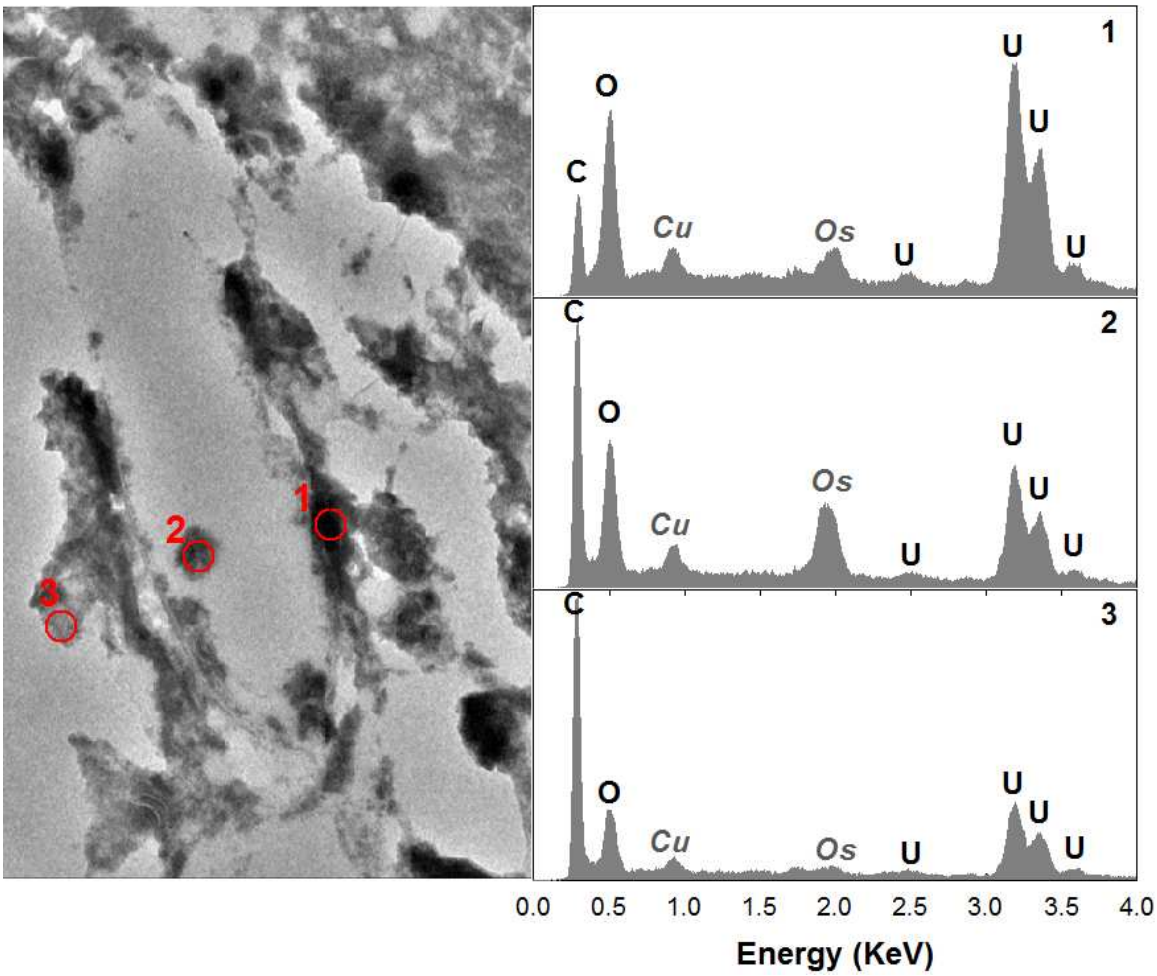


Fig 3.8 EDX spectra of different locations around a rod-shaped cell, as indicated in the cropped TEM image of Fig 3.6C on left.

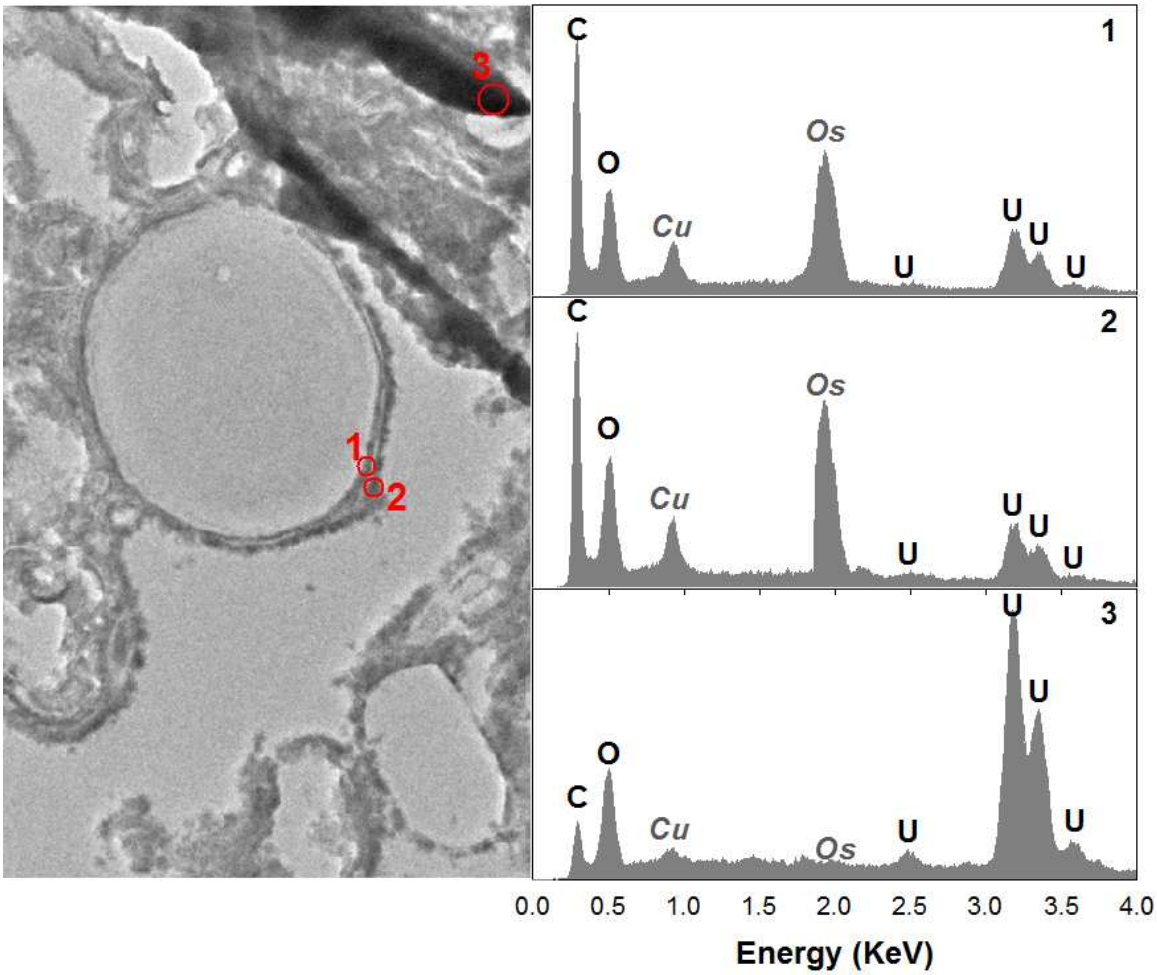


Fig 3.9 EDX spectra of different locations around the encrusted round spore, as indicated in the cropped TEM image of Fig 3.6E on left.

3.3.4. Microbial community structure of the biofilm

Figure 3.10 shows the taxonomic breakdown at the genus level for Stage 1 (U alone) and Stage 2 (U and sulfate). Perhaps surprisingly, the inoculated *D. vulgaris* almost disappeared (a negligible abundance of 0.2%) after the 26-day startup and 19-day continuous operation in Stage 1. Instead, members of the *Rhodocyclaceae* family and the *Veillonellaceae* family (*Thermosinus* spp.) became predominant in the biofilm community, with abundances of 69% and 14%, respectively.

The *Rhodocyclaceae* family belongs to *Rhodocyclales*, an order predominant in nitrate- and perchlorate-reducing MBfRs[332, 333]. Members in this family have been reported to be responsible for U(VI) bioreduction coupled with organic electron donors[149, 334, 335]. Thus, our results suggest, the first time, that *Rhodocyclaceae* family members grew lithotrophically by respiring U(VI) coupled with H_2 oxidation.

No previous research has reported that *Thermosinus* spp. has U(VI)-reducing capacity. However, the *Veillonellaceae* family belongs to the *Clostridiales* order, which is believed to play a role in breaking down biomass or other organic matter during *in situ* U(VI) bioreduction[336-338]. Thus, we interpret that *Thermosinus* spp. did not contribute directly to U(VI) reduction, but facilitated U(VI) reducers by degrading biomass and EPS through fermentation to acetate and H_2[339].

The major shift of the community during Stage 1 is similar to what Martins et al. observed in batch tests of U(VI) reduction[334]: a drastic change from SRB (including *D. vulgaris*) to *Clostridium* genus and *Rhodocyclaceae* families after U(VI) exposure. We interpret that *D. vulgaris* was not able to conserve energy and form a good biofilm in the H_2-based system with U(VI) reduction alone. This caused *D. vulgaris* to be outcompeted by *Rhodocyclaceae*

Regardless of the near absence of sulfate reduction in Stage 2, the microbial community underwent a drastic shift: the *Rhodocyclaceae* family decreased to 2%, *Thermosinus* spp. became negligible, and two other families in the *Clostridiales* order - *Clostridiaceae* and an unknown *Clostridiales* - became predominant, with abundances of 67% and 17%, respectively.

Clostridium is the only genus in the *Clostridiaceae* family known to be capable of U(VI) reduction: heterotrophically by vegetative cells or lithotrophically by spores[331, 340]. Vecchia et al.[331] proposed that redox reactions catalyzed by spores take place at the surface of the exosporium, where hydrogenases oxidize H_2, certain reductases reduce U(VI), and electrons are shuttled by carriers of various sizes. Thus, it is possible that spores can catalyze certain redox reactions even though they remain in their dormant state. The existence of spores is supported by the TEM images in Figures 3.6C and E.

The appearance of *Clostridiaceae* after SO_4^{2-} addition is similar to what was observed by Martins et al.[334] in their Cr(VI)-reducing tests: the presence of SO_4^{2-} and the lack of organic electron donor probably stimulated sporulation of *Clostridium* spp., which led to metal reduction in the exosporium. Perhaps the *Clostridiaceae* spores became predominant over the *Rhodocyclaceae* due their greater tolerance to alkaline conditions in long term[341].

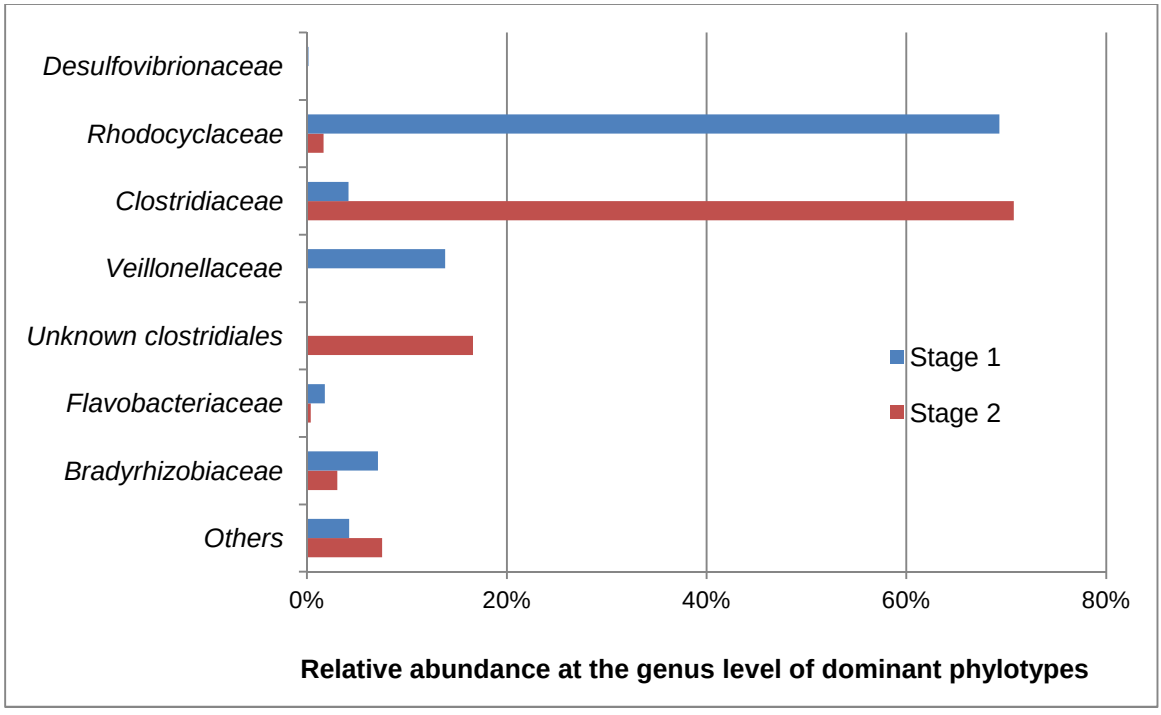


Fig 3.10 Relative abundances of the most abundant microbial phylotypes of the biofilm samples at the family level in Stage 1 and Stage 2. The sum does not add up to 100% in all cases because minor phylotypes are not shown.

3.4. Conclusion

Slow-growing U(VI) reducers formed biofilms on the fibers of the H_2-based MBfR after an extended startup. With an average U surface loading of 5.7 e^- mEq/m^2-day and an average SRT of 27 hours, the system successfully achieved and maintained 94-95% U(VI) removal at steady state with or without sulfate during over 8 months of operation, and the biofilm was capable of self-recovery after a disturbance due to O_2 exposure. Reduced U solids were clearly identified in the biofilm by XRD and TEM/EDX. Nanocrystalline UO_2 aggregates and amorphous U precipitates were associated with vegetative cells and mature spores that accumulated in the biofilm matrix. Sulfate was not reduced, and *D. vulgaris* and other SRB were not present in the biofilm; rather, the biofilm community mainly contained members of *Rhodocyclaceae* family and *Thermosinus* spp. when U(VI) was the only electron acceptor, and it underwent a dramatic shift to two other groups of the *Clostridiale* order when sulfate was added. The presence of the *Clostridiaceae* family supports the presence of spores that may have been responsible for U(VI) reduction in the biofilm in Stage 2.

CHAPTER 4. Biogenic iron-sulfide under various conditions

4.1. Introduction

The goal of this chapter is to present the experiments I conducted to investigate how different bacterial performances influenced the formation and crystallization of biogenic FeS solids under a variety of controllable environmental conditions. These completed experiments were the first part of a three-year collaborative project between Dr. Rittmann's team (including Dr. Rittmann, Dr. Vannela, and me) in Arizona State University (ASU) and Dr. Kim Hayes' team in University of Michigan (UofM). The ASU team was responsible to provide biogenic FeS and UO_2 with various characteristics, and the UofM team was responsible to conduct the subsequent UO_2 reoxidation experiments using the solids from the ASU team.

I prepared one manuscript based on these results. The title of the manuscript is "Effect of growth conditions on microbial activity and iron-sulfide production by *Desulfovibrio vulgaris*". The authors include Chen Zhou, Raveender Vannela, Kim F. Hayes, and Bruce E. Rittmann. The manuscript was published on *Journal of Hazardous Materials* 2014, 272: 28–35. The methods, results, and discussion in this chapter are the same as in the manuscript, but the introductory information was relocated to Chapter 1.

4.2. Experimental setup

4.2.1. Strain, growth medium, and culturing conditions

Desulfovibrio vulgaris subsp. *vulgaris* Postgate and Campbell (ATCC 29579) was purchased from the American Type Culture Collection (Rockville, Md.) and grown in 160-ml serum bottles with 100 ml medium and a headspace of N_2. The serum bottles were sealed with rubber stoppers and aluminum caps and mixed in a shaker (200 rpm) at 30℃. For providing biomass in the experiments, *D. vulgaris* was cultured in the standard ATCC 1249 medium, which contains 2 g/l $MgSO_4$, 5 g/l sodium citrate, 1 g/l $CaSO_4$, 1 g/l NH_4Cl, 0.5 g/l K_2HPO_4, 3.5 g/l sodium lactate, 1 g/l yeast extract, and 2 ml/l 5% ferrous ammonium sulfate (FAS) solution. The

pH of medium was adjusted to 7.5 before autoclaving and FAS addition. The medium contained 31.2 mM lactate, 19.4 mM citrate, 31.0 mM SO_4^{2-}, and 3.5 mM Fe(II). The cells were transferred to new serum bottles every four to seven days by injecting 2 to 3 ml inoculum into the new bottles containing freshly prepared media.

4.2.2. Medium modification

All medium modifications were based on stoichiometry. To perform experiments with different lactate-to-sulfate ratios, the original ATCC medium was modified by adding different concentrations of a sterile sodium lactate concentrate to achieve mole ratios of 0.5:1 (18.7 mM lactate, low sulfide production), 0.8:1 (28.5 mM lactate, moderate sulfide production), or 1.9:1 (69.3 mM lactate, nearly complete sulfide production). In experiments with different iron-to-sulfate mole ratios, additional iron was added from a deoxygenated 2.20 M $FeCl_2$ concentrate (pH < 2) that had been filter-sterilized. Four different iron-to-sulfate mole ratios were used: 0.11:1 (without extra iron addition; the only iron source was FAS in the original medium; 0.2:1 iron-to-sulfide, Fe very limiting), 0.25:1 (0.5:1 iron-to-sulfide, Fe limiting), 0.5:1 (1.1:1 iron-to-sulfide, approximately stoichiometric Fe and S), and 0.9:1 (1.9:1 iron-to-sulfide, Fe overdosed). In the pH-impact experiments, HCl or NaOH was used to adjust the pH of the original ATCC medium to one of five levels (5.5, 6.5, 7.5, 8.5, or 9.5, all within a range allowing for general bacterial growth) before autoclaving. After autoclaving, FAS addition, and inoculation, the pH values were measured and found to be 5.6, 6.5, 6.9, 7.3, and 8.6, respectively.

One set of electron-donor experiments replaced lactate with pyruvate at the same mole concentration (31.2 mM). For an electron-donor experiment involving H_2, 20 mM acetate was added first, the medium was then purged with CO_2 gas, the pH was adjusted to 7.2 by addition of sodium bicarbonate, and H_2 gas was injected directly into bottles after inoculation with *D. vulgaris*.

Table 4.1 summarizes the nomenclature and conditions for all experiments, along with key results described in the Results and Discussion section (2.2).

Table 4.1 Initial concentrations of lactate, sulfate and Fe^{2+}, initial and final pHs, experimental durations, estimated concentrations of final FeS solids and free sulfide, particle thicknesses of biogenic mackinawite, presence/absence of greigite and vivianite under all growth conditions.

Experiment Designation		Initial [lactate] (mM)	Initial [sulfate] (mM)	Initial [Fe^{2+}] (mM)	Initial pH (s.u.)	Final pH (s.u.)	Duration* (day)	Final FeS† (mM)	Final Free Sulfide‡ (mM)	Mackinawite thickness (nm)	Greigite	Vivianite
[lactate] : [sulfate]	0.5:1	18.7	36.1	3.4	6.6	6.8	5	3.4	4.9	4.2	-	-
	0.8:1	28.5	35.3	3.3	6.6	6.9	5	3.3	9.5	9.3	-	-
	1.9:1	69.3	36.6	3.3	6.7	7.0	5	3.3	29.3	18.5	+	-
[iron] : [sulfate]	0.11:1	34.1	32.2	3.1	7.0	6.9	4	3.5	14.4	2.2	-	-
	0.25:1	33.0	33.7	7.6	6.8	6.9	4	7.8	10.3	3.3	-	-
	0.5:1	32.5	33.5	15.5	6.5	6.5	4	15.2	2.1	12.6	-	-
	0.9:1	29.3	33.0	31.1	6.2	6.3	4	20.1	0	2.2	-	+
pH	5.6	33.4	31.6	2.9	5.6	6.7	16	3.7	13.5	-§	-	-
	6.5	32.9	33.3	3.5	6.5	6.9	8	3.5	9.9	23.2	-	-
	6.9	29.9	35.2	3.6	6.9	6.9	8	3.9	10.2	23.8	-	-
	7.3	32.8	35.7	3.1	7.3	7.0	8	3.2	10.9	12.2	-	-
	8.6	34.4	36.9	3.2	8.6	7.4	16	3.2	13.0	4.4	-	-
Other *e*- donor	Pyruvate	30.0	37.3	3.2	6.7	6.4	4	3.4	3.9	15.1	-	-
	H_2	-	38.8	3.5	7.2	7.6	3	3.7	6.0	3.7	-	-

* Counted from the day when the bottles were inoculated to the day when the bottles were opened for solid collection.
† Assuming that the precipitated iron was completely converted to FeS (except when vivianite was formed).
‡ Assuming that the reduced sulfate was completely converted to sulfide.
§ Unable to measure because no solids were collected from the bottle.

4.2.3. Analytical methods

Routine analyses of liquid samples were carried out daily or every second day. 3-ml liquid samples were collected in an anaerobic glove box using a sterile syringe and stored in 15-ml centrifuge tubes for pH measurement with an Epoxy Semi-Micro Combination pH Electrode (Beckman Coulter BKA57187) and a pH Meter (Beckman Coulter BKA58734). The samples were then centrifuged at 200 g for 6 minutes to remove the Fe-S solids, but not biomass, which had a lower density. The centrate was analyzed with a UV–Visible spectrophotometer (Cary 50 Bio, Varian, Inc., Santa Clara, CA) at 600-nm wavelength for optical density (OD), protein concentration with Coomassie (Bradford) reagents, and soluble iron (III) plus total soluble iron by the colorimetric 5-sulfosalicylic acid (SSA) method[299]. The standard deviations of the measurements for protein, iron (III), and total iron concentrations were 0.04 mg/l, 0.20, and 0.31 mM, respectively (n = 3 samples).

Samples diluted 200-fold after filtration were used for analyses of concentrations of anions (including sulfate, chloride, nitrate, and phosphate) by ion-exchange chromatography (IC, Dionex ICS2000) and for concentrations of volatile fatty acids (acetic acid, lactic acid, citric acid, pyruvic acid, formic acid, and butyric acid) by high-performance liquid chromatography (HPLC, Shimadzu 20AT) with a refractive index detector (RID). The standard deviations of the measurements for sulfate, lactate, acetate, and pyruvate concentrations were 0.02, 0.01, 0.04, and 0.00 mM, respectively (n = 3 samples). H_2 was measured using a gas chromatograph (GC 2010, Shimadzu) equipped with a thermal conductivity detector and a packed column (ShinCarbon ST 100/120 mesh, Restek Corporation) for separating sample gases. The standard deviation of the measurement for hydrogen concentrations was 0.06 atm (n = 6 samples).

4.2.4. Separation of iron sulfide solids from culture medium

After complete lactate consumption was achieved, the serum bottles were placed in an anaerobic glove box and left there overnight, during which time most of the solids settled to the bottom. Without re-suspending the settled solids, bottles were opened (while still in the anaerobic glove box), and the supernatant was removed with a pipette. The solids and residual liquid (~ 10

mL) were transferred to 50-ml centrifuge tubes. About 40 ml anoxic sterile deionized water was used in order to rinse out any solids adhering to the walls inside the bottles and then transferred into the centrifuge tubes. The tubes were then capped, vortexed, and centrifuged at 1,800 g for 6 minutes. The supernatant was removed with a pipette, and the rinsing steps were repeated two more times. The tubes were then placed in an air-tight glass container, taken out of the glove box, and attached to a freeze dryer (Labconco FreeZone) for freeze drying at -50℃ under 10 Pa vacuum for 2 days. The dried solids were weighed, ground by the mortar and pestle in anaerobic chamber, and stored in 10-ml serum bottles sealed with rubber stoppers for further analysis on X-ray diffraction (XRD).

4.2.5. X-Ray Diffraction (XRD) analysis

XRD was performed using a Rigaku D/Max-IIB diffractometer with monochromated Cu *K*α radiation. The powdered solids were packed into glass slides and immobilized by a steamed mixture of white petroleum jelly and n-hexane. The X-ray scanning featured a constant scanning speed of 0.75 deg/min from 5° to 90° 2 Θ and a step interval of 0.02° 2 Θ. XRD patterns were processed using the computer programs Jade (Materials Data, Inc., Livermore, CA) and Microsoft Excel (Microsoft Corp., Redmond, WA). The average particle sizes of the mackinawite in those samples were estimated by Jade on the basis of the Scherrer equation:

$$t = \frac{0.9\lambda}{B\cos\theta_B} \qquad (2.1)$$

where t = thickness of the particles (Å), λ = wavelength of the incident X-ray (Å), B = full width at half maximum (FWHM) of the (0 0 1) peak (radian) based on instrumental correction using LaB6 standard powder, and θ_B is the Bragg angle (degrees) at the (0 0 1) peak[300-302].

4.2.6. Stoichiometry equations for mass balance calculation

Mass balances on S and Fe were developed on the basis of Eqns. 4.12 – 4.16 and by assuming that sulfate was reduced completely to sulfide and that iron precipitated with S was FeS. This leads to the following mass balances on total sulfur (eqn. 4.2), sulfide-S (eqn. 4.3), and Fe^{2+} (eqn. 4.4):

$$C_{\mathrm{S,\,total}} = \left[\mathrm{SO_4^{2-}}\right]_{\mathrm{initial}} = \left[\mathrm{SO_4^{2-}}\right]_{\mathrm{final}} + C_{\mathrm{S^{2-},\,total}} + C_{\mathrm{S^0}} \qquad (4.2)$$

$$C_{\mathrm{S^{2-},\,total}} = C_{\mathrm{S^{2-},\,free}} + C_{\mathrm{FeS}} \qquad (4.3)$$

$$C_{\mathrm{Fe,\,total}} = \left[\mathrm{Fe^{2+}}\right]_{\mathrm{initial}} = C_{\mathrm{FeS}} + \left[\mathrm{Fe^{2+}}\right]_{\mathrm{finial}} \qquad (4.4)$$

4.3. Results for Bacteria growth and solid formation

4.3.1. Various lactate-to-sulfate mole ratios

Figure 4.1 presents the results for the experiments with different lactate-to-sulfate mole ratios. Complete lactate fermentation took approximately 2, 3, and 5 days for lactate-to-sulfate mole ratios of 0.5:1, 0.8:1, and 1.9:1, respectively (Fig 4.1A). As expected, higher lactate concentration produced more H_2 through fermentation, resulting in more SO_4^{2-} reduction (Fig 4.1B) and corresponding Fe^{2+} loss (Fig 4.1D), protein (Fig 4.1F), and acetate accumulation (Fig 4.1C), along with a slightly higher pH (Fig 4.1E). However, the specific growth rates of *D. vulgaris* for lactate-to-sulfate mole ratios of 0.5:1, 0.8:1, and 1.9:1 were similar: 0.35, 0.30 and 0.36 h^{-1}, respectively. These similar values reveal that higher lactate concentration did not enhance the bacteria's growth, suggesting that the half-maximum rate concentration (K_s) of lactate was small for *D. vulgaris*. For example, Zellner et al. estimated K_s of 1.5 mM, a value much smaller than the smallest starting concentration (18.7 mM for the 0.5:1 bottle)[342].

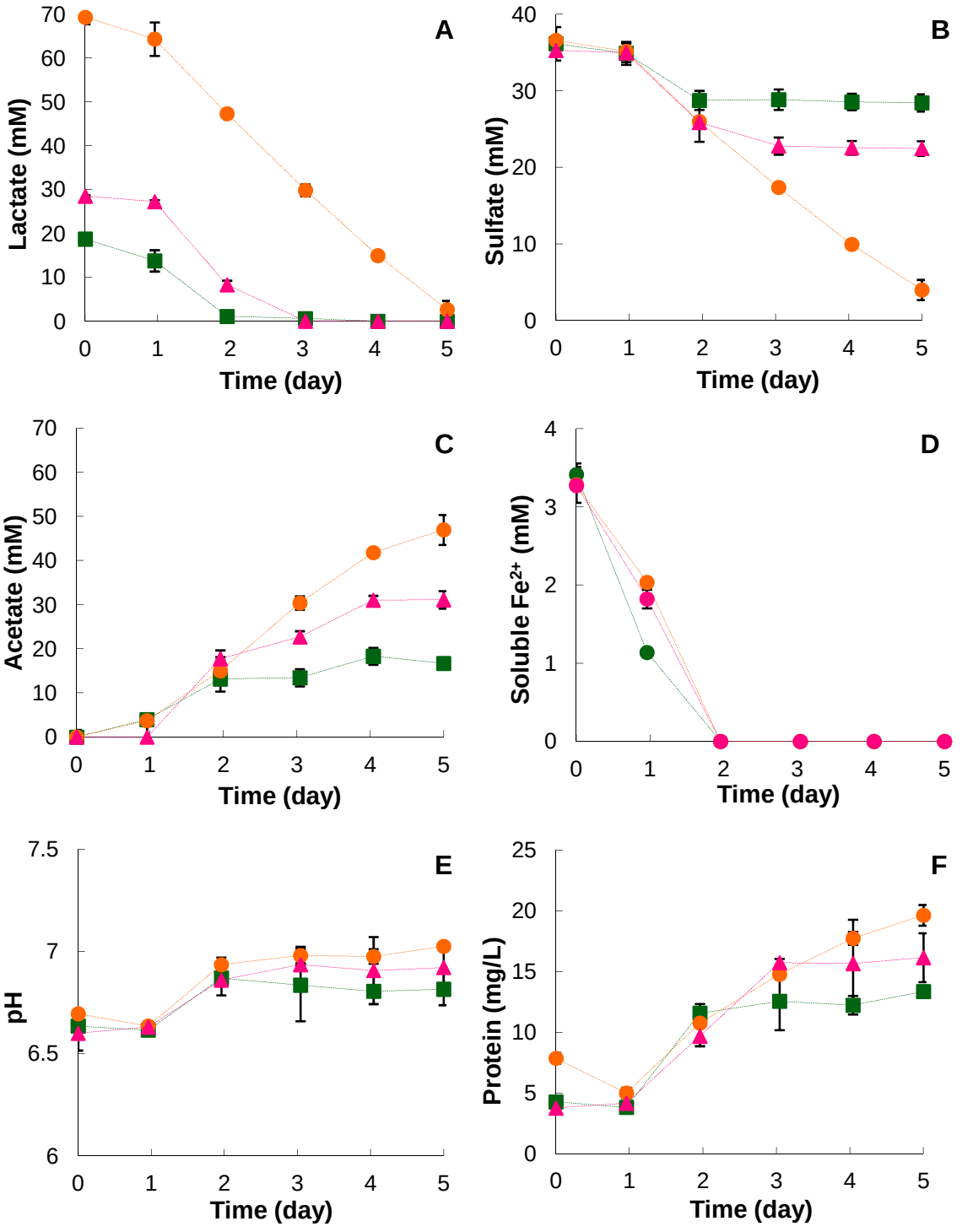


Fig 4.1 Concentrations of lactate (A), sulfate (B), acetate (C), soluble Fe^{2+} (D), pH (E), and protein (F) during the growth of *D. vulgaris* with initial lactate-to-sulfate mole ratios of 0.5:1 (●), 0.8:1 (▲), and 1.9:1 (■).

Black precipitate started to appear within one day and increased over the duration of the experiments. The FWHM and the average particle size values are summarized in Table 4.1. The calculated concentrations of FeS and free sulfide (based on eqns. 4.2 – 4.4) are also summarized in Table 4.1. The XRD analyses show that solid samples collected from the bottles with the initial lactate-to-sulfate mole ratios of 0.5:1, 0.8:1, and 1.9:1 had the characteristic peaks of mackinawite (Figs. 4.2A and 4.2B) and particle thicknesses of 3.8, 7.9, and 14.2 nm, respectively (Table 4.1). The solids from the bottle with the mole ratio of 1.9:1 also showed the presence of greigite (Fig. 4.2C), which is thought to be formed from mackinawite very slowly[212, 219, 221]. Abiotic greigite formation from mackinawite in laboratory experiments may have been the result of accidental oxygen exposure during solid phase characterization[217], an explanation not relevant for our experiments, in which care was taken to protect against oxygen exposure. More likely is that higher sulfide accumulation (29.3 mM free sulfide; Table 4.1) resulting from the higher concentration of lactate (69.3 mM initially) accelerated the crystallization process of mackinawite to greigite. The transformation of mackinawite towards greigite is thought to proceed via the reaction of FeS with aqueous H_2S or polysulfides[224, 343]. Herbert et al. used high lactate and sulfate concentrations, but quite low iron concentrations in the SRB medium, and this also led to free-sulfide as high as 11 mM[224]. They observed biogenic precipitates similar to greigite, with the remaining mineral mass composed of disordered mackinawite. Gramp et al. also observed the presence of biogenic greigite and mackinawite in mixed cultures of SRB with iron-to-sulfide mole ratios from 1:3.25 to 1:20 (where the estimated concentrations of free sulfide were higher than 4.0 mM) at 45℃, but they saw only biogenic mackinawite with any iron-to-sulfide mole ratios at 22℃ [344]. In our experiments, which were carried out at moderate temperature (30℃), greigite was still absent when the final free sulfide was 9.5 mM (initial lactate-to-sulfate mole ratios of 0.8:1; Table 4.1). This trend further indicates that free sulfide concentration and temperature can promote crystallite growth, including the formation of greigite; in addition, more free sulfide was needed to induce greigite formation at lower temperature.

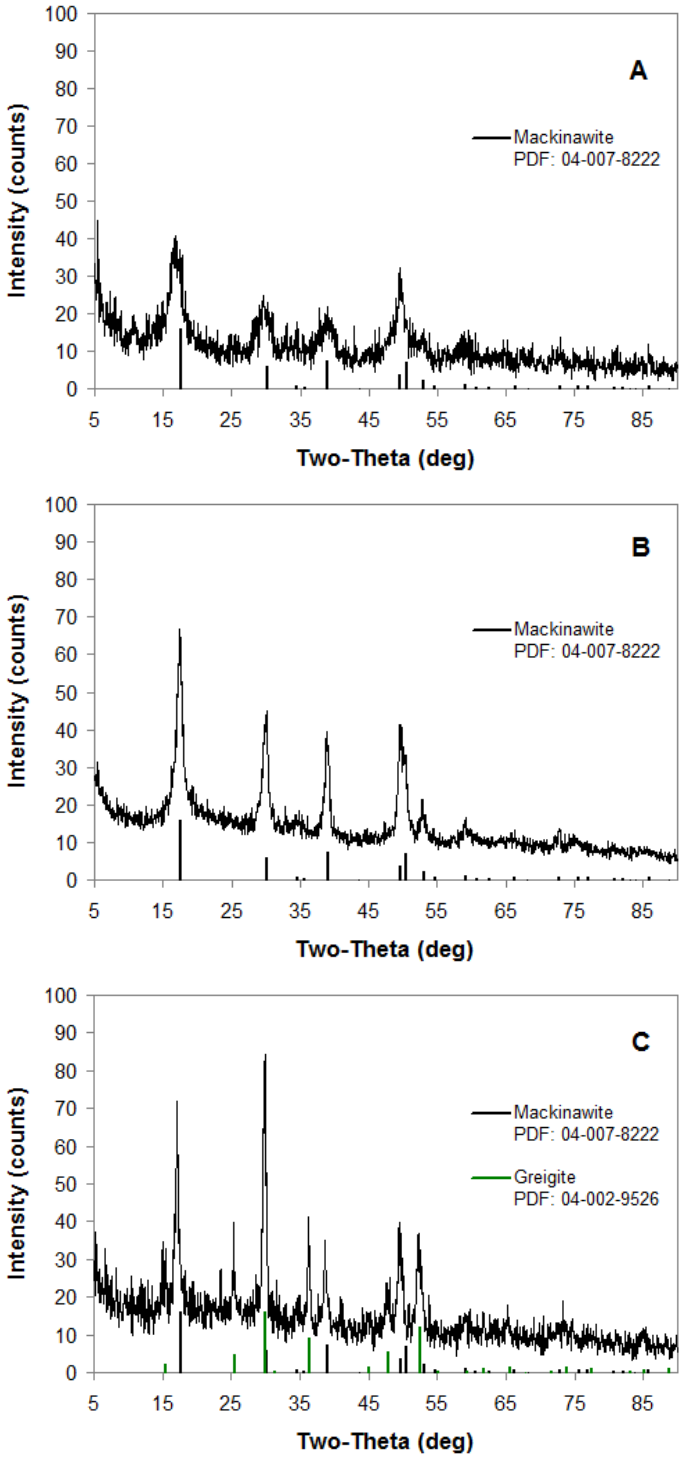


Fig 4.2 XRD patterns of solids separated from the *D. vulgaris* cultures with lactate-to-sulfate mole ratios of 0.5:1 (A), 0.8:1 (B), and 1.9:1 (C).

4.3.2. Various iron-to-sulfate mole ratios

For all four iron-to-sulfate mole ratios (i.e., 0.1:1, 0.25:1, 0.5:1, and 0.9:1), lactate was completely fermented within three days (Fig 4.3A); sulfate reduction (Fig 4.3B) and loss of aqueous iron occurred in parallel during the three days and were consistent the 1:1 FeS mole ratio for formation of mackinawite. More iron led to lower initial and final pH values, as shown in Table 4.1, but initial pH as low as 6.1 did not inhibit bacterial growth.

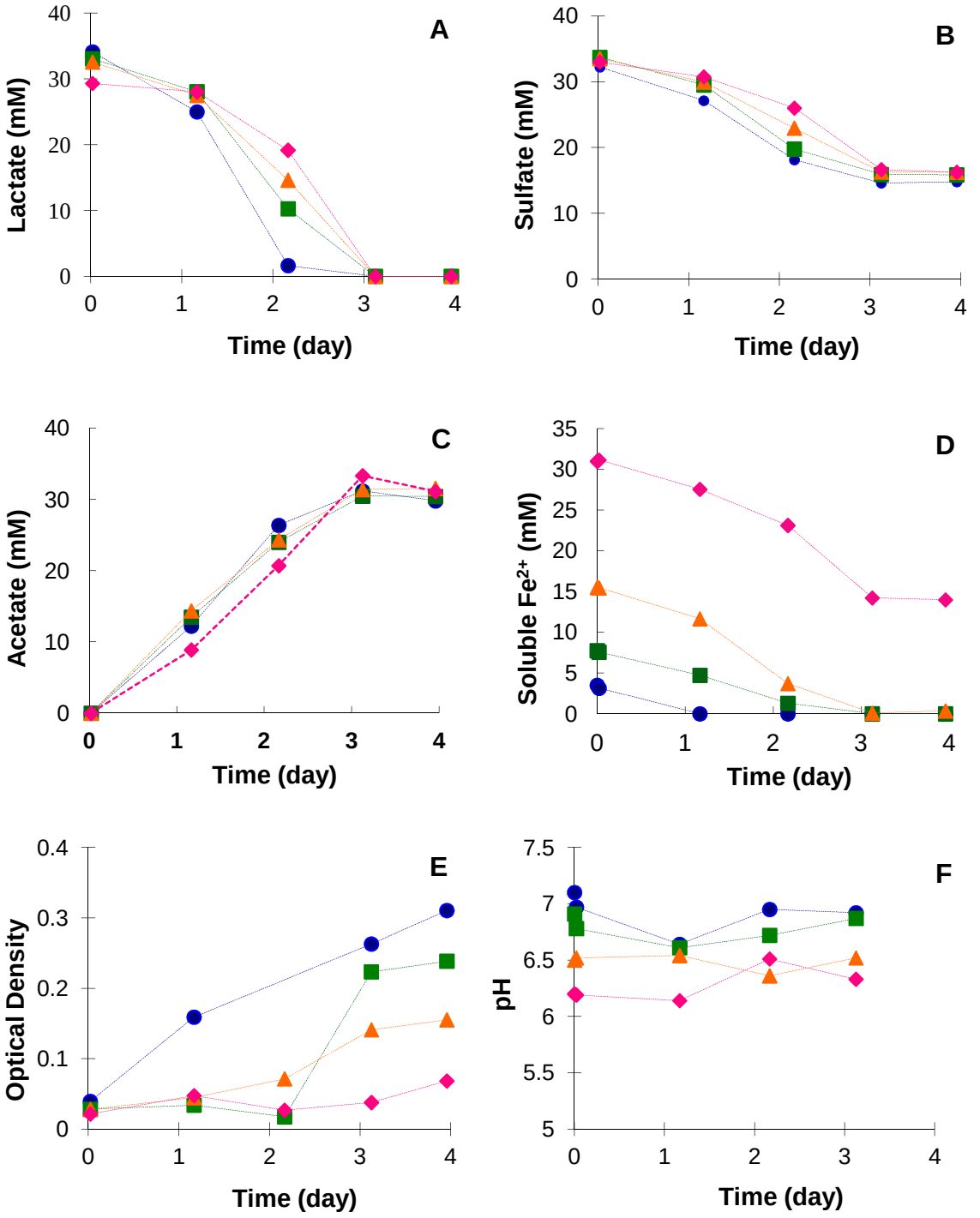


Fig 4.3 Concentrations of lactate (A), sulfate (B), acetate (C), soluble Fe^{2+} (D), optical density (E), and pH (F) during the growth of *D. vulgaris* with initial iron-to-sulfate mole ratios of 0.11:1 (●), 0.25:1 (■), 0.5:1 (▲), and 0.9:1 (◆).

As shown in the XRD spectra of Figure 4.4, mackinawite was present in all solid samples generated from the various [Fe]:[S] ratios. However, the solid sample from the medium with the lowest iron-to-sulfate mole ratio (0.11:1) had the widest peaks with the lowest intensities (Fig 4.4A), as well as the smallest crystallite size (2.1 nm of the particle thickness, Table 4.1); the samples with the iron-to-sulfate mole ratios of 0.25:1 and 0.5:1 showed sharper peaks with higher intensities (Figs 4.4B and 4.4C) and larger crystallite sizes (Table 4.1). Thus, high iron concentration enhanced the process of crystallite growth of mackinawite, probably by accelerating the rate of FeS formation. That greigite was absent in all four samples supports that free sulfide as high as 14.4 mM (the lowest initial iron-to-sulfate mole ratio of 0.11:1; Table 4.1) was not sufficient by itself to induce greigite formation for our lactate-to-sulfate experiments at 30℃ (Fig 4.1), as well as for Gramp et al [344].

Vivianite [$Fe_3(PO_4)_2{\cdot}8(H_2O)$] was detected only in the medium when iron was applied at the highest iron-to-sulfate mole ratio (0.9:1; Fig 4.4D). Vivianite is thought to be produced rapidly at circumneutral pH when aqueous phosphate ions and certain iron-containing compounds are present (Hansen and Poulsen, 1999; Zegeye *et al.*, 2007). Although the same initial phosphate concentration (2.9 mM) was present in all experiments, vivianite was not formed in experiments with lower initial iron-to-sulfate ratios (i.e., iron was precipitated only as FeS) because: 1) Fe(II)-citrate complexes (with 1 Fe^{2+} and 2 citrate anions each) kept aqueous Fe(II) from reaching super-saturation with precipitates other than mackinawite (when sulfide was present in sufficient quantities)[302]; and 2) a certain amount of free sulfide suppresses vivianite formation by competing with PO_4^{3-} for soluble Fe^{2+} [345]. In our experiments, lower initial iron-to-sulfate ratios allowed all iron to be converted to FeS with free sulfide remaining (from 2.1 mM to 14.4 mM, shown in Table 1). However, the highest initial iron-to-sulfate mole ratio (0.9:1) left a considerable amount of dissolved Fe(II) (up to 14.0 mM) in excess of the Fe(II)-citrate ligand (ca. 9.7 mM) after FeS precipitation. In addition, the smaller crystallite size (2.1 nm) for mackinawite, similar to the small size observed for the iron-to-sulfate mole ratio of 0.11:1 (Table 4.1), indicates that the formation of vivianite may have retarded the formation of FeS precipitation by competing for iron and effectively lowering the iron-to-sulfate ratio.

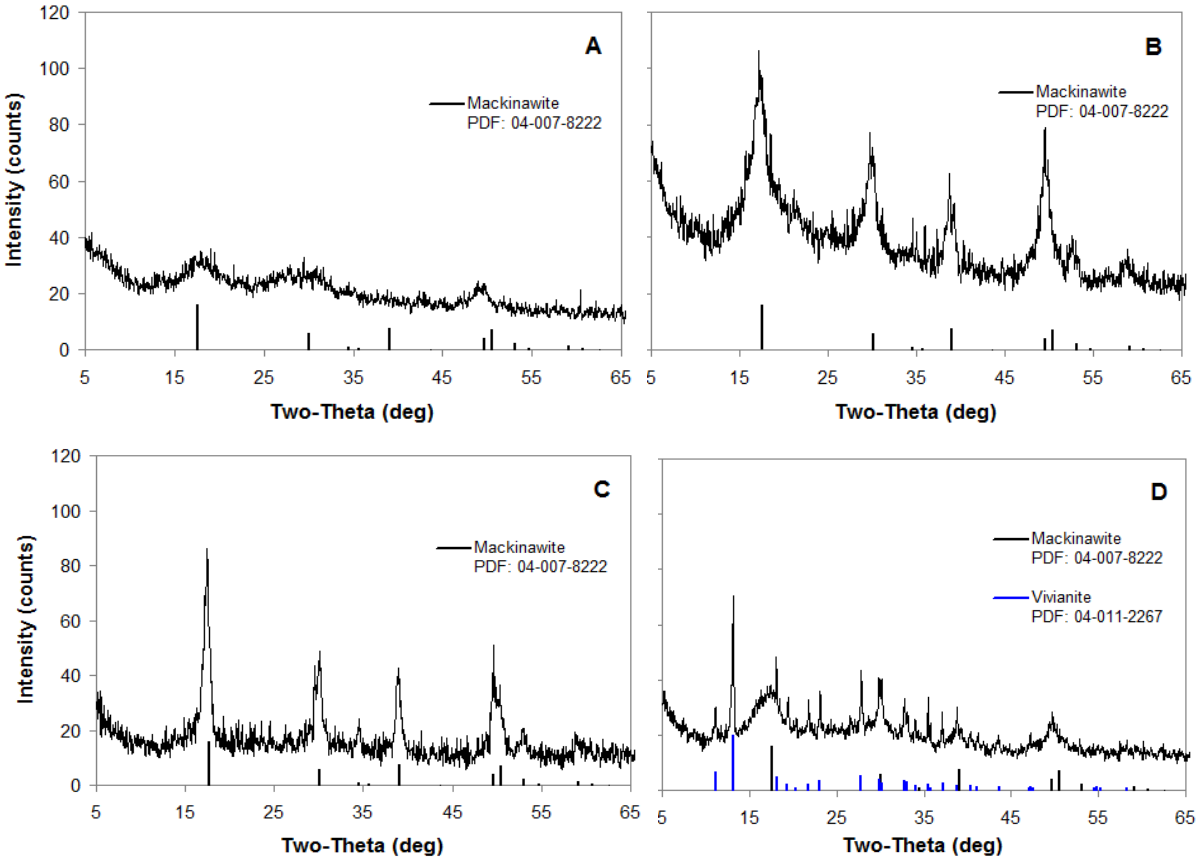


Fig 4.4 XRD patterns of solids separated from the *D. vulgaris* cultures with iron-to-sulfate mole ratios of 0.1:1 (A), 0.25:1 (B), 0.5:1 (C), and 0.9:1 (D).

4.3.3. Various pHs

As shown in Figure 4.5, *D. vulgaris* with initial pH of 6.9 started to grow from the third day, but *D. vulgaris* with initial pH values of 7.3 and 6.5 started one day and two days later, respectively. For these three pH conditions, *D. vulgaris* completed lactate fermentation and SO_4^{2-} reduction within three days from the onset of growth. The specific growth rate of *D. vulgaris* with initial pH value of 7.3 was 0.044 h^{-1}, slightly higher than those of *D. vulgaris* with initial pH values of 6.5 and 6.9 (0.030 h^{-1} and 0.032 h^{-1}, respectively). Although *D. vulgaris* with initial pH values of 5.6 and 8.6 showed no growth after 8 days, complete lactate oxidation and SO_4^{2-} reduction occurred on the 16th day (data not shown). Retarded growth at pH values of 5.6 and 8.9 indicates that circumneutral pH (6.5 – 7.3) is favorable for *D. vulgaris*, but they can adapt to the weak acidic (pH 5.6) or weak basic (pH 8.6) conditions when provided longer acclimation periods.

The pH changes in the incubations, summarized in Table 4.1, show that the pH moved towards neutral in all cases. SO_4^{2-} reduction caused a pH increase by producing excess sulfide, a strong base, for the low-pH incubation. On the other hand, the greater precipitation of FeS solids lowered the pH in the high-pH incubations by consuming base (S^{2-}). Meanwhile, lactate fermentation in all cases produced a large amount of carbonate (eqns. 1.12 and 1.13), which buffers the pH near neutral.

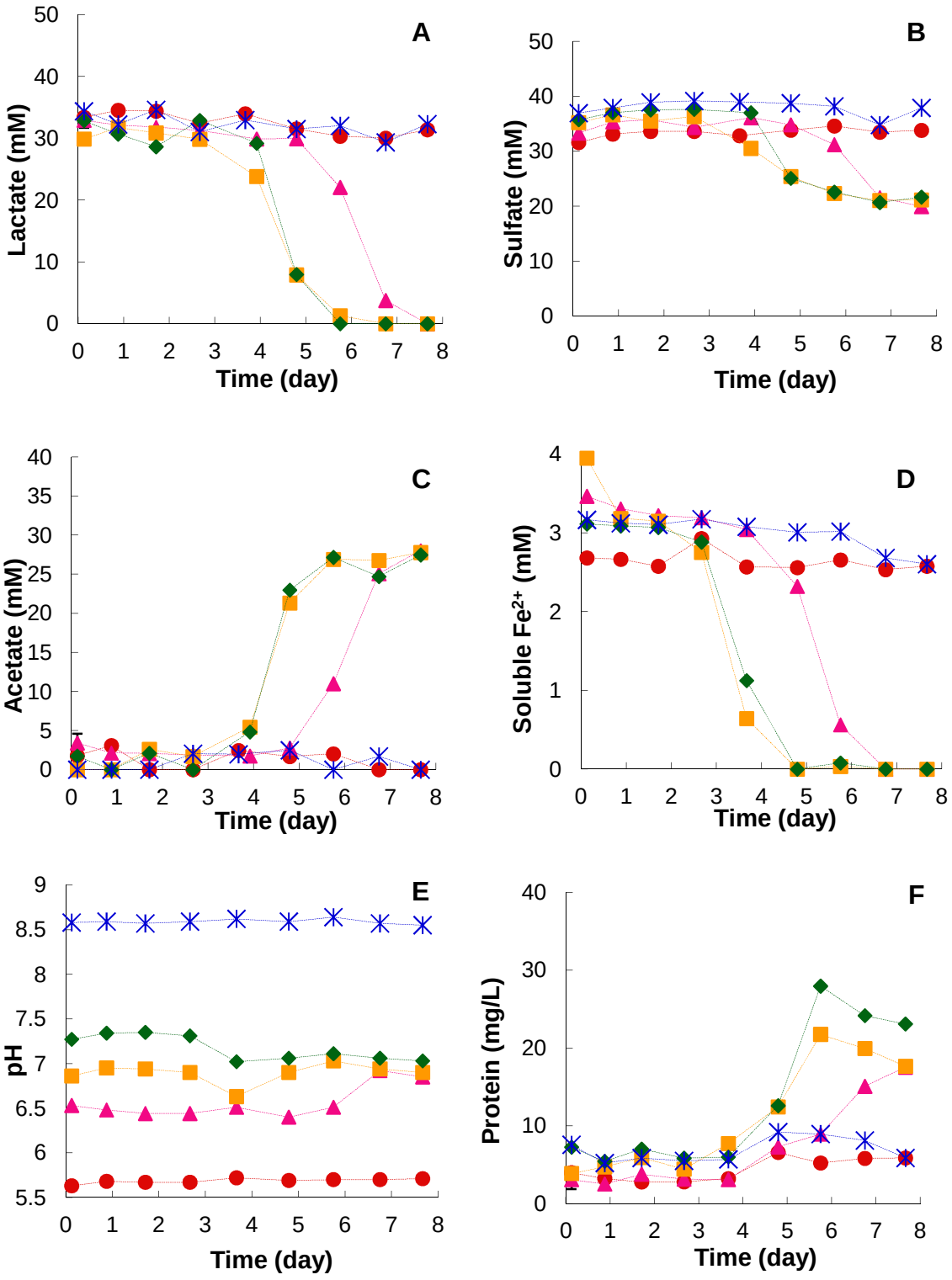


Fig 4.5 Concentrations of lactate (A), sulfate (B), acetate (C), soluble Fe^{2+} (D), pH (E), and protein (F) during the growth of *D. vulgaris* with initial pHs of 5.6 (●), 6.5 (▲), 6.9 (■), 7.3 (◆) and 8.6 (*) within 8 days.

Figure 4.6 show the XRD patterns of the solid samples for the four highest pH conditions. An XRD pattern of the solid sample separated from the bottle with initial pH 5.6 is not available because the quantity of solids was too little (lower efficiency in production) for analysis. Mackinawite was detected in all samples, but, in general, higher initial pH led to smaller crystallite size (Table 4.1). The considerable range of particle size (4 -17 nm, Table 4.1) produced within the relatively narrow range of pH suggests that the rate of mackinawite crystal growth was quite sensitive to pH, a trend also reported by Wang and Morse[223] in a chemogenic system.

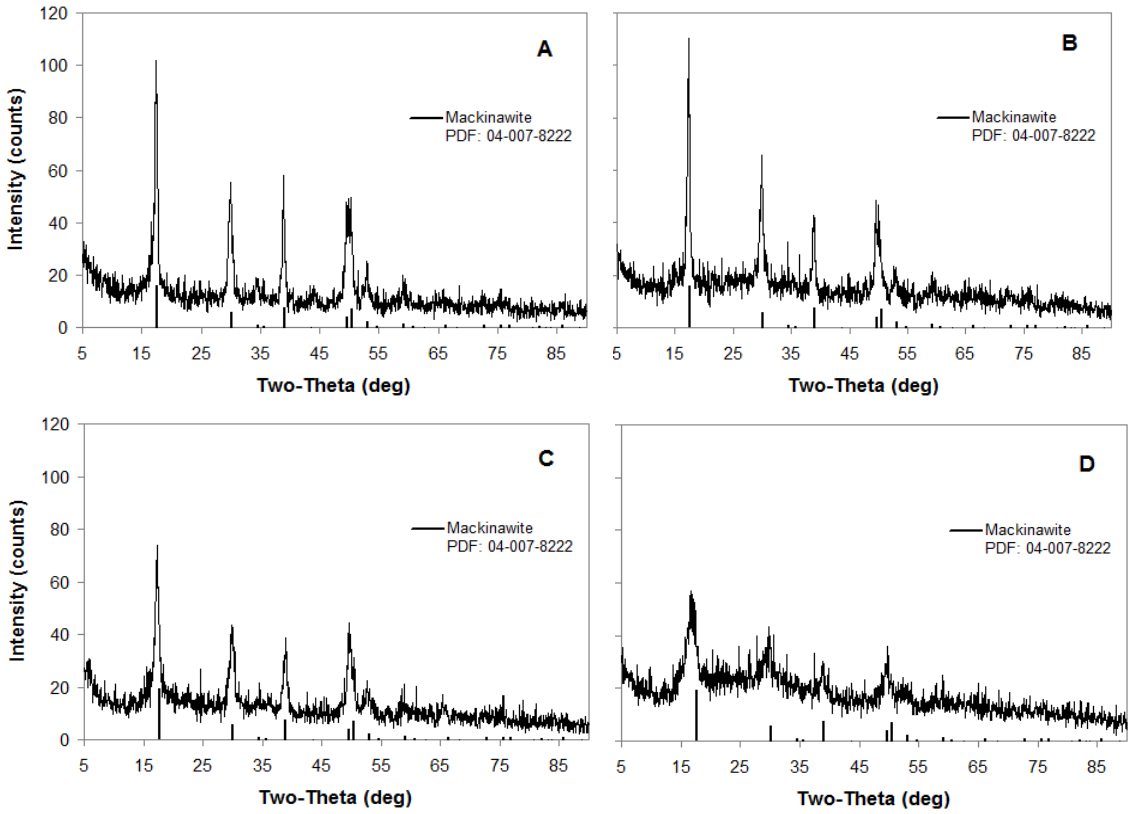


Fig 4.6 XRD patterns of solids separated from the *D. vulgaris* cultures with initial pHs of 6.5 (A), 6.9 (B), 7.3 (C), and 8.6 (D).

4.3.4. Various electron donor candidates

Pyruvate. All pyruvate was fermented to acetate within only about two days, as shown in Figure 4.7A. Since pyruvate is the first intermediate during lactate fermentation to acetate and H_2[274, 275], the faster utilization rate of pyruvate compared to lactate leads to the hypothesis that lactate fermentation to pyruvate is the limiting step during the entire process of lactate fermentation.

According to stoichiometry (Eqns 1.13 and 1.16), one mole of pyruvate reduces approximately 0.25 mole SO_4^{2-}, which is only half of the SO_4^{2-} reduced (0.5 mole) by one mole of lactate (Eqns 1.12, 1.13 and 1.16), since the sole pyruvate fermentation generates less H_2. This stoichiometric calculation is consistent with the experiment results that 7.3 mM SO_4^{2-} was reduced when 30 mM pyruvate was present, while 14.5 mM SO_4^{2-} was reduced when 30 mM lactate was present. Furthermore, sulfate reduction coupled with lactate fermentation did not consume protons (Eqns. 1.12, 1.13 and 1.16), while SO_4^{2-} reduction coupled with pyruvate fermentation led to considerable proton production (0.4 mole H^+/mole pyruvate; Eqns 1.13 and 1.16). That difference accounts for the pH decrease from 6.7 to 6.3 in the experiment with pyruvate. Finally, the XRD spectrum in Figure 4.7B shows characteristics of highly crystalline mackinawite (12.9 nm, Table 4.1) with pyruvate as the electron donor, and this is consistent with the production of the relatively larger crystallite size at lower pH (16.6 nm for solids collected with lactate as electron donor, initial pH 6.5, and final pH 6.9, Table 4.1).

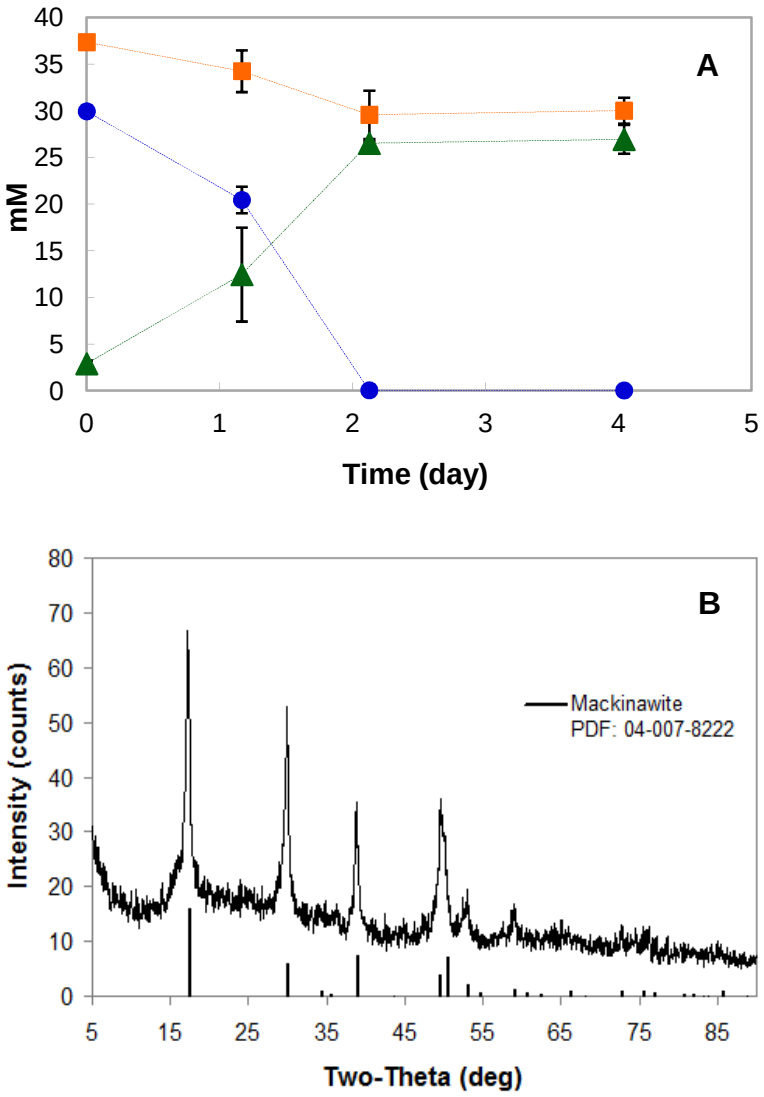


Fig 4.7 (A) Pyruvate (●), sulfate (■), and acetate (▲) in the culture of *D. vulgaris* growing exclusively on pyruvate; (B) XRD spectra of solids produced by *D. vulgaris* growing exclusively on pyruvate.

Hydrogen gas. Without any signs of growth retardation, bacteria utilized H_2 while reducing sulfate, as shown in Figure 4.8A. Within less than 2 days, around 25% of the sulfate had been reduced. In contrast to weakly basic conditions with lactate as the electron donor, the pH with H_2 increased to over 7.5 in parallel with H_2 oxidation and SO_4^{2-} reduction. This is consistent with proton consumption when sulfate reduction is coupled to H_2 oxidation and autotrophic cell synthesis using acetate as the C source[273].

The XRD spectrum in Figure 4.8B shows characteristics of a more poorly crystallized and smaller crystallite size of mackinawite (3.5 nm, Table 4.1) with H_2 as the electron donor at the higher pH of 7.5. The size is very close to the particle thickness of the solids collected with lactate as electron donor, initial pH 8.6, and final pH 7.5 (4.0 nm, Table 4.1).

The XRD results for pyruvate and H_2 underscore that the crystallization process was affected more by the final pH after FeS had been precipitated than by the electron donor, as the iron concentrations were identical (3.5 mM) and the sulfide concentrations were close (3.9 mM and 6.0 mM; Table 4.1). As expected, greigite was absent, because both electron donors were limiting (only 22% and 25% sulfate was reduced), resulting in 3.9 mM and 6.0 mM free sulfide remaining, respectively. These were significantly lower than the sulfide concentration of the condition of 1.9:1 lactate-to-sulfate mole ratio where greigite was observed (29.3 mM).

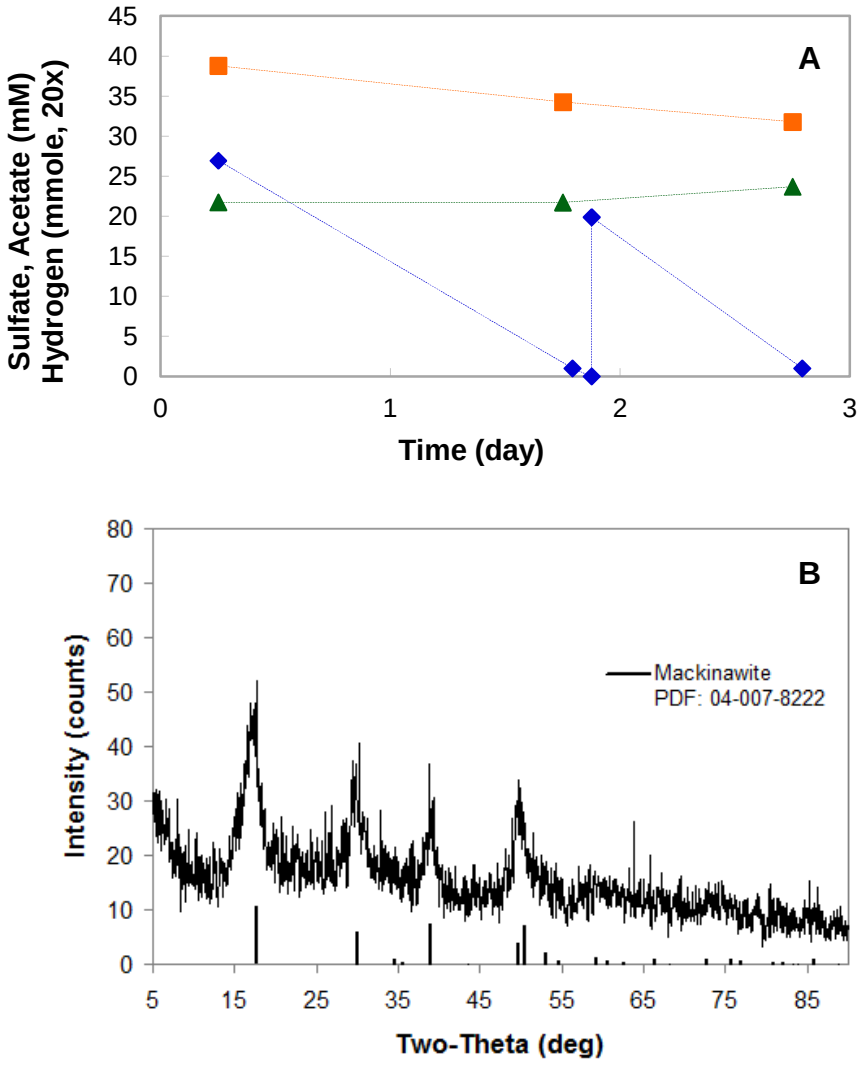


Fig 4.8 (A) H_2 (●), sulfate (■), and acetate (▲) in the culture of *D. vulgaris* growing exclusively on hydrogen gas; (B) XRD spectra of solids produced by *D. vulgaris* growing exclusively on hydrogen gas.

4.4. Summary

By fermenting lactate, *D. vulgaris* produced H_2 to provide electrons for SO_4^{2-} reduction to sulfide, which led to the formation of crystalline mackinawite when Fe^{2+} was present. As long as the lactate concentration was well above the half-maximum-rate concentration, high lactate-to-sulfate ratios did not affect the kinetics of bacterial growth, but they strongly enhanced the FeS crystallization by reducing more sulfate to sulfide. In particular, the highest lactate-sulfate mole ratio (1.9:1) led to the presence of greigite, which normally forms slowly. Varying the iron-to-sulfate ratio showed that an initial soluble Fe^{2+} concentration as high as 30 mM did not inhibit bacterial growth, but having soluble Fe^{2+} remain after precipitation with sulfide resulted in formation of vivianite. Although *D. vulgaris* grew faster at near-neutral pH (6.5 – 7.3), it adapted to weakly acidic or weakly basic conditions (pH values of 5.7 or 8.6), and lower pH led to more crystalline mackinawite. Besides lactate, *D. vulgaris* could grow successfully with pyruvate or hydrogen gas as the sole electron donor, and it produced mackinawite in both cases; as with lactate, lower pH enhanced crystallization.

CHAPTER 5. Biogenic iron-sulfide from various iron sources

5.1. Introduction

The goal of this chapter is to present the experiments I conducted to investigate formation and crystallization of biogenic FeS solids from different iron sources when electron donor was lactate or pyruvate. These completed experiments were the second part of the three-year collaborative project between ASU team and UofM team.

I prepared one manuscript based on these results. The title is "The electron donor determines distinct patterns of sulfate and Fe(III)-(hydr)oxide reductions and concomitant iron sulfide formation by *Desulfovibrio vulgaris*". The authors include Chen Zhou, Raveender Vannela, Kim F. Hayes, and Bruce E. Rittmann. The manuscript has been submitted to *Water Research* and is now under review. The methods, results, and discussion in the chapter are the same as in the manuscript, although the introductory material was relocated to Chapter 1.

5.2. Experimental setup

5.2.1. Strain, growth medium, and culturing conditions

The *D. vulgaris* culture used in the previous studies was grown in ATCC 1249 medium, and the cells were transferred to fresh medium every four to seven days. The details of medium preparation and transferring are described in 2.2.1.

5.2.2. Medium modification and iron sources

In all experiments, ATCC 1249 medium was modified by replacing FAS with a target iron source and replacing $MgSO_4$ with $MgCl_2$; the latter was done to keep the Mg concentration constant as the sulfate concentration was varied. $FeCl_2$ and $FeCl_3$ powders, purchased from Sigma (St. Louis, MO), were the sources of soluble Fe(II) and Fe(III), respectively. The three Fe(III)-(hydr)oxide mineral sources -- goethite (α-FeOOH), hematite (α-Fe_2O_3), and 2-line ferrihydrite ($Fe_2O_3 \cdot 0.5H_2O$) -- were synthesized as described by Schwertmann and Cornell[346] and added to the matrixes at the same molar concentration. The average solid surface areas were 80

m^2/g, 30 m^2/g, and 200-300 m^2/g, respectively[346]. For all experiments, the electron-equivalent concentrations of lactate and pyruvate were equal, and greater than the electron-equivalent concentrations of all electron acceptors (SO_4^{2-} and Fe^{3+}).

The modified media were deoxygenated by bubbling N_2 gas and then distributed in the sterile 160-ml serum bottles (100 ml media per bottle) in an anaerobic glove box. These experimental bottles were sealed with rubber stoppers and aluminum caps with a headspace of N_2 gas, and then they were autoclaved 15 minutes at 121℃. All iron sources other than $FeCl_2$ were added with other components at the beginning. A concentrate of $FeCl_2$ (1.5 M Fe) in anoxic DI water was prepared in the anaerobic glove box beforehand, and then a certain amount of the filtered concentrate, according to the stoichiometry, was injected into the autoclaved experimental bottles. The inocula were from the culturing bottles after three days growth. 3 ml of inoculum were injected into each experimental bottle in order to keep the initial protein concentration around 5 mg/l. The inoculated bottles were then transferred immediately to the shaker (200 rpm) and incubated at 30℃.

5.2.3. Analytical methods

pH, concentrations of soluble Fe(III) and total soluble Fe, anions (sulfate and phosphate), volatile fatty acids (acetate, lactate, pyruvate, and formate) were analyzed routinely. The detailed information is in 2.2.3.

5.2.4. Separation of iron sulfide solids from culture medium

After complete lactate consumption was achieved, the precipitates were separated from the bottles, rinsed, freeze dried, and stored under anaerobic conditions for further analysis by XRD and transmission electron microscope equipped with energy-dispersive X-ray spectroscopy (TEM/EDX). The detailed procedure is described in 2.2.4.

5.2.5. X-Ray Diffraction (XRD) analysis

XRD was performed using a Rigaku D/Max-IIB diffractometer with monochromated Cu *K*α radiation. The procedures of XRD scanning and average mackinawite particle sizes calculation are described in 2.2.7.

5.2.6. TEM/EDX analysis

The powdered sample was loaded on a Lacey carbon 300-mesh copper TEM grid (Ted-Pella, Inc., Redding, CA, USA). TEM images were captured using a Philips CM200-FEG high resolution TEM/STEM (FEI Corp., Eindhoven, The Netherlands) operated at 200 kV, and elemental compositions at selected areas were identified using an EDX detector (EDAX Inc., Mahwah, NJ, USA).

5.2.7. Mass-distribution calculations

I developed a spreadsheet-based mass-balance and equilibrium model based on the approach of Tang et al.[347]. The first principle of the model is mass balance for all components. The molar mass balances for all species of sulfur, carbonate, phosphate, citrate, and ammonia are in eqns. 5.1-5.5, respectively:

$$C_{S^{2-},\,\text{free}}\left(V_g + V_l\right) = C_{H_2S_{(g)}} \cdot V_g + \left(\left[H_2S\right] + \left[HS^-\right] + \left[S^{2-}\right]\right) \cdot V_l \qquad (5.1)$$

$$C_{CO_2,\,\text{total}}\left(V_g + V_l\right) = C_{CO_2\,(g)} \cdot V_g + \left(\left[CO_2\right] + \left[HCO_3^-\right] + \left[CO_3^{2-}\right]\right) \cdot V_l \qquad (5.2)$$

$$C_{PO_4,\,\text{total}} = \left[H_3PO_4\right] + \left[H_2PO_4^-\right] + \left[HPO_4^{2-}\right] + \left[PO_4^{3-}\right] \qquad (5.3)$$

$$C_{\text{Cit, total}} = \left[H_3\text{Cit}\right] + \left[H_2\text{Cit}^-\right] + 2\left[\text{HCit}^{2-}\right] + 3\left[\text{Cit}^{3-}\right] \qquad (5.4)$$

$$C_{NH_3,\,\text{total}}\left(V_g + V_l\right) = C_{NH_3\,(g)} \cdot V_g + \left(\left[NH_3\right] + \left[NH_4^+\right]\right) \cdot V_l \qquad (5.5)$$

where C_i is the total mole/L concentration of component *i*, [*Xj*] is the mole/L concentration of species *j*, V_g is the headspace volume, and V_l is the liquid volume. To take into account the gas-phase partitioning of CO_2, NH_3, and H_2S, I assumed equilibrium between their gas- and liquid-phase concentrations according to the dimensionless Henry's law constant (K_H)[348].

The second principle is that all of the acid/base reactions are at equilibrium, which is expressed quantitatively with mass-action equations and acidity constants (K_a) [348]. Eqns. 5.6 and 5.7 give an example of the mass-action equations for the NH_4^+/ NH_3 equilibrium of eqn. 3.5:

$$C_{NH_3\,(g)} = H_k\left(\left[NH_3\right] + \left[NH_4^+\right]\right) \qquad (5.6)$$

$$\left[NH_4^+\right] = k_a\left[NH_3\right] \qquad (5.7)$$

I did not make activity corrections, which means that I used mole/L concentration in the mass-action equations.

The third principle of the model is that, at the end of the experiment (i.e., just before we opened the bottles), the pH and alkalinity conform to the proton condition for all chemical species active in acid/base reactions[347, 348]:

$$\begin{aligned}[\mathrm{Alk}] &= [\mathrm{OH^-}] + [\mathrm{HS^-}] + 2[\mathrm{S^{2-}}] + [\mathrm{HCO_3^-}] + 2[\mathrm{CO_3^{2-}}] + [\mathrm{H_2PO_4^-}] + 2[\mathrm{HPO_4^{2-}}] \\ &\quad + 3[\mathrm{PO_4^{3-}}] + [\mathrm{H_2Cit^-}] + 2[\mathrm{HCit^{2-}}] + 3[\mathrm{Cit^{3-}}] - [\mathrm{H^+}] - [\mathrm{NH_4^+}] \\ &= [\mathrm{Na^+}] + [\mathrm{K^+}] + 2[\mathrm{Ca^{2+}}] + 2[\mathrm{Mg^{2+}}] + 2[\mathrm{Fe^{2+}}] - [\mathrm{Cl^-}] - 2[\mathrm{SO_4^{2-}}] \\ &\quad - [\mathrm{Lac^-}] - [\mathrm{Ac^-}] \end{aligned} \qquad (5.8)$$

where Alk stands for alkalinity, Cit stands for citrate, Lac stands for lactate, and Ac stands for acetate.

I made a few assumptions to simplify the model:

1. Total concentrations of non-transformed components in the original medium (citrate, calcium, magnesium, chloride, sodium, and potassium) were constant throughout the experiments.
2. The very small uptakes of ammonium and phosphate for bacterial synthesis[273] were neglected.
3. Lactate fermentation produced an equal concentration of total carbonate □i.e. $C_{CO2,\ total}$ = Δ[lac]□.

To solve the model, I applied the following input concentrations from our measurements:

- $[\text{sulfate}]_{final}$
- $[Fe^{2+}]_{final}$
- pH_{final}
- Organic compounds: $[Lac]_{final}$, $[Ac]_{final}$, and $[Cit]_{toal}$
- $C_{CO2,\ total}$
- Other inorganic ions: ($[Na^+]$, $[NH_4^+]$, $[Ca^{2+}]$, $[Mg^{2+}]$, and $[Cl^-]$).

To yield the output of $C_{s2-,\ free}$, I set up the *solver*, an add-in program in Excel, to iterate eqn. S8 for $C_{s2-,\ free}$ until the targeted pH equaled the measured pH on the basis of eqns. 5.1 – 5.8.

With pH and $C_{S2,\ free}$ known, I then calculated C_{s0}, C_{FeS}, and $C_{Fe(III)\ (hydr)xodes,\ remaining}$ according to eqns. 5.9 – 5.11:

$$C_{Fe(III)\ (hydr)oxide,\ total} = \left[Fe^{2+}\right] + C_{FeS} + C_{Fe(III)\ (hydr)oxide,\ remaining} \quad (5.9)$$

$$C_{S,\ total} = \left[SO_4^{2-}\right]_{initial} = \left[SO_4^{2-}\right]_{final} + C_{S^{2-},\ total} + C_{S^0} \quad (5.10)$$

$$C_{S^{2-},\ total} = C_{S^{2-},\ free} + C_{FeS} \quad (5.11)$$

Tables 5.1 and 5.2 summarize measured and calculated results for all batch experiments, respectively.

Table 5.1. Measured sulfate, soluble Fe^{2+}, formate concentrations; pH; experimental durations; and particle thicknesses of biogenic mackinawite for all iron-source conditions when lactate or pyruvate was the electron donor.

		[Sulfate]		[Fe^{2+}]	[Formate]	pH		Duration*	Mackinawite thickness
		Initial	*final*	*final*	*max.*	*initial*	*final*		
Iron source	Electron donor	(mmole / bottle)				(s.u.)		(day)	(nm)
Soluble Fe^{2+}	Lactate	2.5	0.3	0.0	0.0	7.3	7.0	4	12.2
	Pyruvate	1.2	0.0	0.0	0.0	6.9	6.1	7	28.4
Soluble Fe^{3+}	Lactate	2.7	0.9	0.0	0.0	7.2	7.1	4	5.3
	Pyruvate	1.3	0.0	0.0	0.0	6.6	6.2	7	8.1
Goethite	Lactate	1.4	0.0	0.1	0.6	7.2	7.4	6	-
	Pyruvate	1.5	0.2	0.3	2.1	7.1	6.5	6	-
Hematite	Lactate	1.2	0.0	0.2	0.2	6.9	7.6	20	-
	Pyruvate	1.2	0.0	0.8	9.1	7.0	6.6	20	-
Ferrihydrite	Lactate	1.3	0.0	0.7	0.1	7.1	8.0	43	6.8
	Pyruvate	1.6	0.0	0.7	4.2	7.1	7.0	43	6.2

* Counted from the day when the bottles were inoculated to the day when the bottles were opened for solid collection.

Table 5.2. Mass distributions of iron, sulfur, and solid phases at the end of the experiments using goethite, hematite, or ferrihydrite as the iron-based electron acceptor and lactate or pyruvate as the electron donor.

Iron source		Goethite		Hematite		Ferrihydrite	
Electron donor		Lactate	Pyruvate	Lactate	Pyruvate	Lactate	Pyruvate
Iron species	Fe(III) (Hydr)oxide	20%	3%	68%	3%	24%	2%
(mole / mole)	Soluble Fe^{2+}	11%	25%	8%	28%	25%	27%
	$FeS_{(s)}$	69%	72%	24%	45%	51%	60%
	Vivianite [$Fe_3(PO_4)_2 \cdot 8H_2O_{(s)}$]	0%	0%	0%	24%	0%	11%
Sulfur species	Sulfate	0%	0%	0%	0%	0%	1%
(mole / mole)	Soluble sulfide	0%	0%	0%	1%	0%	0%
	$FeS_{(s)}$	63%	64%	50%	99%	100%	99%
	Elemental sulfur [$S^{\circ}_{(s)}$]	37%	36%	50%	0%	0%	0%
Final Solids	Fe(III) (Hydr)oxide$_{(s)}$	19%	4%	66%	3%	30%	2%
(g / g)	$FeS_{(s)}$	67%	82%	25%	57%	70%	79%
	Elemental sulfur [$S^{\circ}_{(s)}$]	14%	14%	9%	0%	0%	0%
	Vivianite [$Fe_3(PO_4)_2 \cdot 8H_2O_{(s)}$]	0%	0%	0%	40%	0%	19%

5.3. Bacterial growth and solid formation with soluble Fe sources

5.3.1. Lactate as the electron donor

In the bottles with $FeCl_2$ as the iron source (i.e., soluble Fe^{2+} chelated by citrate ions in the matrix), sulfate was the sole electron acceptor. Figure 5.1A shows that sulfate was 87% reduced to sulfide by *D. vulgaris* within three days. Soluble Fe^{2+} decreased along with sulfate reduction, indicating the formation of FeS precipitates from biogenic sulfide.

Bottles with $FeCl_3$ (i.e., soluble Fe^{3+} chelated by citrate ions in the matrix) had Fe^{3+} as an additional electron acceptor. Figures 5.1B shows that Fe^{3+} was reduced without delay after inoculation, but SO_4^{2-} reduction was inhibited until all Fe^{3+} was reduced to Fe^{2+}. The retardation of SO_4^{2-} reduction and sulfide production allowed for temporary accumulation of soluble Fe^{2+} in the medium. This phenomenon is consistent with the observation by Elias et al. that Fe(III) reduction had priority over sulfate reduction[121]. The unique pathway of electron flow in *D. vulgaris* cell -- featuring sulfate and Fe(III) reductions at different locations (Fig 1.2) -- illustrates why Fe(III) accepts electrons preferentially over sulfate. Thus, when Fe^{3+} was readily available, its reduction consumed the entire electron flow and suppressed sulfate reduction.

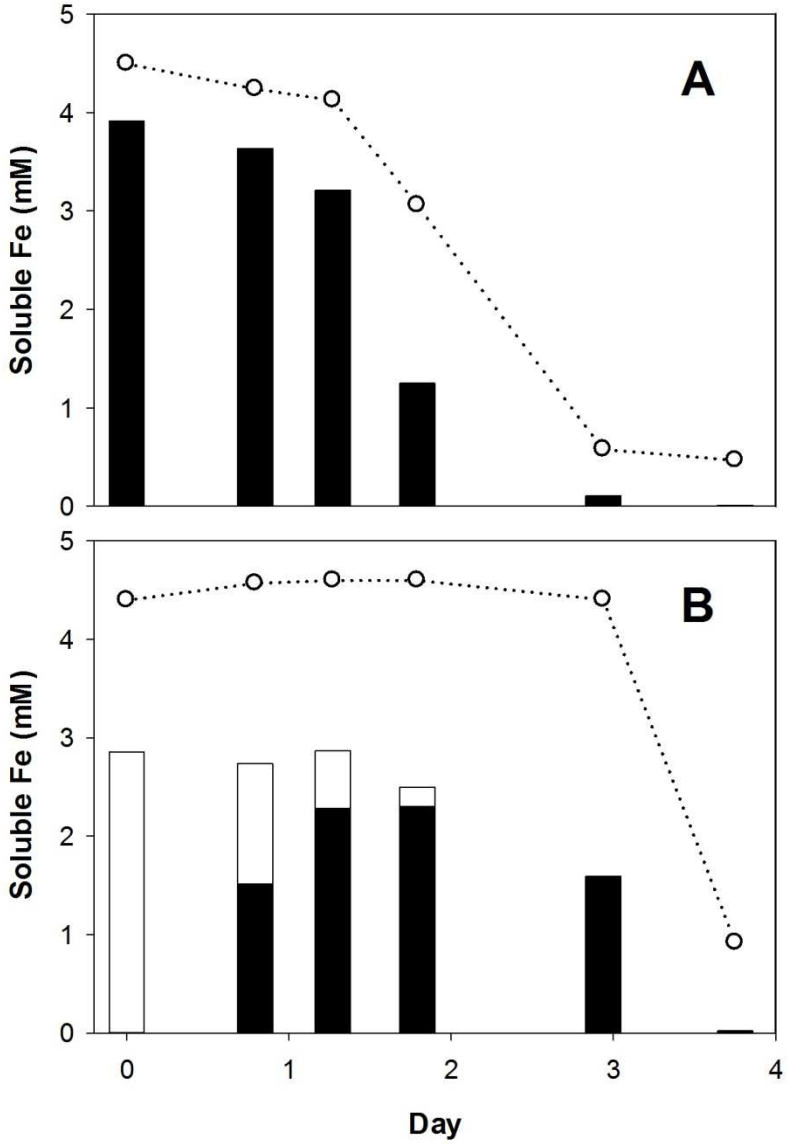


Fig 5.1 Concentrations of soluble Fe(II) (black bars), soluble Fe(III) (white bars), and sulfate (○) during the growth of *D. vulgaris* with lactate as the electron donor plus soluble Fe^{2+} as the iron source (A) or soluble Fe^{3+} as the iron source (B).

The XRD analyses in Figure 5.2 show that pure mackinawite was present in both solid samples collected from the bottles with soluble iron sources. The mackinawite produced from soluble Fe^{2+} had higher crystallinity (narrower diffraction peaks with higher intensity in Fig. 5.2) and larger particle size (12.2 nm) than mackinawite from soluble Fe^{3+} (broader peaks and 5.3 nm of particle size); this probably was due to the earlier formation of FeS and the longer period for subsequent crystallization.

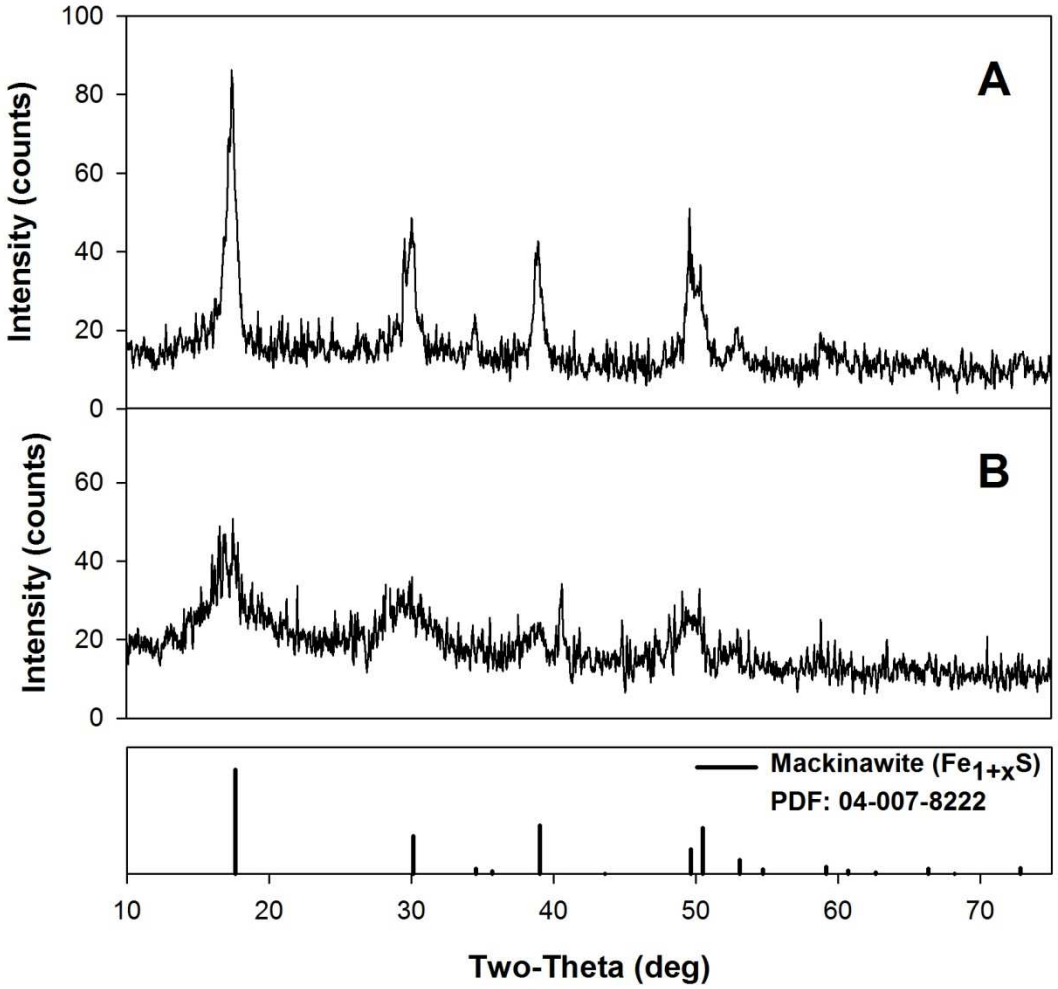


Fig 5.2 XRD spectra of solids separated from media with soluble Fe^{2+} as the iron source (A) or with soluble Fe^{3+} as the iron source (B).

5.3.2. Pyruvate as the electron donor

5.3.2.1. Soluble Fe^{2+} as the iron source

In the bottles with $FeCl_2$ (soluble Fe^{2+}) as the iron source, sulfate was the sole electron acceptor. As shown in Figure 5.3A, *D vulgaris* reduced 95% of the starting sulfate to sulfide by *D. vulgaris* within three days. This was slightly greater conversion than when lactate was the electron donor (87%). Soluble Fe^{2+} decreased in parallel with sulfate reduction, forming FeS precipitates by combining with the biogenic sulfide (Figs 5.3A). The fermentation of pyruvate to acetate has a significantly lower Gibbs free energy ($\Delta_r G^{0'}$; -47.1 kJ/mole) than the fermentation of lactate to pyruvate (+43.2 kJ/mole)[274]. These results suggest that lactate fermentation to pyruvate was the limiting step during complete lactate fermentation to acetate.

The final pH after the 7-day incubation dropped from 6.9 to 6.1, while the final pH was still around neutral when lactate was the electron donor (Table 5.1). These are consistent with the stoichiometry (Eqns 1.12 and 1.13): To reduce an equivalent amount of electron acceptor, pyruvate fermentation produces double the protons of lactate fermentation, resulting in lower pH.

The XRD patterns in Fig 5.4 reveal that the final solid product was crystalline mackinawite with a notably larger particle thickness (28.4 nm; Table 5.1) than for the mackinawite from using lactate as the donor (12.2 nm; Table 5.1). This is consistent with the conclusion from previous research that a lower final pH (6.1 in this pyruvate experiment; Table 5.1) enhanced crystallization of mackinawite[223].

5.3.2.2. Soluble Fe^{3+} as the iron source

The bottles with $FeCl_3$ featured concomitant reductions Fe^{3+} and SO_4^{2-} coupled with pyruvate fermentation. Fe^{3+} was reduced without delay after inoculation, but sulfate reduction was retarded until Fe^{3+} was completely reduced to Fe^{2+} (Fig 5.3B). The priority of Fe^{3+} reduction over sulfate reduction was probably due to the unique pathway of electron flow in *D. vulgaris* cells, which allows Fe(III) to intercept electrons at cytochrome c_3 in the periplasm before they reach SO_4^{2-} in the cytoplasm (Fig. 1.2).

While the priority of Fe^{3+} reduction over sulfate reduction was complete with lactate, some sulfate reduction still took place in parallel to Fe^{3+} reduction when pyruvate was the electron

donor: 10% sulfate loss with 65% Fe^{3+} reduction on day 3 and 16% sulfate loss with 98% Fe^{3+} reduction on 5 day 5 (Fig 5.3B). This indicates that the reaction rate of Fe(III) reduction is higher than electron production from lactate to pyruvate, but not higher than electron production from pyruvate to acetate. Under this scenario, all the electrons from lactate fermentation can be rapidly scavenged by Fe(III) at cytochrome c_3, while not all the electrons from pyruvate fermentation can be accepted by Fe(III), allowing the surplus of electrons be transported by the cytochrome network to the cytoplasm for sulfate reduction. This phenomenon adds weight to our conclusion above that lactate fermentation towards pyruvate was the limiting step during the whole process.

Retarded SO_4^{2-} reduction in the presence of Fe^{3+} means that the formation of FeS began later in the experiment than with Fe^{2+} added directly, and the consequently shorter period for crystallization lead to poorly crystalline mackinawite (Fig 5.4B). However, the mackinawite particle thickness was higher with pyruvate than with lactate (8.1 nm vs 5.1 nm, respectively; Table 5.1) due to a lower pH with pyruvate (6.2; Table 5.1).

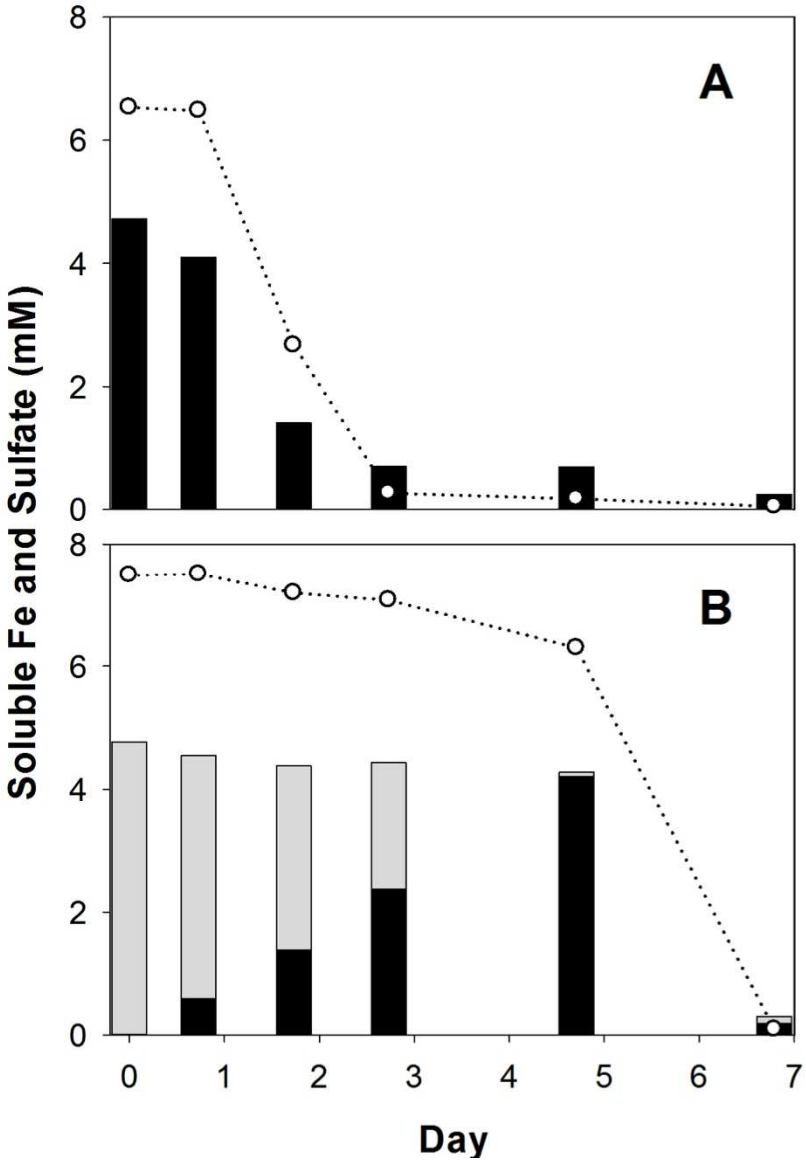


Fig 5.3 Concentrations of soluble Fe(II) (black bars), soluble Fe(III) (grey bars), and sulfate (○) during the growth of *D. vulgaris* with pyruvate as the electron donor plus soluble Fe^{2+} as the iron source (A) or soluble Fe^{3+} as the iron source (B).

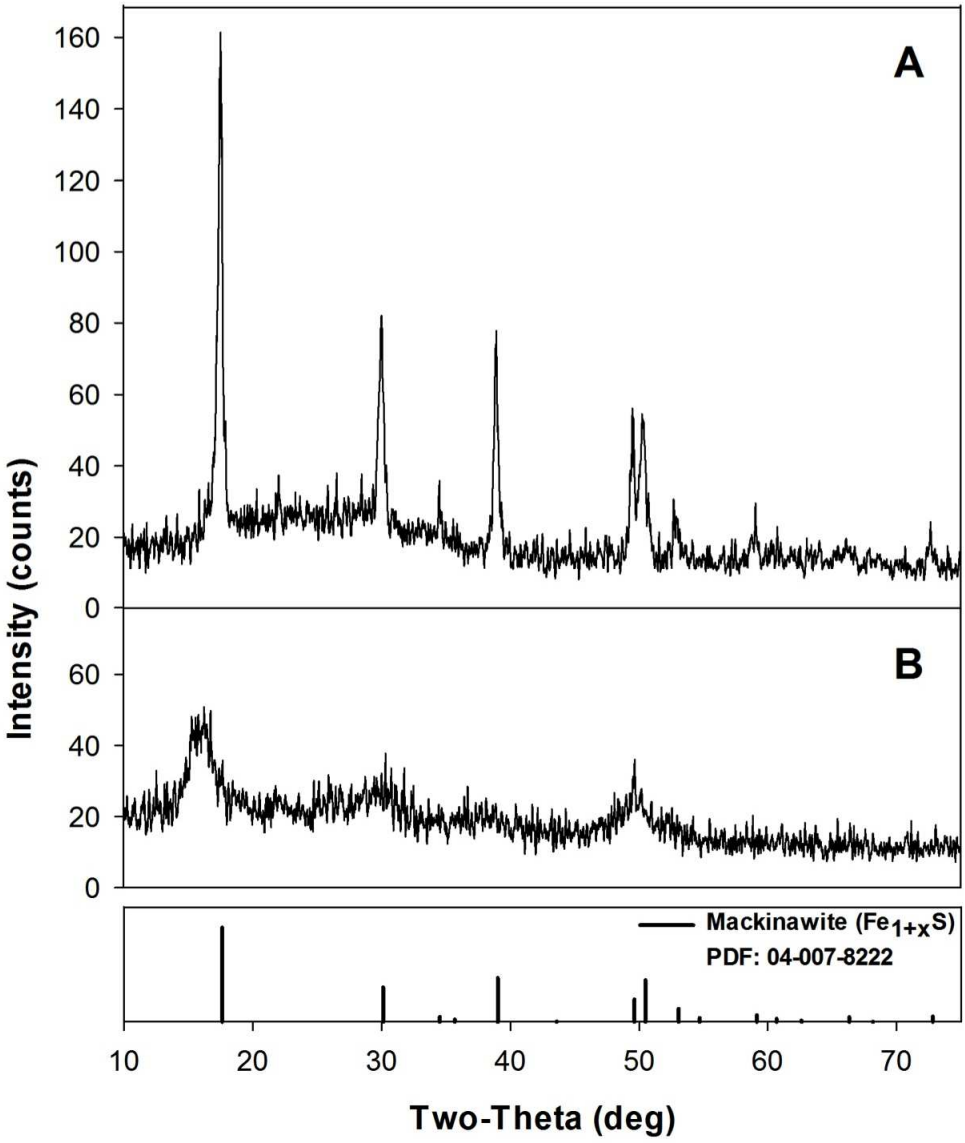


Fig 5.4 XRD spectra of solids separated from media with pyruvate as the electron donor plus soluble Fe^{2+} as the iron source (A) or with soluble Fe^{3+} as the iron source (B).

5.4. Results for Bacterial growth and solid formation with Fe(III) (hydr)oxides

5.4.1. Lactate as the electron donor

5.4.1.1. Sulfate versus Fe(III) reduction

Figure 5.5 shows that the patterns of bacterial growth and substrate utilization were similar to each other in the bottles with goethite (G+L), hematite (H+L), and ferrihydrite (F+L), but they differed from the patterns with soluble iron. In contrast to the priority of soluble Fe(III) utilization over sulfate utilization, the accumulation of soluble Fe^{2+} (attributed to solid-Fe(III) reduction) was observed only after all SO_4^{2-} was reduced (Figs 5.5-A1, 5.5-B1, and 5.5-C1). This delayed reduction of Fe(III) from all Fe(III) (hydr)oxides is expected, as the crystalline phases of Fe(III) (hydr)oxides are less bioavailable than soluble Fe(III) due to the need for extracellular electron transfer and dissolution of the Fe(III) solid[123, 231]. Thus, Fe^{3+} reduction was not fast enough to intercept the electron flow to sulfate reduction.

5.4.1.2. Enzymatic versus chemical Fe(III) reduction

In all conditions, soluble Fe^{2+} was released from reduction of the Fe(III)-(hydr)oxide solids. Rather than being rapidly scavenged by H_2S already produced from SO_4^{2-} reduction, soluble Fe^{2+} accumulated; moreover, the concentration of soluble Fe^{2+} continued to increase after the consumption of lactate ceased (Figs 5.5-A1, 5.5-B1, and 5.5-C1), which is a direct sign that sulfide was the chemical reductant to form Fe^{2+}. These trends are consistent with previous research[235, 349] that demonstrated concurrent Fe(III)-solid reduction by enzymatic (Eqns 1.6 – 1.8) and chemical (Eqns 1.9 – 1.11) mechanisms. In addition, the gradual release of soluble Fe^{2+} over a long period, coupled with the absence of soluble Fe^{3+}, is in accord with rate limitation from the dissolution of the Fe(III) solid to release Fe^{2+} [246].

The maximum concentrations of accumulated soluble Fe^{2+} were 11% (0.8 mM), 8% (1.2 mM), and 25% (3.7 mM) of the total iron added as goethite, hematite, and ferrihydrite, respectively. A higher concentration of accumulated soluble Fe^{2+} indicates that more Fe(III) (hydr)oxide was reduced. Ferrihydrite has the largest surface area (200-300 m^2/g)[346], as well as

the highest redox potential (E_0' = –0.1 V; Table 1.2); consequently, it was reduced more rapidly and completely than goethite and hematite.

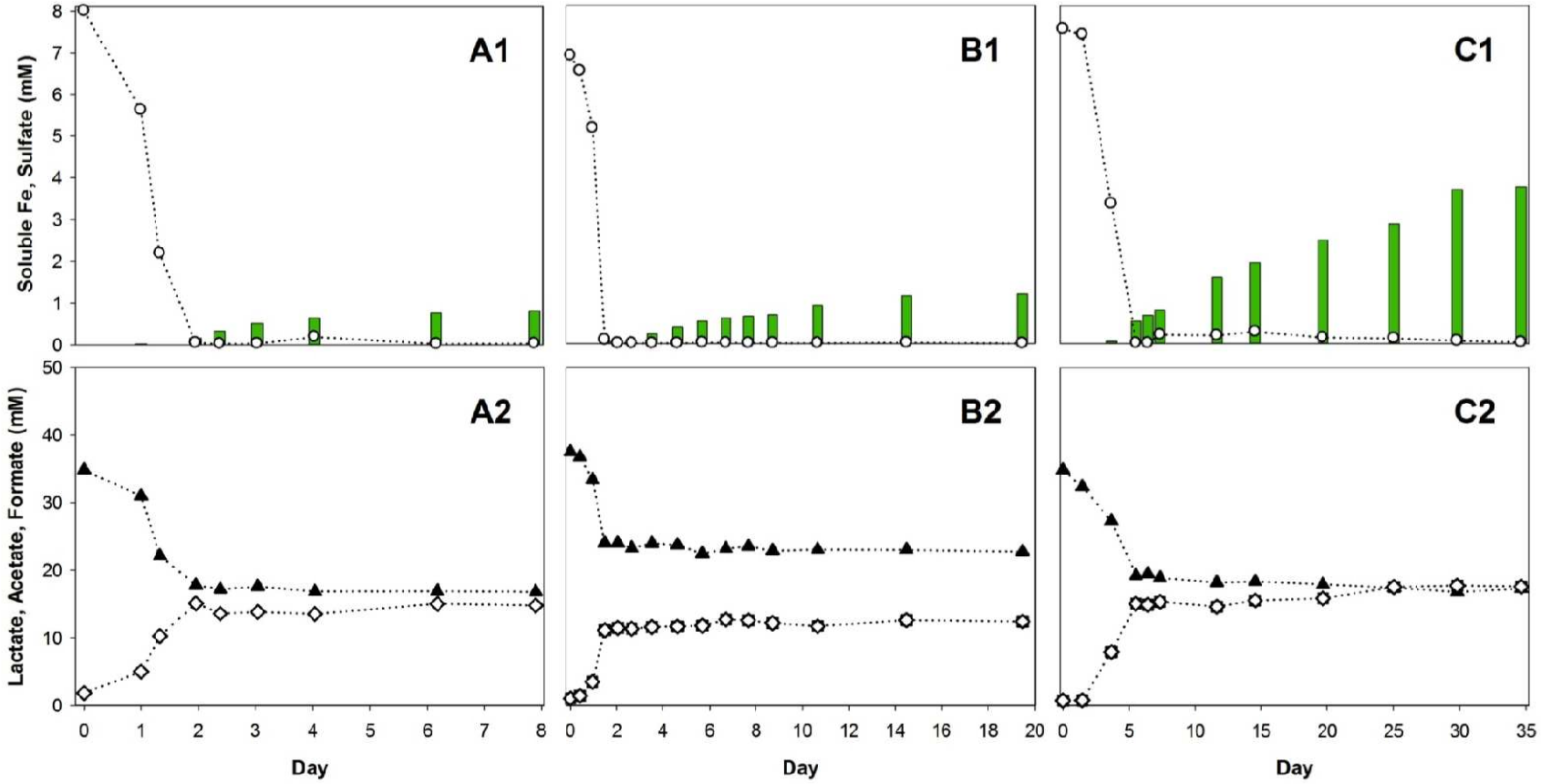


Fig 5.5 Concentrations of soluble Fe(II) (bars), sulfate (○), lactate (▲), and acetate (□) during the growth of *D. vulgaris* with lactate as the electron donor and with goethite (α-FeOOH, A1 and A2), hematite (α-Fe_2O_3, B1 and B2), or ferrihydrite ($Fe_2O_3 \cdot 0.5H_2O$, C1 and C2) solids as the solid-phase electron acceptor.

5.4.1.3. Solid production and characterization

The TEM-EDX and XRD results with the solid forms of Fe^{3+} are shown in Figure 5.6 and 5.7, respectively. Crystalline mackinawite clearly was present in the F+L bottles (Figure 5.7C), although it was poorly crystallized, having only broad peaks and small particle size (4.5 nm). In addition, we observed lattice fringes in a limited area of the solid sample from the H+L bottle (Fig. 5.8): higher average spacing (5.3±0.1Å) corresponded to *d*-spacing of (001) planes of mackinawite, while smaller average spacing (3.3±0.5Å) corresponded to *d*-spacing of (101) planes of mackinawite[350-352]. The thickness of individual crystals calculated by multiplying the number of (001) fringes by the average *d*-spacing was 4.8 nm. This value is very close to the thickness of mackinawite from the F+L bottle (4.9 nm; Table 5.1) calculated on basis of the XRD data. The detectable FeS solids were either in amorphous states or nanocrystalline mackinawite, suggesting a retarded crystallization process, probably due to depletion of sulfide, as reported by previous research [220, 224, 343].

On the other hand, it is difficult to infer from either the XRD patterns or TEM images whether or not mackinawite was present in the G+L and H+L bottles (Figures 5.7A and 5.7B). The characteristic peaks of hematite can be observed (Figure 5.7B), revealing that a significant portion of hematite remained in the final solid samples.

According to the mass distributions shown in Table 5.2, biogenic FeS solids produced from ferrihydrite were most abundant (1.3 mmole/bottle, 50.5% of the total iron added as ferrihydrite), while hematite produced the least FeS solids (0.5 mmole/bottle, 20% of the total iron added as hematite). EDX analyses further confirm this trend: Solids from the H-L bottle had a lower S:Fe signal ratio than solids from other two bottles (Fig 5.6). Hence, the yield of FeS solids correlated to the bioavailability of the iron source. The mass-balance results also point out that a significant fraction of the initial sulfate-S was S° for goethite and hematite (36% and 50%, respectively), although no crystalline elemental S was detected by XRD, probably due to its presence in an amorphous form. The absence of S° with ferrihydrite reveals that enzymatic reduction dominated over chemical reduction of Fe(III) in this case; this reinforces that ferrihydrite was more bioavailable than goethite and hematite.

In addition, lack of crystalline pyrite in the XRD analysis indicates that polysulfide was not produced by reduction of S°; any polysulfide formed would have reacted rapidly with either FeS solids or soluble Fe^{2+} and HS^- to form pyrite[353-357]. Thus, S° was the terminal product from chemical reduction of Fe(III) (hydr)oxides.

Finally, When lactate was the electron donor, the phosphate concentration in the medium was almost constant (2.6±0.3 mM) through the incubation period in the G+L bottle, but gradually dropped by 0.9±0.1 mM after day 8 and day 6 in the H+L and F+L bottles, respectively. Phosphate loss corresponded to pH higher than 7.4. In addition, EDX detected strong signals of calcium (Ca) and phosphorous (P), plus weaker signals of magnesium (Mg), in all three samples. The presence of P corresponded with phosphate loss in the H+L and F+L bottles. Further EDX scanning in selected areas (Fig 5.9) reveals that Ca, Mg, and P were mostly at the edges, but not in the center of the aggregate. XRD scanning did not detect crystalline Ca-Mg-P minerals, such as brushite ($CaHPO_4 \cdot 2H_2O$), whitlockite [$Ca_9MgH(PO_4)_7$], or apatite [$Ca_5(PO_4)_3OH$]; this suggests amorphous forms of Ca-Mg-P solids.

Previous research[358] reported the precipitation in the form of $Ca_5(PO_4)_3OH$ at slightly alkaline pH values (normally higher than 7.4). Lactate fermentation coupled with sulfate and Fe(III) reductions consumed protons, resulting in a pH increase; as a result, the final pHs in all lactate-stimulated bottles were all above 7.4; this allowed calcium and phosphate precipitation in the possible form of $Ca_5(PO4)_3OH$.

In addition, XRD scanning did not detect any Ca- or P- associated crystallites in lactate-stimulated bottles (Fig. 5.7), indicating the precipitates were still amorphous, in line with the proposed inhibitive effect of Mg on $Ca_5(PO4)_3OH$ crystallization towards apatite by substituting in and disrupting of the calcium phosphate crystal lattice or by adsorbing onto the growing calcium phosphate crystals[359, 360].

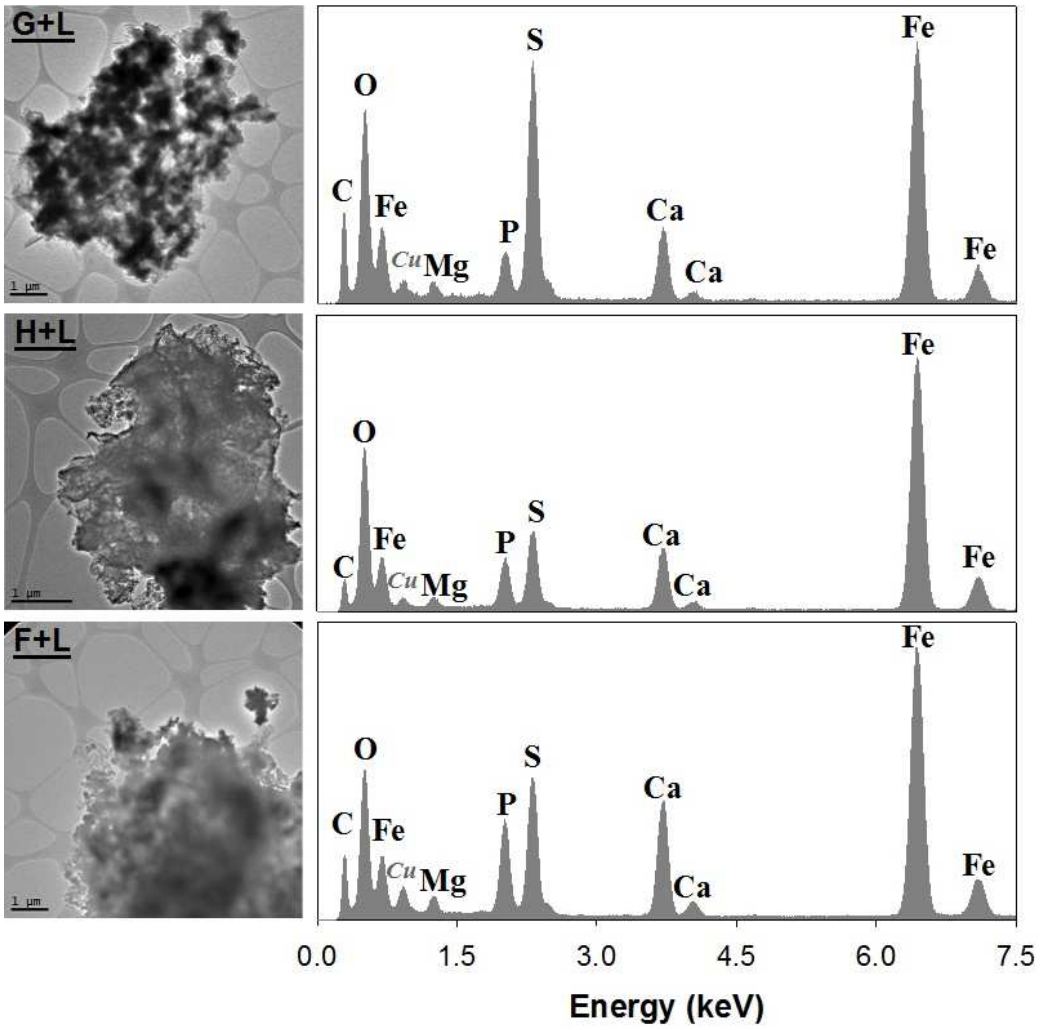


Fig 5.6 TEM images (left column) and EDX spectra (right column) of solids separated from media with goethite plus lactate (G+L), hematite plus lactate (H+L), and 2-line ferrihydrite plus lactate (F+L).

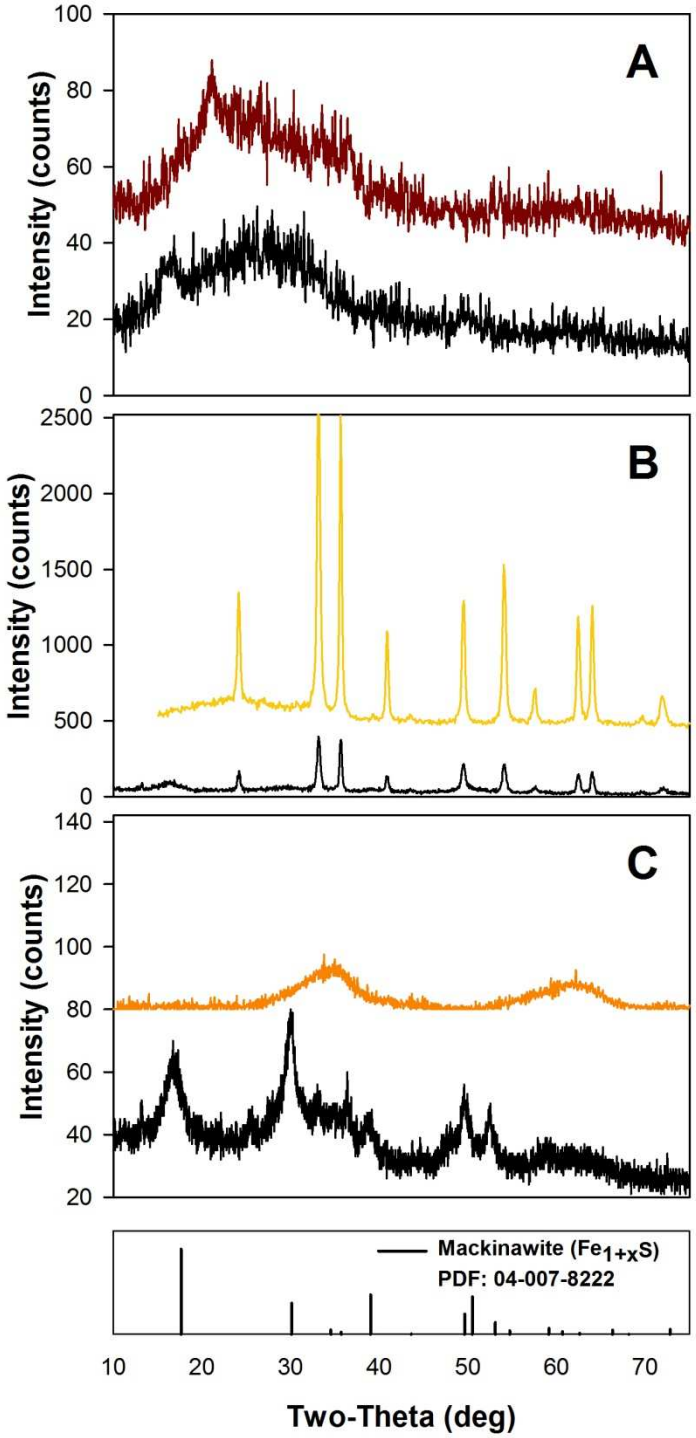


Fig 5.7 XRD spectra of synthetic goethite (α-FeOOH, top line in A), hematite (α-Fe_2O_3, top line in B), 2-line ferrihydrite ($Fe_2O_3 \cdot 0.5H_2O$, top line in C), and biogenic solids from bottles G+L (bottom line in A), H+L (bottom line in B), and F+L (bottom line in C). Lactate was the electron donor in all cases.

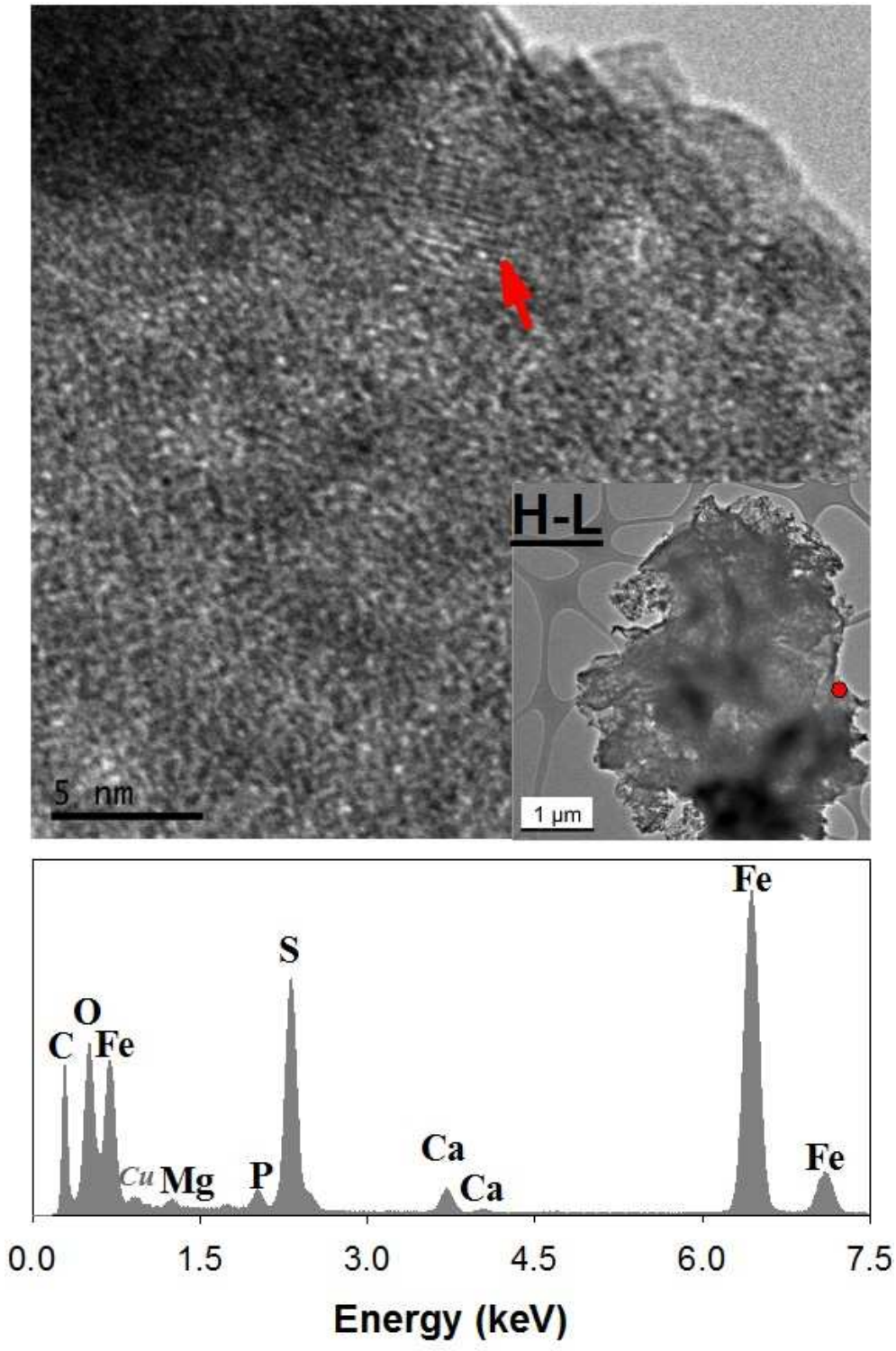


Fig 5.8 The TEM image and the EDX spectrum of a nm-level spot showing crystal lattices in the solids from bottle with hematite plus lactate (H-L). The red dot indicates the selected area for EDX scanning, and the red arrow indicates the lattice fringes.

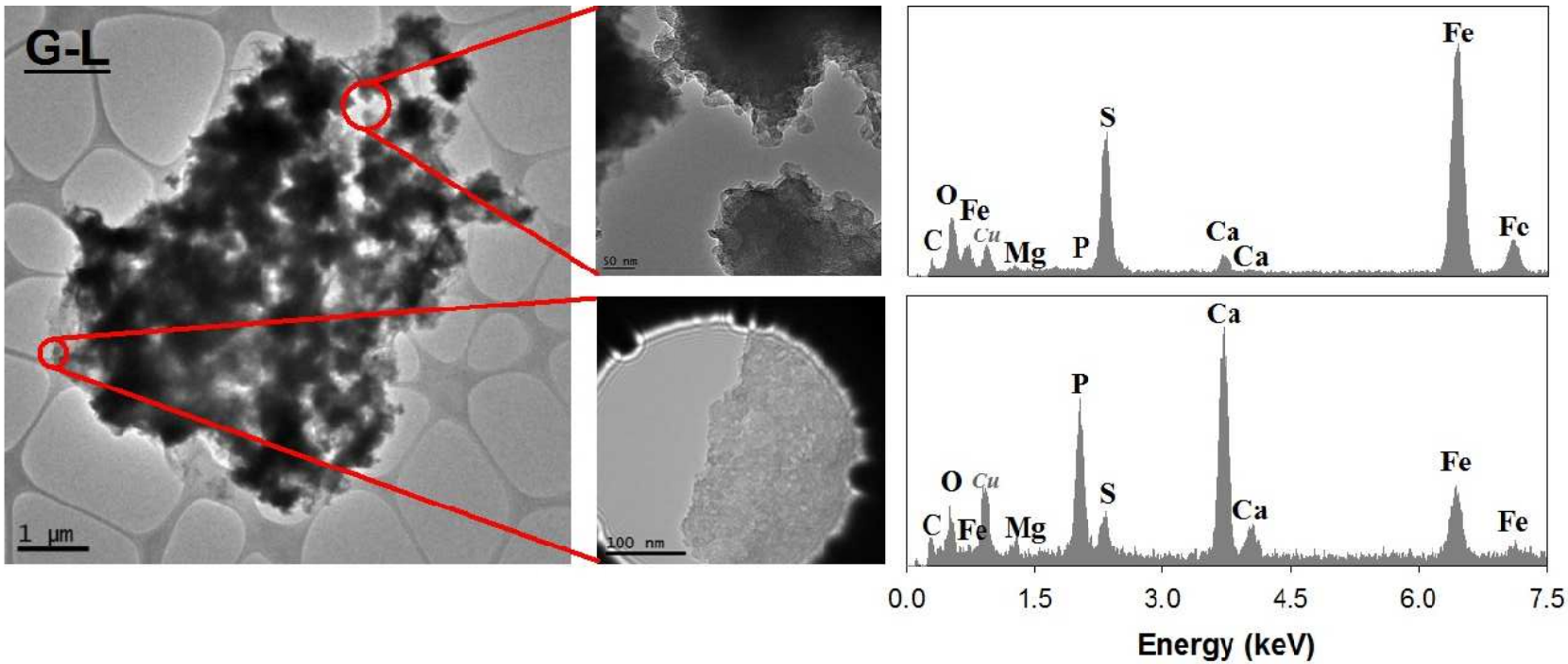


Fig 5.9 TEM images and the comprehensive EDX results of two spots in the solids produced from the bottle with goethite plus lactate (G-L). Ca and P have much higher signals at the edge.

5.4.2. Pyruvate as the electron donor

5.4.2.1. Sulfate versus Fe(III) reduction

As shown in Figure 5.10, Fe(III) reduction and sulfate reduction commenced almost simultaneously in the presence of the solid sources of Fe(III). However, SO_4^{2-} reduction slowed after noticeable soluble Fe^{2+} began to occur on the second day; this contrasts to the lactate results, in which the soluble Fe^{2+} did not accumulate until sulfate was completely reduced and sulfate reduction was not retarded. As a result, *D. vulgaris* required a longer time to reduce 99% sulfate using pyruvate than using lactate.

5.4.2.2. Enzymatic versus chemical Fe(III) reduction

Soluble Fe^{2+} was released from reduction of the Fe(III) solids for all experiments, and it continued to accumulate even though biogenic H_2S was present (indicated by sulfate loss); moreover, the concentration of soluble Fe^{2+} increased even after pyruvate was consumed. Fe^{2+} accumulation after donor consumption demonstrates enzymatic reduction by bacteria and chemical reduction by the biogenic sulfide, and it is consistent with previous studies[235, 349]. The maximum concentrations of accumulated soluble Fe^{2+} were 23% of original goethite (1.7 mM), 28% of original hematite (5.5 mM), and 27% of original ferrihydrite (4.6 mM). These soluble Fe^{2+} concentrations were higher than with lactate, reflecting that using pyruvate as the electron donor led to more enzymatic reduction of Fe(III) (hydr)oxides by *D. vulgaris*.

5.4.2.3. Formate accumulation and consumption

While H_2 was never detected in the headspace, the transient accumulation of formate was observed for all the conditions. When pyruvate was the electron donor, the maximum concentrations of accumulating formate were 15% of the consumed electron donor in e^- equivalent for goethite (11.5 mM), 23% for hematite (50.7%), and 13% (25.2 mM) for ferrihydrite. These concentrations are significantly higher than the lactate (3.3 mM, 1.1 mM, and 0.6 mM for goethite, hematite, and ferrihydrite, respectively; Table 5.1).

D. vulgaris is capable of conserving energy by respiration of the electron equivalents in hydrogen and formate. In the lactate experiments, certain amounts of lactate remained in the matrix due to inhibition from H_2 in the headspace (although below the detection limit) to the

further fermentation. In contrast, formate generated from pyruvate fermentation was soluble and had no inhibitive effect on bacterial activity; thus, formate allowed fast and complete consumption of pyruvate (Figs 5.10-A2 to 5.10-C2). This significantly enhanced the utilization efficiency of electron donor.

5.4.2.4. Vivianite formation

The greater accumulation of soluble Fe^{2+} from hematite and ferrihydrite (6 mM on the 11th day and 5 mM on the 25th day, respectively; Figs 5.10-B1 and 5.10-C1) exceeded the threshold of citrate chelation (c.a. 5 mM) and allowed precipitation of vivianite. Consequently, the soluble Fe^{2+} concentrations decreased by 1.3 mM and 0.8 mM, concomitant with 2.0 mM (91%) and 1.0 mM (72%) phosphate loss, respectively (Figs 5.10-B2 and 5.10-C2). XRD analysis further confirmed the presence of well-crystallized vivianite (Figs 5.11B and 5.11C), and this consists with the high O signals in the EDX spectra (Fig 5.12). EDX scanning in selected areas (Fig 5.13) revealed that vivianite had aggregated into large crystals taking a slab or a bullet shape from the H+P and F+P bottles, respectively.

Vivianite is rapidly formed when free ferrous and phosphate ions are present at near-neutral pH[361, 362]. Previous research[345, 363, 364] revealed that free sulfide inhibited vivianite formation, but FeS precipitation and Fe(III) (Hydr)oxide reductions scavenged sulfide and thus cleared the inhibitive effect in all our experiments. Completion of pyruvate fermentation led to a build-up of soluble Fe^{2+} high enough (5.5 and 4.6 mM in the H-P and F-P bottles, respectively) to exceed the equilibrium threshold determined by the vivianite solubility product and resulted in precipitation. This is confirmed by the modeling calculation presented in Figure 5.14.

5.4.2.5. Mackinawite formation

Mackinawite was clearly present in the solid sample from the bottle with ferrihydrite (F+P; Fig 5.11C) and had a particle thickness (8.2 nm) close to the mackinawite from lactate (8.6 nm; Table 5.1). This was clearly confirmed by the high S:Fe signal ratio in the EDX spectrum of the solids from the G+P bottle (Fig 5.12). For the other two bottles, however, the S:Fe signal ratio was lower (Fig 5.12) because more soluble Fe^{2+} precipitated as vivianite [$Fe_3(PO_4)_2 \cdot 8(H_2O)$], which is discussed above.

Similar to the lactate experiments, it is difficult to infer from the XRD patterns whether mackinawite was present from the bottles with goethite (G+P) and hematite (H+P). In the G+P samples, TEM detected lattice fringes at two nearby locations (Fig 5.15). In the brighter area on the left, the average *d*-spacing value of 3.0±0.5Å may indicate the presence of mackinawite. In the darker area on the right, the average *d*-spacing values (4.2±0.2Å and 2.7±0.1Å) were close to the *d*-spacing values of common goethite (4.18Å and 2.69 Å)[346].

Also similar to lactate, no characteristic peaks of elemental sulfur can be recognized, either because the amount was negligible or the elemental sulfur was in the non-crystalline, amorphous form. Again parallel to the lactate conditions, higher bioavailability of the initial iron source led to higher FeS yield (ferrihydrite > goethite > hematite).

Although many trends were similar for lactate and pyruvate, they gave distinctly different metabolic patterns with *D. vulgaris*. Compared to lactate, pyruvate as the electron donor gave less remaining Fe(III) (hydr)oxides, more accumulation of soluble Fe^{2+}, less production of elemental sulfur, more FeS production, and formation of vivianite (Table 5.2). This indicates a more active enzymatic reductions of Fe(III) (hydr)oxides with pyruvate due to the faster and complete utilization of pyruvate by *D. vulgaris*, and states significant difference of metabolism patterns when *D. vulgairs* utilized pyruvate from utilizing lactate.

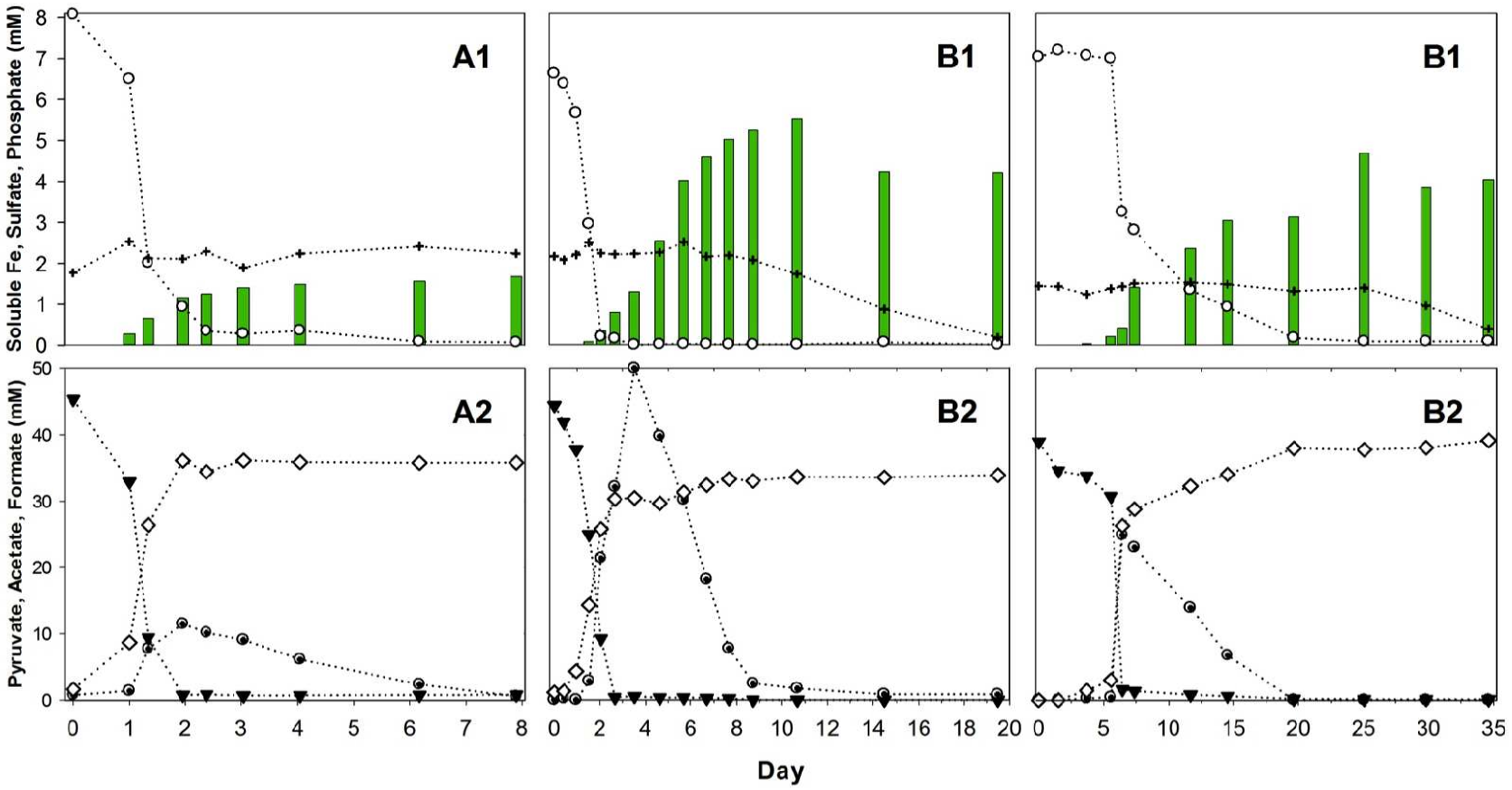


Fig 5.10 Concentrations of soluble Fe(II) (bars), sulfate (○), phosphate (□), pyruvate (▼), acetate (◇), and formate (⊙) during the growth of *D. vulgaris* with pyruvate as the electron donor plus goethite (α-FeOOH, A1 and A2), hematite (α-Fe_2O_3, B1 and B2), or ferrihydrite ($Fe_2O_3 \cdot 0.5H_2O$, C1 and C2) solids as the solid-phase electron acceptor.

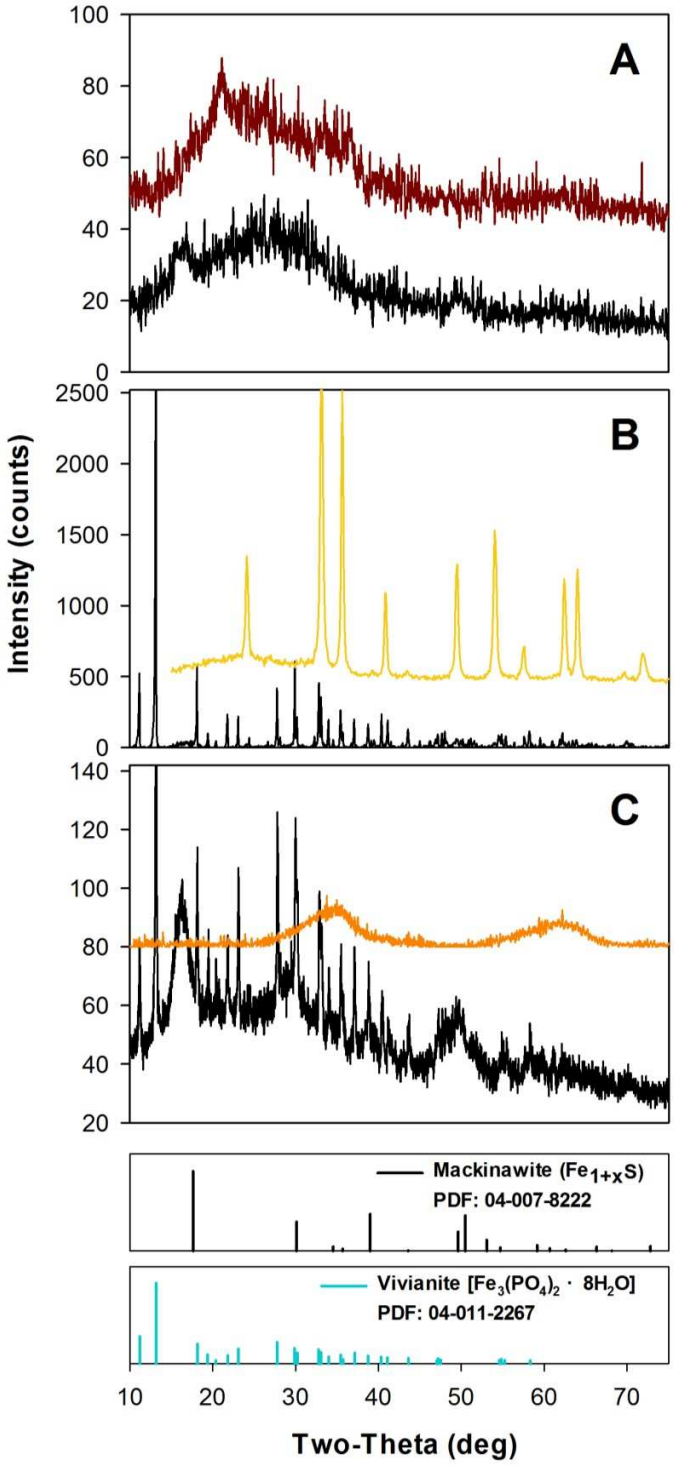


Fig 5.11 XRD spectra of synthetic Fe(III) (hydr)oxides (the top lines) and final solid products (the bottom lines) with pyruvate as the electron donor plus goethite (α-FeOOH, A), hematite (α-Fe_2O_3, B), or ferrihydrite (Fe_2O_3·0.5H_2O, C) solids as the solid-phase electron acceptor.

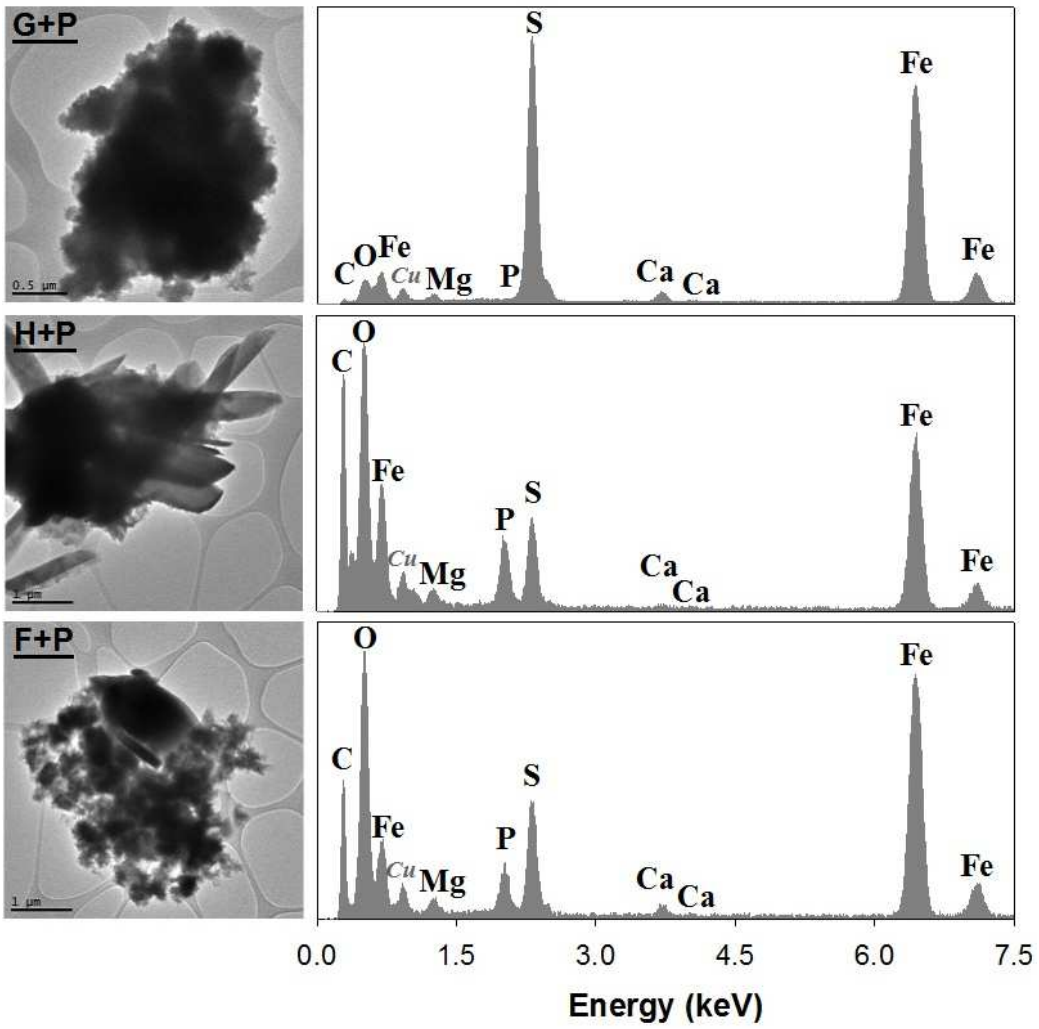


Fig 5.12 TEM images (left column) and EDX spectra (right column) of solids separated from media with goethite plus pyruvate (G+P), hematite plus pyruvate (H+P), and 2-line ferrihydrite plus pyruvate (F+P).

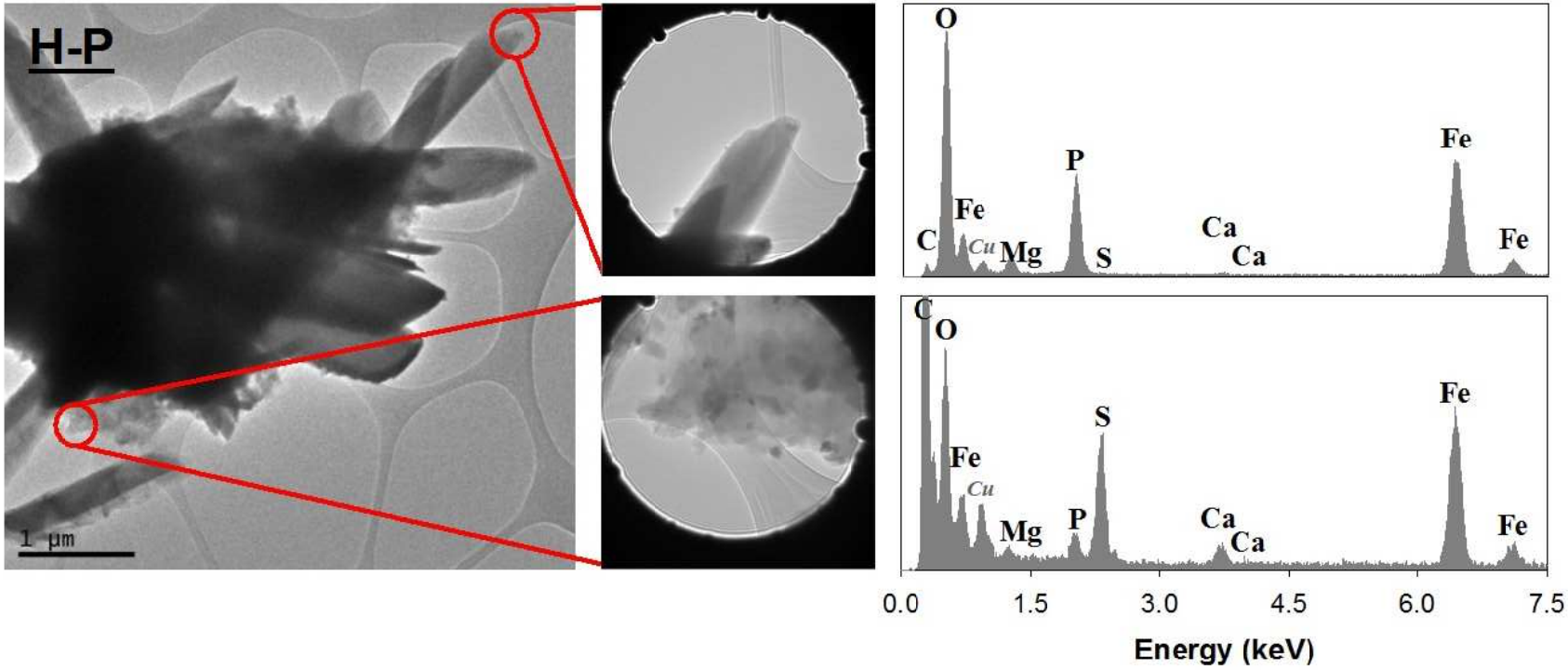


Fig 5.13 The TEM images and the comprehensive EDX results of two spots in the solids produced from the bottle with hematite plus pyruvate. The strong Fe and P signals but invisible S signal in the upper area indicates that the large slab-shpaed crystals in µm level was vivianite, while the strong Fe and S signals in the lower area indicates that FeS solids mainly accumulated at the edge of vivianite clumps.

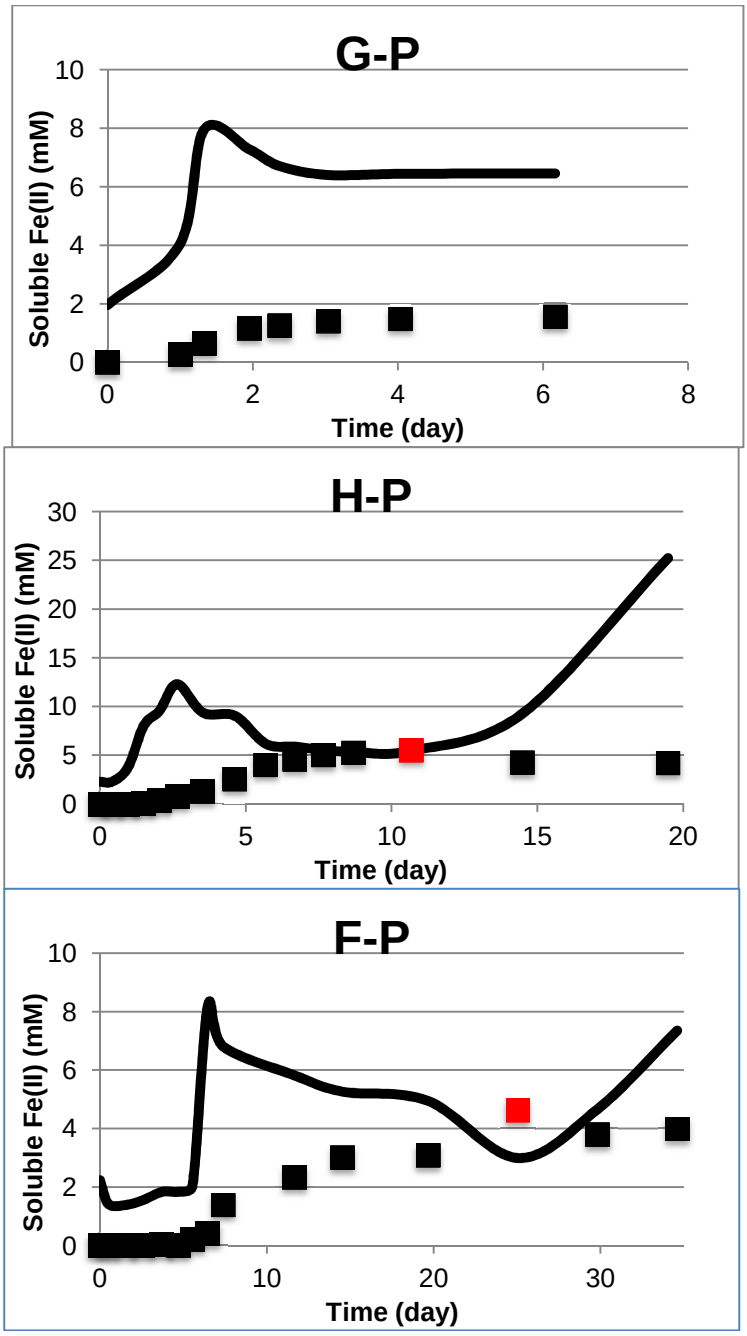


Figure 5.14. Solid lines: the simulated mimimum soluble Fe(II) concentration allowing vivianite precipitation given the actual phosphate concentration and pH value in the G-P, H-P, and F-P bottles featuring 0.3 M inonic strength; Square dots: the actual soluble Fe(II) concentration in the G-P, H-P, and F-P bottles. The red dots represent the actual soluble Fe(II) concentrations above the simulated thresholds and thus causing vivianite formation.

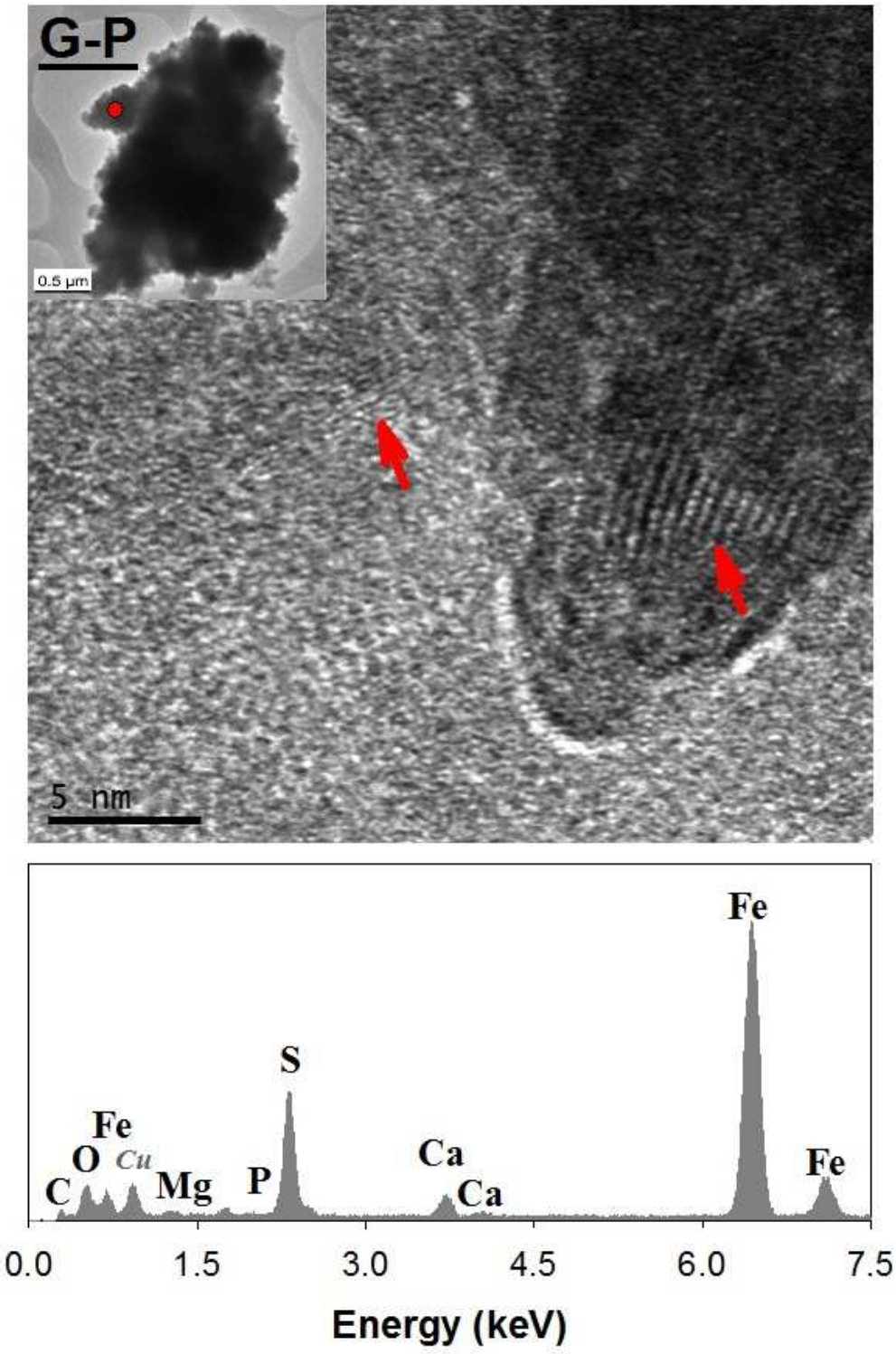


Fig 5.15 The TEM image and the EDX spectrum of a nm-level spot showing crystal lattices in the solids from bottle with goethite plus pyruvate (G-P). The red dot indicates the selected area for EDX scanning, and two red arrows indicate two different lattice fringes.

5.5. Summary

Different iron sources and electron donors significantly affected the extent of reaction and FeS characteristics by *D. vulgaris*. With lactate as the electron donor, *D. vulgaris* exclusively reduced soluble Fe^{3+} enzymatically, and Fe^{3+} was reduced before sulfate when soluble Fe^{3+} was readily available. Fe(III) (hydr)oxide reductions were slower than sulfate reduction and did not go to completion despite electron-donor overdosing. Because of the relatively slow rate of Fe(III) (hydr)oxide reduction, *D. vulgaris* concurrently reduced Fe(III) (hydr)oxides enzymatically (based on lactate oxidation) and chemically via the biogenic sulfide derived from sulfate reduction. *D. vulgaris* produced mackinawite with soluble Fe or solid-phase ferrihydrite, but the mackinawite derived from soluble Fe^{2+} was more crystalline than the mackinawite derived from reducing soluble Fe^{3+} or ferrihydrite solids. The greater crystallinity and size with soluble Fe^{2+} were direct results of the faster formation rate of FeS solids.

Pyruvate significantly enhanced the growth and metabolism of the bacteria, compared to lactate, due to its faster oxidation kinetics. The higher utilization rate of pyruvate allowed concomitant reductions of sulfate and Fe(III), while sulfate reduction could not begin until the more favorable Fe(III) reduction was completed with lactate. The greater proton production during pyruvate fermentation lowered pH and hence led to more crystalline mackinawite than from lactate when soluble Fe^{2+} or Fe^{3+} was the iron source. Pyruvate fermentation apparently produced formate preferably over H_2, thus enabling the complete pyruvate consumption even when no electron acceptor was present. As a result, more Fe(III) (hydr)oxides was reduced and more FeS solids were produced with pyruvate than under lactate conditions. However, a possible drawback of the fast Fe(III) reduction was the unexpected formation of vivianite due to greater accumulation of soluble Fe^{2+}.

CHAPTER 6. Summary

6.1. Summary of results

Uranium has been utilized for weapon manufacturing and energy generation over the past century. As a consequence, U is widely present in aquifers and soils at over 120 DOE sites in the U.S., and it threatens human health due to its strong toxicity. The overall goal of my PhD research is to understand the roles of SRB - the *Desulfovibrio vulgaris* species being a representative - on uranium bioremediation, as well as to investigate the relationships among environmental conditions, SRB activities, and geochemical characteristics of biogenic precipitates during short-term and long-term U sequestration.

In Chapter 1, I presented an overview of the literature on uranium contamination and bioremediation. I also summarized the fundamentals of uranium immobilization/remobilization, introduced the novel MBfR technology with potential application on U(VI) reduction, and pointed out the significance and advantage to studying the versatile role of SRB on uranium bioremediation by 1) directly inducing U immobilization in both enzymatic and chemical way and by 2) indirectly protecting U remobilization using biogenic FeS as the metabolic product.

In Chapter 2, I detailed batch studies on U(VI) bioreduction and reported how the reduction patterns and uraninite crystallinities are influenced by sulfate and iron. *D. vulgaris* was able to grow through respiration of U(VI) alone and produced nanocrystallite uraninite (UO_2). Compared to synthetic UO_2, biogenic UO_2 by *D. vulgaris* featured smaller size, higher static disorder, and about 20 mg/g associated biomass. In addition, the patterns of U(VI) reduction and UO_2 production by *D. vulgaris* were distinguishable in presence versus absence of sulfate and Fe(II). When sulfate was present, *D. vulgaris* reduced both electron acceptor concomitantly, and the biogenic sulfide accelerated the overall U(VI) loss by abiotically reducing U(VI); this process, however, did not take place in presence of soluble Fe(II), because Fe(II) rapidly scavenged sulfide by forming FeS precipitates. The presence of Fe(II) probably also inhibited crystallization of biogenic UO_2 and FeS.

In Chapter 3, I introduced the bench-scale MBfR system inoculated with a *D. vulgaris* suspension for U(VI) removal, a collaborative effort with Aura Ontiveros, a PhD student in our research group. We successfully achieved and maintained 94-95% U(VI) removal at steady state in the MBfR during over 8 months of operation, and we discovered that 1) an extended startup was necessary in order to allow slow-growing U(VI) reducers to form biofilms; 2) The system was capable of self-recovery after an intensive disturbance due to oxygen exposure; 3) crystalline UO_2 aggregates and amorphous U precipitates were associated with vegetative cells and mature spores accumulated in the biofilm matrix; 4) sulfate was not reduced, and *D. vulgaris* was not present in the U(VI)-reducing biofilm; and 5) the most abundant group in the biofilm community contained U(VI) reducers in the *Rhodocyclaceae* family when U(VI) was the only electron acceptor, and it dramatically shift to the *Clostridiaceae* family that included U(VI)-reducing spores after sulfate was added.

In Chapters 4 and 5, I detailed the production of biogenic FeS of different characteristics using various environmental conditions and iron sources. My studies revealed that pH, free sulfide concentration, iron species, and electron donor affected *D. vulgaris* growth and consequent FeS production, and the potential usefulness of the FeS to protect against U remobilization. The pH determined the characteristics of biogenic FeS, and SRB metabolism of different donors systematically altered the ambient pH. A lower pH, due to its initial value or net production of acid, greatly enhanced particle growth of mackinawite. Greater accumulation of free sulfide from enhanced sulfate bioreduction stimulated mackinawite production and its transformation to greigite.

Distinctly different patterns of lactate and pyruvate utilization significantly affected the amount and type of FeS solids, as well as the generation of other solids. Lactate fermentation was inhibited once sulfate reduction was completed due to a small accumulation of H_2, while pyruvate was completely fermented because electrons were diverted from H_2 to formate. As a result, *D. vulgaris* produced limited amounts of FeS when lactate was the fermentable substrate, but was able to convert over 97% Fe(III) (hydr)oxides to FeS. Overall, microbiology-relevant

conditions can be tools to generate biogenic FeS solids of different characteristics that could affect the FeS activity in buffering UO_2 remoblization in potential.

In summary, my research provides a baseline for exploiting effective and sustainable approaches in U bioremediation, including the application of biogenic FeS for protecting remobilization of sequestrated U, and the novel MBfR technology to U sequestration from groundwater, and microbe-relevant tools to optimize U sequestration in either setting.

6.2. Future research

Further collaborative and interdisciplinary research with other groups in ASU and other universities is an absolute necessity to investigate and characterize interactional behaviors of U and microorganisms in more depth either in nature or in laboratory, as well as to optimize technology for in situ or *ex situ* remediation and terminal treatment in larger scale. Immediately, I will continue the collaboration with the UofM team for further investigation on protecting sequestrated U from remobilization. We are looking forward to a series of tests investigating how the various characteristics of biogenic FeS - including crystalline size, geochemically-associated biomass, and dosages – affect its buffer capacity for both synthetic and biogenic UO_2.

I also am now conducting batch tests on physical-chemical adsorption and enzymatic reduction of U(VI) by cell-free EPS. EPS is a substantial component of all biofilm systems, including the MBfR, but its contribution to U sequestration and the underlying mechanisms are minimally understood. This is a collaborative project with two other students in ASU, Xiaoyin Xu and Zhuolin Liu, as well as a research group supervised by Dr. Ang Li in Harbin Institute of Technology, China.

In addition, I am scheduling a new MBfR experiment with more “real world” conditions. I will inoculate the reactor with microorganisms in the activated sludge from the Mesa WWTP and feed the reactor with synthetic U-contaminated groundwater featuring a low U concentration, high sulfate and nitrate concentrations, and high hardness. I expect to explore the versatility of the MBfR system in U treatment and the influence of unfavorable conditions on the performance of U sequestration and on the structure of microbial community.

Looking at the larger picture, I recommend a series of research efforts on 1) optimizing *in situ* (bioaugmentation) and *ex situ* (full-scale MBfR systems) for long-term sequestration and recovery of U from the contaminated groundwater and 2) maximizing the recyclability of the recovered U for sustainable exploitation of U resources. Both can build upon the foundation laid by my research and can lead to practical benefits.

REFERENCES

1. McGraw-Hill, Uranium. In *McGraw-Hill Concise Encyclopedia of Science & Technology*, 5th ed.; McGraw-Hill Book Company: New York, USA, 2004.

2. Taylor, D. M.; Taylor, S. K., Environmental Uranium and Human Health. *Reviews on Environmental Health* **1997,** *12*, (3), 147-157.

3. Hammond, C. R., The Elements. In *CRC handbook of chemistry and physics*, 81th ed.; Hynes, W. M., Ed. CRC press LLC: Boca Raton, FL, USA, 2000.

4. Hampel, C. A., The encyclopedia of the chemical elements. In Reinhold Book Corp.: New York,, 1968; pp viii, 849.

5. Seaborg, G. T., Uranium. In *The Encyclopedia of the Chemical Elements*, Reinhold Book Corporation: Skokie, IL, 1968; pp 773-786.

6. Sandino, A.; Bruno, J., The Solubility of $(UO_2)_3(PO_4)_2 \cdot 4H_2O_{(S)}$ and the Formation of U(Vi) Phosphate Complexes: Their Influence in Uranium Speciation in Natural Waters. *Geochim Cosmochim Ac* **1992,** *56*, (12), 4135-4145.

7. Gavrilescu, M.; Pavel, L. V.; Cretescu, I., Characterization and remediation of soils contaminated with uranium. *J Hazard Mater* **2009,** *163*, 475-510.

8. Kim, J. J., Chemical behavior of transuranic elements in aquatic systems. In *Handbook on the Physics and Chemistryof the Actinides*, Freeman, A. J.; Keller, C., Eds. Elsevier Science Publishers: Amsterdam, Holland, 1986; pp 413-455.

9. Lenhart, J. J.; Cabaniss, S. E.; MacCarthy, P.; Honeyman, B. D., Uranium(VI) complexation with citric, humic and fulvic acids. *Radiochim Acta* **2000,** *88*, (6), 345-353.

10. Shanbhag, P. M.; Choppin, G. R., Binding of Uranyl by Humic Acid. *J Inorg Nucl Chem* **1981,** *43*, (12), 3369-3372.

11. Dozol, M.; Hagemann, R.; Hoffman, D. C.; Adloff, J. P.; Vongunten, H. R.; Foos, J.; Kasprzak, K. S.; Liu, Y. F.; Zvara, I.; Ache, H. J.; Das, H. A.; Hagemann, R. J. C.; Herrmann, G.; Karol, P.; Maenhaut, W.; Nakahara, H.; Sakanoue, M.; Tetlow, J. A.; Baro, G. B.; Fardy, J. J.; Benes, P.; Roessler, K.; Roth, E.; Burger, K.; Steinnes, E.; Kostanski, M. J.; Peisach, M.; Liljenzin, J. O.; Aras, N. K.; Myasoedov, B. F.; Holden, N. E., Radionuclide Migration in Groundwaters: Review of the Behavior of Actinides (Technical Report). *Pure Appl Chem* **1993,** *65*, (5), 1081-1102.

12. Brendler, V.; Geipel, G.; Bernhard, G.; Nitsche, H., Possible impacts of phosphate influx on the uranium speciation and migration in seepage waters. In *Proceedings of theInternational*

Conference Workshop on Uranium Mining and Hydrogeology, Merkel, B.; Hurst, S.; Löhnert, E. P.; Struckmeier, W., Eds. Verlag Sven von Loga: Köln, Germany, 1995.

13. Gupta, D. C.; Singh, H., Uranium resource procecessing: secondary resources, developments in uranium resources, production, demand and the environment. In *Proceedings of a Technical Committee Meeting*, Vienna, Austria, 2005.

14. Ikeda, A.; Hennig, C.; Tsushima, S.; Takao, K.; Ikeda, Y.; Scheinost, A. C.; Bernhard, G., Comparative study of U(VI) and U(V) carbonate complexes in an aqueous solution. *Inorganic Chemistry* **2007,** *46*, (10), 4212-4219.

15. Bernhard, G.; Geipel, G.; Brendler, V.; Nitsche, H., Speciation of uranium in seepage waters of a mine tailing pile studied by time-resolved laser-induced fluorescence spectroscopy (TRLFS). *Radiochim Acta* **1996,** *74*, 87-91.

16. Bernhard, G.; Geipel, G.; Reich, T.; Brendler, V.; Amayri, S.; Nitsche, H., Uranyl(VI) carbonate complex formation: Validation of the $Ca_2UO_2(CO_3)_{3\,(aq.)}$ species. *Radiochim Acta* **2001,** *89*, (8), 511-518.

17. Kalmykov, S. N.; Choppin, G. R., Mixed Ca2+/UO22+/CO32- complex formation at different ionic strengths. *Radiochim Acta* **2000,** *88*, (9-11), 603-606.

18. Gorman-Lewis, D.; Elias, P. E.; Fein, J. B., Adsorption of aqueous uranyl complexes onto Bacillus subtilis cells. *Environ Sci Technol* **2005,** *39*, (13), 4906-4912.

19. Merroun, M. L.; Selenska-Pobell, S., Bacterial interactions with uranium: An environmental perspective. *J Contam Hydrol* **2008,** *102*, (3-4), 285-295.

20. Arogonne National Laboratory, E., DOE Uranium. http://www.evs.anl.gov/pub/doc/Uranium.pdf

21. Emsley, J., *Nature's Building Blocks: An A to Z Guide to the Elements*. Oxford University Press: New York, USA, 2001.

22. Arfsten, D. P.; Still, K. R.; Ritchie, G. D., A review of the effects of uranium and depleted uranium exposure on reproduction and fetal developmentt. *Toxicol Ind Health* **2001,** *17*, (5-10), 180-191.

23. Brugge, D.; de Lemos, J. L.; Oldmixon, B., Exposure Pathways and Health Effects Associated with Chemical and Radiological Toxicity of Natural Uranium: A Review. *Reviews on Environmental Health* **2005,** *20*, (3), 177-193.

24. Wall, J. D.; Krumholz, L. R., Uranium Reduction. *Annu Rev Microbiol* **2006,** *60*, 149-166.

25. NABIR, Bioremediation of metals and radionuclides. What is it and how it works. *Rep.LBNL-42595* **2003**.

26. Krane, K. S., *Introductory Nuclear Physics*. John Wiley & Sons: 1988.

27. McDiarmid, M. A., Depleted uranium and public health - Fifty years' study of occupational exposure provides little evidence of cancer. *Brit Med J* **2001,** *322*, (7279), 123-124.

28. Miller, A. C.; McClain, D., A Review of Depleted Uranium Biological Effects: In Vitro and In Vivo Studies. *Reviews on Environmental Health* **2007,** *22*, (1), 75-89.

29. Bleise, A.; Danesi, P. R.; Burkart, W., Properties, use and health effects of depleted uranium (DU): a general overview. *J Environ Radioactiv* **2003,** *64*, (2-3), 93-112.

30. (AEPI)., A. E. P. I. *Health and environmental consequence s of depleted uranium use in the U.S. Army*; U.S. Army Environmental Policy Institute: Technical Report, 1995.

31. Priest, N. D., Toxicity of depleted uranium. *Lancet* **2001,** *357*, (9252), 244-246.

32. Miller, A. C.; Stewart, M.; Brooks, K.; Shi, L.; Page, N., Depleted uranium-catalyzed oxidative DNA damage: absence of significant alpha particle decay. *J Inorg Biochem* **2002,** *91*, (1), 246-252.

33. Cothern, C. R.; Lappenbusch, W. L., Occurrence of Uranium in Drinking-Water in the United States. *Health Phys* **1983,** *45*, (1), 89-99.

34. Latouche, Y. D.; Willis, D. L.; Dawydiak, O. I., Absorption and Biokinetics of U in Rats Following an Oral-Administration of Uranyl-Nitrate Solution. *Health Phys* **1987,** *53*, (2), 147-162.

35. Skipton, S. O. Drinking water: Uranium. http://www.ianrpubs.unl.edu/live/g1569/build/g1569.pdf

36. Harley, N. H.; Foulkes, E. C.; Hilborne, L. H.; Hudson, A.; Anthony, C. R. *A review of the scientific literature as it pertains to Gulf war illnesses, Vol. 7: Depleted Uranium*; Corporation National Defense Research Institute: Washington, USA, 1999.

37. A. A. f. T. S. a. D. *Toxicological Profile for Uranium*; US Public Health Service, Department of Health & Human Services.: Atlanta, GA, USA, 1999.

38. Kurttio, P.; Komulainen, H.; Leino, A.; Salonen, L.; Auvinen, A.; Saha, H., Bone as a Possible Target of Chemical Toxicity of Natural Uranium in Drinking Water. *Environ Health Persp* **2005,** *113*, (1), 68-72.

39. Zamora, M. L.; Tracy, B. L.; Zielinski, J. M.; Meyerhof, D. P.; Moss, M. A., Chronic ingestion of uranium in drinking water: A study of kidney bioeffects in humans. *Toxicol Sci* **1998,** *43*, (1), 68-77.

40. Kurttio, P.; Harmoinen, A.; Saha, H.; Salonen, L.; Karpas, Z.; Komulainen, H.; Auvinen, A., Kidney toxicity of ingested uranium from drinking water. *Am J Kidney Dis* **2006,** *47*, (6), 972-982.

41. Kurttio, P.; Auvinen, A.; Salonen, L.; Saha, H.; Pekkanen, J.; Makelainen, I.; Vaisanen, S. B.; Penttila, I. M.; Komulainen, H., Renal effects of uranium in drinking water. *Environ Health Persp* **2002,** *110*, (4), 337-342.

42. Carriere, M.; Avoscan, L.; Collins, R.; Carrot, F.; Khodja, H.; Ansoborlo, E.; Gouget, B., Influence of uranium speciation on normal rat kidney (NRK-52E) proximal cell cytotoxicity. *Chem Res Toxicol* **2004,** *17*, (3), 446-452.

43. Linares, V.; Belles, M.; Albina, M. L.; Sirvent, J. J.; Sanchez, D. J.; Domingo, J. L., Assessment of the pro-oxidant activity of uranium in kidney and testis of rats. *Toxicol Lett* **2006,** *167*, (2), 152-161.

44. Peters, P. W.; Garbls-Berkvens, J. M., Study Unit 31: General reproductive toxicology. In *Toxicology: principles and applications*, Niesink, R. J. M.; de Vries, J.; Hollinger, M. A., Eds. CRC Press: Boca Raton, FL, USA, 1996; p 937.

45. Arfsten, D. P.; Still, K. R.; Ritchie, G. D., A review of the effects of uranium and depleted uranium exposure on reproduction and fetal development. *Toxicol Ind Health* **2001,** *17*, (5-10), 180-191.

46. Domingo, J. L., Reproductive and developmental toxicity of natural and depleted uranium: a review. *Reprod Toxicol* **2001,** *15*, (6), 603-609.

47. Linares, V.; Albina, M. L.; Belles, M.; Mayayo, E.; Sanehez, D. J.; Domingo, J. L., Combined action of uranium and stress in the rat: II. Effects on male reproduction. *Toxicol Lett* **2005,** *158*, (3), 186-195.

48. Llobet, J. M.; Sirvent, J. J.; Ortega, A.; Domingo, J. L., Influence of Chronic Exposure to Uranium on Male Reproduction in Mice. *Fund Appl Toxicol* **1991,** *16*, (4), 821-829.

49. Angenard, G.; Muczynski, V.; Coffigny, H.; Duquenne, C.; Frydman, R.; Habert, R.; Livera, G.; Rouiller-Fabre, V., In vitro effects of Uranium on human fetal germ cells. *Reprod Toxicol* **2011,** *31*, (4), 470-476.

50. Arfsten, D. P.; Still, K. R.; Wilfong, E. R.; Johnson, E. W.; McInturf, S. M.; Eggers, J. S.; Schaeffer, D. J.; Bekkedal, M. Y. V., Two-Generation Reproductive Toxicity Study of Implanted Depleted Uranium (DU) in CD Rats. *J Toxicol Env Heal A* **2009,** *72*, (6), 410-427.

51. (WHO), W. H. O., Guidelines for Drinking Water Quality. In *Health Criteria and other Supporting Information*, 2nd ed.; WHO: Geneva, Switzerland, 1998.

52. EPA Basic Information about Radionuclides in Drinking Water.

53. Baca, T. E.; Florkowski, T., *The environmental challenges of nuclear disarmament*. Kluwer Academic: Dordrecht Netherlands ; Boston, 2000; p xi, 354.

54. Baird, C.; Cann, M., *Environmental Chemistry*. 3rd ed.; University of Western Ontario: London, Ontario, Canada, 2005.

55. Brümmer, G.; Gerth, J.; Herms, U., Heavy metal species, mobility and availability in soils. *Pflanzenernaehr. Bodenkd* **1986,** *149*, (382-298).

56. Langmuir, D., Uranium Solution-Mineral Equilibria at Low-Temperatures with Applications to Sedimentary Ore-Deposits. *Geochim Cosmochim Ac* **1978,** *42*, (6), 547-569.

57. Krepelova, A.; Sachs, S.; Bernhard, G., Uranium(VI) sorption onto kaolinite in the presence and absence of humic acid. *Radiochim Acta* **2006,** *94*, (12), 825-833.

58. Payne, T. E.; Lumpkin, G. R.; Waite, T. D., Uranium(VI) adsorption on model minerals. In *Adsorption of Metals by Geomedia: Variables, Mechanisms, and Model Applications*, Jenne, E., Ed. Academic Press: Waltham, MA, USA, 1998.

59. Lenhart, J. J.; Honeyman, B. D., Uranium(VI) sorption to hematite in the presence of humic acid. *Geochim Cosmochim Ac* **1999,** *63*, (19-20), 2891-2901.

60. Aytas, S. M.; Akyil, S.; Eral, M., Adsorption and thermodynamic behavior of uranium on natural zeolite. *J Radioanal Nucl Ch* **2004,** *260*, (1), 119-125.

61. Ho, C. H.; Miller, N. H., Effect of Humic-Acid on Uranium Uptake by Hematite Particles. *J Colloid Interf Sci* **1985,** *106*, (2), 281-288.

62. Schmeide, K.; Pompe, S.; Bubner, M.; Heise, K. H.; Bernhard, G.; Nitsche, H., Uranium(VI) sorption onto phyllite and selected minerals in the presence of humic acid. *Radiochim Acta* **2000,** *88*, (9-11), 723-728.

63. Morrison, S. J.; Spangler, R. R.; Tripathi, V. S., Adsorption of Uranium(Vi) on Amorphous Ferric Oxyhydroxide at High-Concentrations of Dissolved Carbon(IV) and Sulfur(VI). *J Contam Hydrol* **1995,** *17*, (4), 333-346.

64. Kilislioglu, A.; Bilgin, B., Adsorption of uranium on halloysite. *Radiochim Acta* **2002,** *90*, (3), 155-160.

65. Duff, M. C.; Amrhein, C., Uranium(VI) adsorption on goethite and soil in carbonate solutions. *Soil Sci Soc Am J* **1996,** *60*, (5), 1393-1400.

66. Moyes, L. N.; Parkman, R. H.; Charnock, J. M.; Vaughan, D. J.; Livens, F. R.; Hughes, C. R.; Braithwaite, A., Uranium uptake from aqueous solution by interaction with goethite, lepidocrocite, muscovite, and mackinawite: An X-ray absorption spectroscopy study. *Environ Sci Technol* **2000,** *34*, (6), 1062-1068.

67. Dong, W. M.; Ball, W. P.; Liu, C. X.; Wang, Z. M.; Stone, A. T.; Bai, J.; Zachara, J. M., Influence of calcite and dissolved calcium on uranium(VI) sorption to a Hanford subsurface sediment. *Environ Sci Technol* **2005,** *39*, (20), 7949-7955.

68. Elzinga, E. J.; Tait, C. D.; Reeder, R. J.; Rector, K. D.; Donohoe, R. J.; Morris, D. E., Spectroscopic investigation of U(VI) sorption at the calcite-water interface. *Geochim Cosmochim Ac* **2004,** *68*, (11), 2437-2448.

69. Reeder, R. J.; Nugent, M.; Tait, C. D.; Morris, D. E.; Heald, S. M.; Beck, K. M.; Hess, W. P.; Lanzirotti, A., Coprecipitation of uranium(VI) with calcite: XAFS, micro-XAS, and luminescence characterization. *Geochim Cosmochim Ac* **2001,** *65*, (20), 3491-3503.

70. Niu, Z. W.; Fan, Q. H.; Wang, W. H.; Xu, J. Z.; Chen, L.; Wu, W. S., Effect of pH, ionic strength and humic acid on the sorption of uranium(VI) to attapulgite. *Appl Radiat Isotopes* **2009,** *67*, (9), 1582-1590.

71. Wersin, P.; Hochella, M. F.; Persson, P.; Redden, G.; Leckie, J. O.; Harris, D. W., Interaction between Aqueous Uranium(VI) and Sulfide Minerals - Spectroscopic Evidence for Sorption and Reduction. *Geochim Cosmochim Ac* **1994,** *58*, (13), 2829-2843.

72. Descostes, M.; Schlegel, M. L.; Eglizaud, N.; Descamps, F.; Miserque, F.; Simoni, E., Uptake of uranium and trace elements in pyrite (FeS2) suspensions. *Geochim Cosmochim Ac* **2010,** *74*, (5), 1551-1562.

73. Benes, P.; Kratzer, K.; Vlckova, S.; Sebestova, E., Adsorption of uranium on clay and the effect of humic substances. *Radiochim Acta* **1998,** *82*, 367-373.

74. Donat, R.; Aytas, S., Adsorption and thermodynamic behavior of uranium(VI) on *Ulva sp*.-Na bentonite composite adsorbent. *J Radioanal Nucl Ch* **2005,** *265*, (1), 107-114.

75. Tsezos, M.; Volesky, B., The Mechanism of Uranium Biosorption by Rhizopus-Arrhizus. *Biotechnol Bioeng* **1982,** *24*, (2), 385-401.

76. Yang, J. B.; Volesky, B., Biosorption of uranium on Sargassum biomass. *Water Res* **1999,** *33*, (15), 3357-3363.

77. Wang, J. S.; Hu, X. J.; Liu, Y. G.; Xie, S. B.; Bao, Z. L., Biosorption of uranium (VI) by immobilized Aspergillus fumigatus beads. *J Environ Radioactiv* **2010,** *101*, (6), 504-508.

78. Bhainsa, K. C.; D'Souza, S. F., Biosorption of uranium(VI) by Aspergillus fumigatus. *Biotechnol Tech* **1999,** *13*, (10), 695-699.

79. Li, P. F.; Mao, Z. Y.; Rao, X. J.; Wang, X. M.; Min, M. Z.; Qiu, L. W.; Liu, Z. L., Biosorption of uranium by lake-harvested biomass from a cyanobacterium bloom. *Bioresource technology* **2004,** *94*, (2), 193-195.

80. Gonzalez-Munoz, M. T.; Merroun, M. L.; Ben Omar, N.; Arias, J. M., Biosorption of uranium by Myxococcus xanthus. *Int Biodeter Biodegr* **1997,** *40*, (2-4), 107-114.

81. Galun, M.; Siegel, S. M.; Cannon, M. I.; Siegel, B. Z.; Galun, E., Ultrastructural-Localization of Uranium Biosorption in Penicillium-Digitatum by Stem X-Ray-Microanalysis. *Environ Pollut* **1987,** *43*, (3), 209-218.

82. Veglio, F.; Beolchini, F., Removal of metals by biosorption: A review. *Hydrometallurgy* **1997,** *44*, (3), 301-316.

83. Rothstein, A.; Meier, R., The Relationship of the Cell Surface to Metabolism. VI. The Chemical Nature of Uranium-Complexing Groups of the Cell Surface. *J Cell Compar Physl* **1951,** *38*, (2), 245-270.

84. Stroes-Gascoyne, S.; Hamon, C. J.; Dixon, D. A.; Martino, J. B., Microbial analysis of samples from the tunnel sealing experiment at AECL's Underground Research Laboratory. *Phys Chem Earth* **2007,** *32*, (1-7), 219-231.

85. Markich, S. J., Uranium speciation and bioavailability in aquatic systems: an overview. *Sci. World* **2002,** *2*, 707-729.

86. Kashefi, K.; Lovley, D. R., Reduction of Fe(III), Mn(IV), and toxic metals at 100 degrees C by Pyrobaculum islandicum. *Appl Environ Microb* **2000,** *66*, (3), 1050-1056.

87. Merroun, M. L.; Raff, J.; Rossberg, A.; Hennig, C.; Reich, T.; Selenska-Pobell, S., Complexation of uranium by cells and S-layer sheets of Bacillus sphaericus JG-A12. *Appl Environ Microb* **2005,** *71*, (9), 5532-5543.

88. Van Roy, S.; Peys, K.; Dresselaers, T.; Diels, L., The use of an Alcaligenes eutrophus biofilm in a membrane bioreactor for heavy metals recovery. *Res. Microbiol.* **1997,** *148*, 526-528.

89. Gu, B.; Liang, L.; Dickey, M. J.; Yin, X.; Dai, S., Reductive precipitation of uranium(VI) by zero-valent iron. *Environ Sci Technol* **1998,** *32*, (21), 3366-3373.

90. Liger, E.; Charlet, L.; Van Cappellen, P., Surface catalysis of uranium(VI) reduction by iron(II). *Geochim Cosmochim Ac* **1999,** *63*, (19-20), 2939-2955.

91. Morrison, S. J.; Metzler, D. R.; Carpenter, C. E., Uranium precipitation in a permeable reactive barrier by progressive irreversible dissolution of zerovalent iron. *Environ Sci Technol* **2001,** *35*, (2), 385-390.

92. Jeon, B. H.; Dempsey, B. A.; Burgos, W. D.; Barnett, M. O.; Roden, E. E., Chemical reduction of U(VI) by Fe(II) at the solid-water interface using natural and synthetic Fe(III) oxides. *Environ Sci Technol* **2005,** *39*, (15), 5642-5649.

93. Scott, T. B.; Allen, G. C.; Heard, P. J.; Randell, M. G., Reduction of U(VI) to U(IV) on the surface of magnetite. *Geochim Cosmochim Ac* **2005,** *69*, (24), 5639-5646.

94. Farrell, J.; Bostick, W. D.; Jarabek, R. J.; Fiedor, J. N., Uranium removal from ground water using zero valent iron media. *Ground Water* **1999,** *37*, (4), 618-624.

95. Latta, D. E.; Boyanov, M. I.; Kemner, K. M.; O'Loughlin, E. J.; Scherer, M. M., Abiotic reduction of uranium by Fe(II) in soil. *Appl Geochem* **2012,** *27*, (8), 1512-1524.

96. Dodge, C. J.; Francis, A. J., Photodegradation of Uranium Citrate Complex with Uranium Recovery. *Environ Sci Technol* **1994,** *28*, (7), 1300-1306.

97. Dodge, C. J.; Francis, A. J., Photodegradation of a ternary iron(III)-uranium(VI)-citric acid complex. *Environ Sci Technol* **2002,** *36*, (9), 2094-2100.

98. Abdelouas, A.; Lu, Y. M.; Lutze, W.; Nuttall, H. E., Reduction of U(VI) to U(IV) by indigenous bacteria in contaminated ground water. *J Contam Hydrol* **1998,** *35*, (1-3), 217-233.

99. Lloyd, J. R.; Macaskie, L. E., Bioremediation of radioactive metals. In *Environmental Microbe–Metal Interactions*, Lovley, D. R., Ed. ASM Press: Washington, DC, USA, 2000; pp 277–327.

100. Gavrilescu, M.; Pavel, L. V.; Cretescu, I., Characterization and remediation of soils contaminated with uranium. *J Hazard Mater* **2009,** *163*, (2-3), 475-510.

101. Sanford, R. A.; Wu, Q.; Sung, Y.; Thomas, S. H.; Amos, B. K.; Prince, E. K.; Loffler, F. E., Hexavalent uranium supports growth of *Anaeromyxobacter dehalogenans* and *Geobacter* spp. with lower than predicted biomass yields. *Environ Microbiol* **2007,** *9*, (11), 2885-2893.

102. Wu, Q.; Sanford, R. A.; Loffler, F. E., Uranium(VI) reduction by *Anaeromyxobacter dehalogenans* strain 2CP-C. *Appl Environ Microb* **2006,** *72*, (5), 3608-3614.

103. Francis, A. J.; Dodge, C. J.; Lu, F. L.; Halada, G. P.; Clayton, C. R., XPS and XANES Studies of Uranium Reduction by *Clostridium* sp. *Environ Sci Technol* **1994,** *28*, (4), 636-639.

104. Gao, W. M.; Francis, A. J., Reduction of uranium(VI) to uranium(IV) by Clostridia. *Appl Environ Microb* **2008,** *74*, (14), 4580-4584.

105. Madden, A. S.; Smith, A. C.; Balkwill, D. L.; Fagan, L. A.; Phelps, T. J., Microbial uranium immobilization independent of nitrate reduction. *Environ Microbiol* **2007,** *9*, (9), 2321-2330.

106. Appukuttan, D.; Rao, A. S.; Apte, S. K., Engineering of *Deinococcus radiodurans* R1 for bioprecipitation of uranium from dilute nuclear waste. *Appl Environ Microb* **2006,** *72*, (12), 7873-7878.

107. Fredrickson, J. K.; Kostandarithes, H. M.; Li, S. W.; Plymale, A. E.; Daly, M. J., Reduction of Fe(III), Cr(VI), U(VI), and Tc(VII) by *Deinococcus radiodurans* R1. *Appl Environ Microb* **2000,** *66*, (5), 2006-2011.

108. Lovley, D. R.; Roden, E. E.; Phillips, E. J. P.; Woodward, J. C., Enzymatic Iron and Uranium Reduction by Sulfate-Reducing Bacteria. *Mar Geol* **1993,** *113*, (1-2), 41-53.

109. Tebo, B. M.; Obraztsova, A. Y. F. M. L., Sulfate-reducing bacterium grows with Cr(VI), U(VI), Mn(IV), and Fe(III) as electron acceptors. *FEMS Microbiology Letters* **1998,** *162*, 193-198.

110. Pilar Junier, P.; Suvorova, E. I.; Bernier-Latmani, R., Effect of Competing Electron Acceptors on the Reduction of U(VI) by *Desulfotomaculum reducens*. *Geomicrobiol J* **2010,** *27*, (5), 435-443.

111. Junier, P.; Frutschi, M.; Wigginton, N. S.; Dalla Vecchia, E.; Sharp, J. O.; Suvorova, E.; Schofield, E.; Bargar, J. R.; Bernier-Latmani, R., U(VI) reduction by *Desulfotomaculum reducens* MI-1. *Geochim Cosmochim Ac* **2009,** *73*, (13), A610-A610.

112. Suzuki, Y.; Kelly, S. D.; Kemner, K. M.; Banfield, J. F., Enzymatic U(VI) reduction by *Desulfosporosinus* species. *Radiochim Acta* **2004,** *92*, (1), 11-16.

113. Lovley, D. R.; Phillips, E. J., Reduction of uranium by *Desulfovibrio desulfuricans*. *Appl Environ Microbiol* **1992,** *58*, (3), 850-6.

114. Tucker, M. D.; Barton, L. L.; Thomson, B. M., Kinetic coefficients for simultaneous reduction of sulfate and uranium by *Desulfovibrio desulfuricans*. *Appl Microbiol Biot* **1996,** *46*, (1), 74-77.

115. Tucker, M. D.; Barton, L. L.; Thomson, B. M., Reduction of Cr, Mo, Se and U by *Desulfovibrio desulfuricans* immobilized in polyacrylamide gels. *J Ind Microbiol Biot* **1998,** *20*, (1), 13-19.

116. Ganesh, R.; Robinson, K. G.; Chu, L. L.; Kucsmas, D.; Reed, G. D., Reductive precipitation of uranium by *Desulfovibrio desulfuricans*: Evaluation of cocontaminant effects and selective removal. *Water Res* **1999,** *33*, (16), 3447-3458.

117. Payne, R. B.; Gentry, D. A.; Rapp-Giles, B. J.; Casalot, L.; Wall, J. D., Uranium reduction by *Desulfovibrio desulfuricans* strain G20 and a cytochrome C_3 mutant. *Appl Environ Microb* **2002,** *68*, (6), 3129-3132.

118. Payne, R. B.; Casalot, L.; Rivere, T.; Terry, J. H.; Larsen, L.; Giles, B. J.; Wall, J. D., Interaction between uranium and the Cytochrome C_3 of *Desulfovibrio desulfuricans* strain G20. *Arch Microbiol* **2004,** *181*, (6), 398-406.

119. Sani, R. K.; Peyton, B. M.; Dohnalkova, A., Toxic effects of uranium on *Desulfovibrio desulfuricans* G20. *Environ Toxicol Chem* **2006,** *25*, (5), 1231-1238.

120. Lovley, D. R.; Widman, P. K.; Woodward, J. C.; Phillips, E. J. P., Reduction of Uranium by Cytochrome C_3 of *Desulfovibrio vulgaris*. *Appl Environ Microb* **1993,** *59*, (11), 3572-3576.

121. Elias, D. A.; Suflita, J. M.; McInerney, M. J.; Krumholz, L. R., Periplasmic cytochrome C_3 of *Desulfovibrio vulgaris* is directly involved in H2-mediated metal but not sulfate reduction. *Appl Environ Microb* **2004,** *70*, (1), 413-420.

122. Lovley, D. R.; Phillips, E. J. P.; Gorby, Y. A.; Landa, E. R., Microbial Reduction of Uranium. *Nature* **1991,** *350*, (6317), 413-416.

123. Lovley, D. R.; Giovannoni, S. J.; White, D. C.; Champine, J. E.; Phillips, E. J. P.; Gorby, Y. A.; Goodwin, S., Geobacter-Metallireducens Gen-Nov Sp-Nov, a Microorganism Capable of Coupling the Complete Oxidation of Organic-Compounds to the Reduction of Iron and Other Metals. *Arch Microbiol* **1993,** *159*, (4), 336-344.

124. Jeon, B. H.; Kelly, S. D.; Kemner, K. M.; Barnett, M. O.; Burgos, W. D.; Dempsey, B. A.; Roden, E. E., Microbial reduction of U(VI) at the solid-water interface. *Environ Sci Technol* **2004,** *38*, (21), 5649-5655.

125. Shelobolina, E. S.; Vrionis, H. A.; Findlay, R. H.; Lovley, D. R., *Geobacter uraniireducens* sp nov., isolated from subsurface sediment undergoing uranium bioremediation. *Int J Syst Evol Micr* **2008,** *58*, 1075-1078.

126. Holmes, D. E.; O'Neil, R. A.; Chavan, M. A.; N'Guessan, L. A.; Vrionis, H. A.; Perpetua, L. A.; Larrahondo, M. J.; DiDonato, R.; Liu, A.; Lovley, D. R., Transcriptome of *Geobacter uraniireducens* growing in uranium-contaminated subsurface sediments. *Isme J* **2009,** *3*, (2), 216-230.

127. Prakash, O.; Gihring, T. M.; Dalton, D. D.; Chin, K. J.; Green, S. J.; Akob, D. M.; Wanger, G.; Kostka, J. E., *Geobacter daltonii* sp. nov., an Fe(III)- and uranium(VI)-reducing bacterium

isolated from a shallow subsurface exposed to mixed heavy metal and hydrocarbon contamination. *Int J Syst Evol Micr* **2010,** *60*, 546-553.

128. Barton, L. L.; Choudhury, K.; Thomson, B. M.; Steenhoudt, K.; Groffman, A. R., Bacterial reduction of soluble uranium: The first step of in situ immobilization of uranium. *Radioact Waste Manag* **1996,** *20*, (2-3), 141-151.

129. Shelobolina, E. S.; Sullivan, S. A.; O'Neill, K. R.; Nevin, K. P.; Lovley, D. R., Isolation, characterization, and U(VI)-reducing potential of a facultatively anaerobic, acid-resistant bacterium from Low-pH, nitrate- and U(VI)-contaminated subsurface sediment and description of *Salmonella subterranea* sp nov. *Appl Environ Microb* **2004,** *70*, (5), 2959-2965.

130. Caccavo, F.; Blakemore, R. P.; Lovley, D. R., A Hydrogen-Oxidizing, Fe(III)-Reducing Microorganism from the Great Bay Estuary, New-Hampshire. *Appl Environ Microb* **1992,** *58*, (10), 3211-3216.

131. Truex, M. J.; Peyton, B. M.; Valentine, N. B.; Gorby, Y. A., Kinetics of U(VI) reduction by a dissimilatory Fe(III)-reducing bacterium under non-growth conditions. *Biotechnol Bioeng* **1997,** *55*, (3), 490-496.

132. Wielinga, B.; Bostick, B.; Hansel, C. M.; Rosenzweig, R. F.; Fendorf, S., Inhibition of bacterially promoted uranium reduction: Ferric (hydr)oxides as competitive electron acceptors. *Environ Sci Technol* **2000,** *34*, (11), 2190-2195.

133. Lovley, D. R.; Phillips, E. J. P.; Gorby, Y. A.; Landa, E. R., Microbial Reduction of Uranium. *Abstr Pap Am Chem S* **1991,** *202*, 8-GEOC.

134. Fredrickson, J. K.; Zachara, J. M.; Kennedy, D. W.; Liu, C. X.; Duff, M. C.; Hunter, D. B.; Dohnalkova, A., Influence of Mn oxides on the reduction of uranium(VI) by the metal-reducing bacterium *Shewanella putrefaciens*. *Geochim Cosmochim Ac* **2002,** *66*, (18), 3247-3262.

135. Bencheikh-Latmani, R.; Williams, S. M.; Haucke, L.; Criddle, C. S.; Wu, L. Y.; Zhou, J. Z.; Tebo, B. M., Global transcriptional profiling of *Shewanella oneidensis* MR-1 during Cr(VI) and U(VI) reduction. *Appl Environ Microb* **2005,** *71*, (11), 7453-7460.

136. Marshall, M. J.; Beliaev, A. S.; Dohnalkova, A. C.; Kennedy, D. W.; Shi, L.; Wang, Z. M.; Boyanov, M. I.; Lai, B.; Kemner, K. M.; McLean, J. S.; Reed, S. B.; Culley, D. E.; Bailey, V. L.; Simonson, C. J.; Saffarini, D. A.; Romine, M. F.; Zachara, J. M.; Fredrickson, J. K., c-Type cytochrome-dependent formation of U(IV) nanoparticles by *Shewanella oneidensis*. *Plos Biol* **2006,** *4*, (8), 1324-1333.

137. Burgos, W. D.; McDonough, J. T.; Senko, J. M.; Zhang, G. X.; Dohnalkova, A. C.; Kelly, S. D.; Gorby, Y.; Kemner, K. M., Characterization of uraninite nanoparticles produced by *Shewanella oneidensis* MR-1. *Geochim Cosmochim Ac* **2008,** *72*, (20), 4901-4915.

138. Sani, R. K.; Peyton, B. M.; Dohnalkova, A., Comparison of uranium(VI) removal by *Shewanella oneidensis* MR-1 in flow and batch reactors. *Water Res* **2008,** *42*, (12), 2993-3002.

139. Schofield, E. J.; Veeramani, H.; Sharp, J. O.; Suvorova, E.; Bernier-Latmani, R.; Mehta, A.; Stahlman, J.; Webb, S. M.; Clark, D. L.; Conradson, S. D.; Ilton, E. S.; Bargar, J. R., Structure of Biogenic Uraninite Produced by *Shewanella oneidensis* Strain MR-1. *Environ Sci Technol* **2008,** *42*, (21), 7898-7904.

140. Blakeney, M. D.; Moulaei, T.; DiChristina, T. J., Fe(III) reduction activity and cytochrome content of *Shewanella putrefaciens* grown on ten compounds as sole terminal electron acceptor. *Microbiol Res* **2000,** *155*, (2), 87-94.

141. Wade, R.; DiChristina, T. J., Isolation of U(VI) reduction-deficient mutants of *Shewanella putrefaciens*. *FEMS Microbiology Letters* **2000,** *184*, (2), 143-148.

142. Haas, J. R.; Northup, A., Effects of aqueous complexation on reductive precipitation of uranium by *Shewanella putrefaciens*. *Geochem T* **2004,** *5*, (3), 41-48.

143. Woolfolk, C. A.; Whiteley, H. R., Reduction of Inorganic Compounds with Molecular Hydrogen by Micrococcus Lactilyticus: 1. Stoichiometry Compounds of Arsenic, Selenium, Tellurium, Transition and Other Elements. *J Bacteriol* **1962,** *84*, (4), 647-58.

144. Woolfolk, C. A., Reduction of Inorganic Compounds with Molecular Hydrogen by Micrococcus Lactilyticus .2. Stoichiometry with Inorganic Sulfur Compounds. *J Bacteriol* **1962,** *84*, (4), 659-668.

145. Roh, Y.; Liu, S. V.; Li, G. S.; Huang, H. S.; Phelps, T. J.; Zhou, J. Z., Isolation and characterization of metal-reducing Thermoanaerobacter strains from deep subsurface environments of the Piceance Basin, Colorado. *Appl Environ Microb* **2002,** *68*, (12), 6013-6020.

146. Khijniak, T. V.; Slobodkin, A. I.; Coker, V.; Renshaw, J. C.; Livens, F. R.; Bonch-Osmolovskaya, E. A.; Birkeland, N. K.; Medvedeva-Lyalikova, N. N.; Lloyd, J. R., Reduction of uranium(VI) phosphate during growth of the thermophilic bacterium Thermoterrabacterium ferrireducens. *Appl Environ Microb* **2005,** *71*, (10), 6423-6426.

147. Kieft, T. L.; Fredrickson, J. K.; Onstott, T. C.; Gorby, Y. A.; Kostandarithes, H. M.; Bailey, T. J.; Kennedy, D. W.; Li, S. W.; Plymale, A. E.; Spadoni, C. M.; Gray, M. S., Dissimilatory reduction of Fe(III) and other electron acceptors by a Thermus isolate. *Appl Environ Microb* **1999,** *65*, (3), 1214-1221.

148. Cason, E. D.; Piater, L. A.; van Heerden, E., Reduction of U(VI) by the deep subsurface bacterium, Thermus scotoductus SA-01, and the involvement of the ABC transporter protein. *Chemosphere* **2012,** *86*, (6), 572-577.

149. Martins, M.; Faleiro, M. L.; da Costa, A. M. R.; Chaves, S.; Tenreiro, R.; Matos, A. P.; Costa, M. C., Mechanism of uranium (VI) removal by two anaerobic bacterial communities. *J Hazard Mater* **2010,** *184*, (1-3), 89-96.

150. Brim, H.; McFarlan, S. C.; Fredrickson, J. K.; Minton, K. W.; Zhai, M.; Wackett, L. P.; Daly, M. J., Engineering Deinococcus radiodurans for metal remediation in radioactive mixed waste environments. *Nat Biotechnol* **2000,** *18*, (1), 85-90.

151. Lovley, D. R.; Phillips, E. J. P., Bioremediation of Uranium Contamination with Enzymatic Uranium Reduction. *Environ Sci Technol* **1992,** *26*, (11), 2228-2234.

152. Vrionis, H. A.; Anderson, R. T.; Ortiz-Bernad, I.; O'Neill, K. R.; Resch, C. T.; Peacock, A. D.; Dayvault, R.; White, D. C.; Long, P. E.; Lovley, D. R., Microbiological and geochemical heterogeneity in an in situ uranium bioremediation field site. *Appl Environ Microb* **2005,** *71*, (10), 6308-6318.

153. Luo, J.; Weber, F. A.; Cirpka, O. A.; Wu, W. M.; Nyman, J. L.; Carley, J.; Jardine, P. M.; Criddle, C. S.; Kitanidis, P. K., Modeling in-situ uranium(VI) bioreduction by sulfate-reducing bacteria. *J Contam Hydrol* **2007,** *92*, (1-2), 129-148.

154. Lovley, D. R., Bioremediation of Organic and Metal Contaminants with Dissimilatory Metal Reduction. *J Ind Microbiol* **1995,** *14*, (2), 85-93.

155. Beyenal, H.; Sani, R. K.; Peyton, B. M.; Dohnalkova, A. C.; Amonette, J. E.; Lewandowski, Z., Uranium immobilization by sulfate-reducing biofilms. *Environ Sci Technol* **2004,** *38*, (7), 2067-2074.

156. Wan, J. M.; Tokunaga, T. K.; Brodie, E.; Wang, Z. M.; Zheng, Z. P.; Herman, D.; Hazen, T. C.; Firestone, M. K.; Sutton, S. R., Reoxidation of bioreduced uranium under reducing conditions. *Environ Sci Technol* **2005,** *39*, (16), 6162-6169.

157. Kramerschnabel, U.; Bischoff, H.; Xi, R. H.; Marx, G., Solubility Products and Complex-Formation Equilibria in the Systems Uranyl Hydroxide and Uranyl Carbonate at 25-Degrees-C and I = 0.1 M. *Radiochim Acta* **1992,** *56*, (4), 183-188.

158. Meinrath, G.; Kimura, T., Carbonate Complexation of the Uranyl(VI) Ion. *J Alloy Compd* **1993,** *202*, 89-93.

159. Gorman-Lewis, D.; Burns, P. C.; Fein, J. B., Review of uranyl mineral solubility measurements. *J Chem Thermodyn* **2008,** *40*, (3), 335-352.

160. Meinrath, G., Coordination of uranyl(VI) carbonate species in aqueous solutions. *J Radioan Nucl Ch Ar* **1996,** *211*, (2), 349-362.

161. Phillips, E. J. P.; Landa, E. R.; Lovley, D. R., Remediation of Uranium Contaminated Soils with Bicarbonate Extraction and Microbial U(Vi) Reduction. *J Ind Microbiol* **1995,** *14*, (3-4), 203-207.

162. Abdelouas, A.; Lutze, W.; Gong, W. L.; Nuttall, E. H.; Strietelmeier, B. A.; Travis, B. J., Biological reduction of uranium in groundwater and subsurface soil. *Sci Total Environ* **2000,** *250*, (1-3), 21-35.

163. Wu, W.; Gu, B.; Fields, M. W.; Gentile, M.; Kuc, Y.; Yan, H.; Tiquias, S.; Yan, T.; Nyman, J.; Zhou, J.; Jardine, P. M.; Criddle, C. S., Uranium (VI) Reduction by Denitrifying Biomass. *Bioremediation Journal* **2005,** *9*, (1), 49-61.

164. Zheng, Z. P.; Tokunaga, T. K.; Wan, J. M., Influence of calcium carbonate on U(VI) sorption to soils. *Environ Sci Technol* **2003,** *37*, (24), 5603-5608.

165. Stewart, B. D.; Neiss, J.; Fendorf, S., Quantifying constraints imposed by calcium and iron on bacterial reduction of uranium(VI). *J Environ Qual* **2007,** *36*, (2), 363-372.

166. Brooks, S. C.; Fredrickson, J. K.; Carroll, S. L.; Kennedy, D. W.; Zachara, J. M.; Plymale, A. E.; Kelly, S. D.; Kemner, K. M.; Fendorf, S., Inhihition of bacterial U(VI) reduction by calcium. *Environ Sci Technol* **2003,** *37*, (9), 1850-1858.

167. Liu, C. X.; Jeon, B. H.; Zachara, J. M.; Wang, Z. M., Influence of calcium on microbial reduction of solid phase uranium(VI). *Biotechnol Bioeng* **2007,** *97*, (6), 1415-1422.

168. Dispirito, A. A.; Talnagi, J. W.; Tuovinen, O. H., Accumulation and Cellular-Distribution of Uranium in Thiobacillus-Ferrooxidans. *Arch Microbiol* **1983,** *135*, (4), 250-253.

169. Gadd, G. M., Heavy-Metal Accumulation by Bacteria and Other Microorganisms. *Experientia* **1990,** *46*, (8), 834-840.

170. Nyman, J. L.; Wu, H. I.; Gentile, M. E.; Kitanidis, P. K.; Criddle, C. S., Inhibition of a U(VI)-and sulfate-reducing consortia by U(VI). *Environ Sci Technol* **2007,** *41*, (18), 6528-6533.

171. Finneran, K. T.; Housewright, M. E.; Lovley, D. R., Multiple influences of nitrate on uranium solubility during bioremediation of uranium-contaminated subsurface sediments. *Environ Microbiol* **2002,** *4*, (9), 510-516.

172. Elias, D. A.; Krumholz, L. R.; Wong, D.; Long, P. E.; Suflita, J. M., Characterization of microbial activities and U reduction in a shallow aquifer contaminated by uranium mill tailings. *Microbial Ecol* **2003,** *46*, (1), 83-91.

173. Istok, J. D.; Senko, J. M.; Krumholz, L. R.; Watson, D.; Bogle, M. A.; Peacock, A.; Chang, Y. J.; White, D. C., In situ bioreduction of technetium and uranium in a nitrate-contaminated aquifer. *Environ Sci Technol* **2004,** *38*, (2), 468-475.

174. Rabus, R. A. L. F.; Hansen, T.; Widdel, F. R. I. E. D. R. I. C. H., Dissimilatory sulfate-and sulfur-reducing prokaryotes. *The prokaryotes* **2006,** *2*, 659-768.

175. D., L., *Aqueous Environmental Geochemistry*. Prentice Hall: Upper Saddle River, NJ, USA, 1997.

176. Yagi, T.; Maruyama, K., Purification and Properties of Cytochrome C_3 of *Desulfovibrio-Vulgaris*, Miyazaki. *Biochim Biophys Acta* **1971,** *243*, (2), 214-224.

177. Thamdrup, B., Bacterial Manganese and Iron Reduction in Aquatic Sediments. In *Adv Microb Ecol*, 2000; Vol. 16, pp 41-84.

178. Thauer, R. K.; Jungermann, K.; Decker, K., Energy Conservation in Chemotrophic Anaerobic Bacteria. *Bacteriol Rev* **1977,** *41*, (1), 100-180.

179. Bargar, J. R.; Bernier-Latmani, R.; Giammar, D. E.; Tebo, B. M., Biogenic Uraninite Nanoparticles and Their Importance for Uranium Remediation. *Elements* **2008,** *4*, (6), 407-412.

180. Lee, S. Y.; Baik, M. H.; Choi, J. W., Biogenic Formation and Growth of Uraninite (UO_2). *Environ Sci Technol* **2010,** *44*, (22), 8409-8414.

181. Lawson, P. S.; Sterritt, R. M.; Lester, J. N., Factors affecting the removal of metals during activated sludge wastewater treatment. I: the role of mixed liquor biomass. *Arch Environ Con Tox* **1984,** *13*, (4), 391-402.

182. Lloyd, J. R.; Renshaw, J. C.; May, I.; Livens, F. R.; Burke, I. T.; Mortimerc, R. J. G.; Morris, K., Biotransformation of radioactive waste: microbial reduction of actinides and fission products. *J. Nucl. Radiochem. Sci.* **2005,** *6*, 17-20.

183. Rodriguez-Navarro, C.; Rodriguez-Gallego, M.; Ben Chekroun, K.; Gonzalez-Munoz, M. T., Conservation of ornamental stone by Myxococcus xanthus-induced carbonate biomineralization. *Appl Environ Microb* **2003,** *69*, (4), 2182-2193.

184. Martinez, R. J.; Beazley, M. J.; Taillefert, M.; Arakaki, A. K.; Skolnick, J.; Sobecky, P. A., Aerobic uranium(VI) bioprecipitation by metal-resistant bacteria isolated from radionuclide- and metal-contaminated subsurface soils (vol 9, pg 3122, 2008). *Environ Microbiol* **2008,** *10*, (4), 1097-1097.

185. Dohnalkova, A.; Marshall, M. J.; Kennedy*, D. W.; Gorby, Y. A.; Shi, L.; Beliaev, A.; Apkarian, R.; Fredrickson, J. K., The role of bacterial exopolymers in metal sorption and reduction. *Microscopy and Microanalysis* **2005,** *11*, 116.

186. Fayek, M.; Utsunomiya, S.; Pfiffner, S. M.; White, D. C.; Riciputi, L. R.; Ewing, R. C.; Anovitz, L. M.; Stadermann, F. J., The application of HRTEM techniques and nanosims to chemically and isotopically characterize Geobacter sulfurreducens surfaces. *Can Mineral* **2005,** *43*, 1631-1641.

187. Fernandez-Garcia, M.; Martinez-Arias, A.; Hanson, J. C.; Rodriguez, J. A., Nanostructured oxides in chemistry: Characterization and properties. *Chem Rev* **2004,** *104*, (9), 4063-4104.

188. Gilbert, B.; Huang, F.; Zhang, H. Z.; Waychunas, G. A.; Banfield, J. F., Nanoparticles: Strained and stiff. *Science* **2004,** *305*, (5684), 651-654.

189. Singer, D. M.; Farges, F.; Brown, G. E., Biogenic nanoparticulate UO_2: Synthesis, characterization, and factors affecting surface reactivity. *Geochim Cosmochim Ac* **2009,** *73*, (12), 3593-3611.

190. Bernier-Latmani, R.; Veeramani, H.; Vecchia, E. D.; Junier, P.; Lezama-Pacheco, J. S.; Suvorova, E. I.; Sharp, J. O.; Wigginton, N. S.; Bargar, J. R., Non-uraninite Products of Microbial U(VI) Reduction. *Environ Sci Technol* **2010,** *44*, (24), 9456-9462.

191. Fletcher, K. E.; Boyanov, M. I.; Thomas, S. H.; Wu, Q. Z.; Kemner, K. M.; Loffler, F. E., U(VI) Reduction to Mononuclear U(IV) by Desulfitobacterium Species. *Environ Sci Technol* **2010,** *44*, (12), 4705-4709.

192. Veeramani, H.; Alessi, D. S.; Suvorova, E. I.; Lezama-Pacheco, J. S.; Stubbs, J. E.; Sharp, J. O.; Dippon, U.; Kappler, A.; Bargar, J. R.; Bernier-Latmani, R., Products of abiotic U(VI) reduction by biogenic magnetite and vivianite. *Geochim Cosmochim Ac* **2011,** *75*, (9), 2512-2528.

193. Sharp, J. O.; Lezama-Pacheco, J. S.; Schofield, E. J.; Junier, P.; Ulrich, K. U.; Chinni, S.; Veeramani, H.; Margot-Roquier, C.; Webb, S. M.; Tebo, B. M.; Giammar, D. E.; Bargar, J. R.; Bernier-Latmani, R., Uranium speciation and stability after reductive immobilization in aquifer sediments. *Geochim Cosmochim Ac* **2011,** *75*, (21), 6497-6510.

194. Campbell, K. M.; Davis, J. A.; Bargar, J.; Giammar, D.; Bernier-Latmani, R.; Kukkadapu, R.; Williams, K. H.; Veramani, H.; Ulrich, K. U.; Stubbs, J.; Yabusaki, S.; Figueroa, L.; Lesher, E.; Wilkins, M. J.; Peacock, A.; Long, P. E., Composition, stability, and measurement of reduced uranium phases for groundwater bioremediation at Old Rifle, CO. *Appl Geochem* **2011,** *26*, S167-S169.

195. Ray, A. E.; Bargar, J. R.; Sivaswamy, V.; Dohnalkova, A. C.; Fujita, Y.; Peyton, B. M.; Magnuson, T. S., Evidence for multiple modes of uranium immobilization by an anaerobic bacterium. *Geochim Cosmochim Ac* **2011,** *75*, (10), 2684-2695.

196. Sivaswamy, V.; Boyanov, M. I.; Peyton, B. M.; Viamajala, S.; Gerlach, R.; Apel, W. A.; Sani, R. K.; Dohnalkova, A.; Kemner, K. M.; Borch, T., Multiple Mechanisms of Uranium Immobilization by Cellulomonas sp Strain ES6. *Biotechnol Bioeng* **2011,** *108*, (2), 264-276.

197. Boyanov, M. I.; Fletcher, K. E.; Kwon, M. J.; Rui, X.; O'Loughlin, E. J.; Loffler, F. E.; Kemner, K. M., Solution and Microbial Controls on the Formation of Reduced U(IV) Species. *Environ Sci Technol* **2011,** *45*, (19), 8336-8344.

198. Alessi, D. S.; Uster, B.; Veeramani, H.; Suvorova, E. I.; Lezama-Pacheco, J. S.; Stubbs, J. E.; Bargar, J. R.; Bernier-Latmani, R., Quantitative Separation of Monomeric U(IV) from UO2 in Products of U(VI) Reduction. *Environ Sci Technol* **2012,** *46*, (11), 6150-6157.

199. Abdelouas, A.; Lutze, W.; Nuttall, H. E., Oxidative dissolution of uraninite precipitated on Navajo sandstone. *J Contam Hydrol* **1999,** *36*, (3-4), 353-375.

200. Gu, B. H.; Yan, H.; Zhou, P.; Watson, D. B.; Park, M.; Istok, J., Natural humics impact uranium bioreduction and oxidation. *Environ Sci Technol* **2005,** *39*, (14), 5268-5275.

201. Zhong, L. R.; Liu, C. X.; Zachara, J. M.; Kennedy, D. W.; Szecsody, J. E.; Wood, B., Oxidative remobilization of biogenic uranium(IV) precipitates: Effects of iron(II) and pH. *J Environ Qual* **2005,** *34*, (5), 1763-1771.

202. Zhou, P.; Gu, B. H., Extraction of oxidized and reduced forms of uranium from contaminated soils: Effects of carbonate concentration and pH. *Environ Sci Technol* **2005,** *39*, (12), 4435-4440.

203. Moon, H. S.; Komlos, J.; Jaffe, P. R., Uranium reoxidation in previously bioreduced sediment by dissolved oxygen and nitrate. *Environ Sci Technol* **2007,** *41*, (13), 4587-4592.

204. Dispirito, A. A.; Tuovinen, O. H., Uranous Ion Oxidation and Carbon-Dioxide Fixation by Thiobacillus-Ferrooxidans. *Arch Microbiol* **1982,** *133*, (1), 28-32.

205. Duff, M. C.; Hunter, D. B.; Bertsch, P. M.; Amrhein, C., Factors influencing uranium reduction and solubility in evaporation pond sediments. *Biogeochemistry* **1999,** *45*, (1), 95-114.

206. Selenska-Pobell, S.; Kampf, G.; Flemming, K.; Radeva, G.; Satchanska, G., Bacterial diversity in soil samples from two uranium waste piles as determined by rep-APD, RISA and 16S rDNA retrieval. *Anton Leeuw Int J G* **2001,** *79*, (2), 149-161.

207. Senko, J. M.; Istok, J. D.; Suflita, J. M.; Krumholz, L. R., In-situ evidence for uranium immobilization and remobilization. *Environ Sci Technol* **2002,** *36*, (7), 1491-1496.

208. Beller, H. R., Anaerobic, nitrate-dependent oxidation of U(IV) oxide minerals by the chemolithoautotrophic bacterium Thiobacillus denitrificans. *Appl Environ Microb* **2005,** *71*, (4), 2170-2174.

209. Senko, J. M.; Mohamed, Y.; Dewers, T. A.; Krumholz, L. R., Role for Fe(III) minerals in nitrate-dependent microbial U(IV) oxidation. *Environ Sci Technol* **2005,** *39*, (8), 2529-2536.

210. Nedelkova, M.; Merroun, M. L.; Rossberg, A.; Hennig, C.; Selenska-Pobell, S., Microbacterium isolates from the vicinity of a radioactive waste depository and their interactions with uranium. *Fems Microbiol Ecol* **2007,** *59*, (3), 694-705.

211. Frazier, S. W.; Kretzschmar, R.; Kraemer, S. M., Bacterial siderophores promote dissolution of UO2 under reducing conditions. *Environ Sci Technol* **2005,** *39*, (15), 5709-5715.

212. Berner, R. A., *Diagenesis of iron sulfide in recent marine sediments*. Washington: American Association for the Advancement of Science, 1967.

213. Morse, J. W.; Cornwell, J. C., Analysis and Distribution of Iron Sulfide Minerals in Recent Anoxic Marine-Sediments. *Mar Chem* **1987,** *22*, (1), 55-69.

214. Lin, S.; Morse, J. W., Sulfate Reduction and Iron Sulfide Mineral Formation in Gulf of Mexico Anoxic Sediments. *Am J Sci* **1991,** *291*, (1), 55-89.

215. Anthony, J. W.; Bideaux, R. A.; Bladh, K. W.; Nichols, C. M., Eds., Handbook of Mineralogy. In Mineralogical Society of America: Chantilly, VA, USA, pp 20151-1110.

216. Schoonen, M. A. A., Mechanisms of Sedimentary Pyrite Formation. In *Sulfur Biogeochemistry: Past and Present*, Amend, J. P.; Edwards, K. J.; Lyons, T. W., Eds. Geological Society of America: Boulder, CO, USA, 2004; pp 117-134.

217. Rickard, D.; Morse, J. W., Acid Volatile Sulfide (AVS). *Mar Chem* **2005,** *97*, (3-4), 141-197.

218. Morse, J. W.; Arakaki, T., Adsorption and Coprecipitation of Divalent Metals with Mackinawite (FeS). *Geochim Cosmochim Ac* **1993,** *57*, (15), 3635-3640.

219. Berner, R. A., Thermodynamic Stability of Sedimentary Iron Sulfides. *Am J Sci* **1967,** *265*, (9), 773-785.

220. Wilkin, R. T.; Barnes, H. L., Pyrite formation by reactions of iron monosulfides with dissolved inorganic and organic sulfur species. *Geochim Cosmochim Ac* **1996,** *60*, (21), 4167-4179.

221. Rickard, D., Kinetics of FeS precipitation: I. Competing reaction mechanisms. *Geochim Cosmochim Ac* **1995,** *59*, (21), 4367-4379.

222. Schoonen, M. A. A.; Barnes, H. L., Reactions forming pyrite and marcasite from solutions: II. Via FeS precursors below 100℃. *Geochim Cosmochim Ac* **1991,** *55*, (6), 1505-1514.

223. Wang, Q. W.; Morse, J. W., Pyrite formation under conditions approximating those in anoxic sediments: I. Pathway and morphology. *Mar Chem* **1996,** *52*, (2), 99-121.

224. Herbert, R. B.; Benner, S. G.; Pratt, A. R.; Blowes, D. W., Surface chemistry and morphology of poorly crystalline iron sulfides precipitated in media containing sulfate-reducing bacteria. *Chem Geol* **1998,** *144*, (1-2), 87-97.

225. Lennie, A. R.; Vaughan, D. J., Spectroscopic studies of iron sulfide formation and phase relations at low temperatures. In *Mineral spectroscopy: a tribute to Roger G. Burns*, Dyar, M. D.; McCammon, C.; Schaefer, M. W., Eds. The Geochemical Society: St. Louis, Mo, 1996; pp 117-131.

226. Pósfai, M.; Dunin-Borkowski, R. E., Sulfides in biosystems. *Rev Mineral Geochem* **2006,** *61*, 679-714.

227. Lennie, A. R.; Redfern, S. A. T.; Schofield, P. F.; Vaughan, D. J., Synthesis and Rietveld crystal structure refinement of mackinawite, tetragonal FeS. *Mineral Mag* **1995,** *59*, (397), 677-683.

228. Livens, F. R.; Jones, M. J.; Hynes, A. J.; Charnock, J. M.; Mosselmans, J. F. W.; Hennig, C.; Steele, H.; Collison, D.; Vaughan, D. J.; Pattrick, R. A. D.; Reed, W. A.; Moyes, L. N., X-ray absorption spectroscopy studies of reactions of technetium, uranium and neptunium with mackinawite. *J Environ Radioactiv* **2004,** *74*, (1-3), 211-219.

229. Faueque, G., Ecology of Sulfate-Reducing Bacteria. In *Sulfate Reducing Bacteria*, Barton, L. L., Ed. Plenum Press: New York, USA, 1995; pp 217 – 241.

230. Lovley, D. R., Organic-Matter Mineralization with the Reduction of Ferric Iron: A Review. *Geomicrobiol J* **1987,** *5*, (3-4), 375-399.

231. Weber, K. A.; Achenbach, L. A.; Coates, J. D., Microorganisms Pumping Iron: Anaerobic Microbial Iron Oxidation and Reduction. *Nat Rev Microbiol* **2006,** *4*, (10), 752-764.

232. Fredrickson, J. K.; Gorby, Y. A., Environmental Processes Mediated by Iron-Reducing Bacteria. *Curr Opin Biotech* **1996,** *7*, (3), 287-294.

233. Fredrickson, J. K.; Zachara, J. M.; Kennedy, D. W.; Duff, M. C.; Gorby, Y. A.; Li, S. M. W.; Krupka, K. M., Reduction of U(VI) in Goethite (alpha-FeOOH) Suspensions by a Dissimilatory Metal-Reducing Bacterium. *Geochim Cosmochim Ac* **2000,** *64*, (18), 3085-3098.

234. Zachara, J. M.; Fredrickson, J. K.; Smith, S. C.; Gassman, P. L., Solubilization of Fe(III) Oxide-Bound Trace Metals by a Dissimilatory Fe(III) Reducing Bacterium. *Geochim Cosmochim Ac* **2001,** *65*, (1), 75-93.

235. Sani, R. K.; Peyton, B. M.; Amonette, J. E.; Geesey, G. G., Reduction of Uranium(VI) under Sulfate-Reducing Conditions in the Presence of Fe(III)-(Hydr)oxides. *Geochim Cosmochim Ac* **2004,** *68*, (12), 2639-2648.

236. Pyzik, A. J.; Sommer, S. E., Sedimentary Iron Monosulfides - Kinetics and Mechanism of Formation. *Geochim Cosmochim Ac* **1981,** *45*, (5), 687-698.

237. Berner, R. A., Sedimentary Pyrite Formation: An Update. *Geochim Cosmochim Ac* **1984,** *48*, (4), 605-615.

238. Afonso, M. D.; Stumm, W., Reductive Dissolution of Iron(Iii) (Hydr)Oxides by Hydrogen-Sulfide. *Langmuir* **1992,** *8*, (6), 1671-1675.

239. Legall, J.; Payne, W. J.; Chen, L.; Liu, M. Y.; Xavier, A. V., Localization and Specificity of Cytochromes and Other Electron-Transfer Proteins from Sulfate-Reducing Bacteria. *Biochimie* **1994,** *76*, (7), 655-665.

240. Lovley, D. R.; Coates, J. D.; BluntHarris, E. L.; Phillips, E. J. P.; Woodward, J. C., Humic substances as electron acceptors for microbial respiration. *Nature* **1996,** *382*, (6590), 445-448.

241. Reguera, G.; McCarthy, K. D.; Mehta, T.; Nicoll, J. S.; Tuominen, M. T.; Lovley, D. R., Extracellular electron transfer via microbial nanowires. *Nature* **2005,** *435*, (7045), 1098-1101.

242. Turick, C. E.; Tisa, L. S.; Caccavo, F., Melanin production and use as a soluble electron shuttle for Fe(III) oxide reduction and as a terminal electron acceptor by Shewanella algae BrY. *Appl Environ Microb* **2002,** *68*, (5), 2436-2444.

243. Rickard, D. T., Kinetics and Mechanism of Sulfidation of Goethite. *Am J Sci* **1974,** *274*, (8), 941-952.

244. Yao, W. S.; Millero, F. J., Oxidation of hydrogen sulfide by hydrous Fe(III) oxides in seawater. *Mar Chem* **1996,** *52*, (1), 1-16.

245. Poulton, S. W.; Krom, M. D.; Raiswell, R., A revised scheme for the reactivity of iron (oxyhydr)oxide minerals towards dissolved sulfide. *Geochim Cosmochim Ac* **2004,** *68*, (18), 3703-3715.

246. Poulton, S. W., Sulfide oxidation and iron dissolution kinetics during the reaction of dissolved sulfide with ferrihydrite. *Chem Geol* **2003,** *202*, (1-2), 79-94.

247. Banaszak, J. E.; Rittmann, B. E.; Reed, D. T., Subsurface interactions of actinide species and microorganisms: Implications for the bioremediation of actinide-organic mixtures. *J Radioanal Nucl Ch* **1999,** *241*, (2), 385-435.

248. Hua, B.; Deng, B. L., Reductive Immobilization of Uranium(VI) by Amorphous Iron Sulfide. *Environ Sci Technol* **2008,** *42*, (23), 8703-8708.

249. Qafoku, N. P.; Kukkadapu, R. K.; McKinley, J. P.; Arey, B. W.; Kelly, S. D.; Wang, C. M.; Resch, C. T.; Long, P. E., Uranium in Framboidal Pyrite from a Naturally Bioreduced Alluvial Sediment. *Environ Sci Technol* **2009,** *43*, (22), 8528-8534.

250. Hyun, S. P.; Davis, J. A.; Sun, K.; Hayes, K. F., Uranium(VI) Reduction by Iron(II) Monosulfide Mackinawite. *Environ Sci Technol* **2012,** *46*, (6), 3369-3376.

251. Moon, H. S.; Komlos, J.; Jaffe, P. R., Biogenic U(IV) Oxidation by Dissolved Oxygen and Nitrate in Sediment After Prolonged U(VI)/Fe(III)/SO_4^{2-} Reduction. *J Contam Hydrol* **2009,** *105*, (1-2), 18-27.

252. Bi, Y. Q.; Hyun, S. P.; Kukkadapu, R. K.; Hayes, K. F., Oxidative dissolution of UO2 in a simulated groundwater containing synthetic nanocrystalline mackinawite. *Geochim Cosmochim Ac* **2013,** *102*, 175-190.

253. Barton, L. L.; Tomei, F. A., Characteristics and Activities of Sulfate Reducing Bacteria. In *Sulfate Reducing Bacteria*, Barton, L. L., Ed. Plenum Press: New York, USA, 1995; pp 1-24.

254. Pfennig, N.; Biebl, H., The Dissimilatory Sulfur-reducing bacteria. In *The Prokaryotes*, Starr, M. P.; Stolp, H.; Truper, H. G.; Balows, A.; Schlegel, H. G., Eds. Springer: Berlin, Germany, 1981; Vol. 1, pp 941-947.

255. Haag, F.; Reinhard, M.; Mccarty, P. L., Degradation of Toluene and Para-Xylene in Anaerobic Microcosms - Evidence for Sulfate as a Terminal Electron-Acceptor. *Environ Toxicol Chem* **1991,** *10*, (11), 1379-1389.

256. Edwards, E. A.; Wills, L. E.; Reinhard, M.; Grbicgalic, D., Anaerobic Degradation of Toluene and Xylene by Aquifer Microorganisms under Sulfate-Reducing Conditions. *Appl Environ Microb* **1992,** *58*, (3), 794-800.

257. Ensley, B. D.; Suflita, J. M., Metabolism of Environmental Contaminants by Mixed and Pure Cultures of Sulfate-Reducing Bacteria. In *Sulfate Reducing Bacteria*, Barton, L. L., Ed. Plenum Press: New York, USA, 1995; pp 293-326.

258. Anderson, R. T.; Lovley, D. R., Anaerobic bioremediation of benzene under sulfate-reducing conditions in a petroleum-contaminated aquifer. *Environ Sci Technol* **2000,** *34*, (11), 2261-2266.

259. Cunningham, J. A.; Rahme, H.; Hopkins, G. D.; Lebron, C.; Reinhard, M., Enhanced in situ bioremediation of BTEX contaminated groundwater by combined injection of nitrate and sulfate. *Environ Sci Technol* **2001,** *35*, (8), 1663-1670.

260. Anneser, B.; Einsiedl, F.; Meckenstock, R. U.; Richters, L.; Wisotzky, F.; Griebler, C., High-resolution monitoring of biogeochemical gradients in a tar oil-contaminated aquifer. *Appl Geochem* **2008,** *23*, (6), 1715-1730.

261. Foght, J., Anaerobic biodegradation of aromatic hydrocarbons: Pathways and prospects. *J Mol Microb Biotech* **2008,** *15*, (2-3), 93-120.

262. Van Sterripvvoort, D. R.; Millar, K.; Lawrence, J. R., Accumulation of short-chain fatty acids in an aquitard linked to anaerobic biodegradation of petroleum hydrocarbons. *Appl Geochem* **2009,** *24*, (1), 77-85.

263. Compeau, G. C.; Bartha, R., Sulfate-Reducing Bacteria: Principal Methylators of Mercury in Anoxic Estuarine Sediment. *Appl Environ Microb* **1985,** *50*, (2), 498-502.

264. Zehr, J. P.; Oremland, R. S., Reduction of Selenate to Selenide by Sulfate-Respiring Bacteria - Experiments with Cell-Suspensions and Estuarine Sediments. *Appl Environ Microb* **1987,** *53*, (6), 1365-1369.

265. Coleman, M. L.; Hedrick, D. B.; Lovley, D. R.; White, D. C.; Pye, K., Reduction of Fe(III) in Sediments by Sulfate-Reducing Bacteria. *Nature* **1993,** *361*, (6411), 436-438.

266. Dalsgaard, T.; Bak, F., Nitrate Reduction in a Sulfate-Reducing Bacterium, Desulfovibrio-Desulfuricans, Isolated from Rice Paddy Soil - Sulfide Inhibition, Kinetics, and Regulation. *Appl Environ Microb* **1994,** *60*, (1), 291-297.

267. Fude, L.; Harris, B.; Urrutia, M. M.; Beveridge, T. J., Reduction of Cr(VI) by a Consortium of Sulfate-Reducing Bacteria (SRB-III). *Appl Environ Microb* **1994,** *60*, (5), 1525-1531.

268. Lesage, S.; Brown, S.; Hosler, K. R., Degradation of Chlorofluorocarbon-113 under Anaerobic Conditions. *Chemosphere* **1992,** *24*, (9), 1225-1243.

269. Lovley, D. R.; Woodward, J. C., Consumption of Freons CFC-11 and CFC-12 by Anaerobic Sediments and Soils. *Environ Sci Technol* **1992,** *26*, (5), 925-929.

270. Mohn, W. W.; Tiedje, J. M., Microbial Reductive Dehalogenation. *Microbiol Rev* **1992,** *56*, (3), 482-507.

271. Sonier, D. N.; Duran, N. L.; Smith, G. B., Dechlorination of Trichlorofluoromethane (CFC-11) by Sulfate-Reducing Bacteria from an Aquifer Contaminated with Halogenated Aliphatic Compounds. *Appl Environ Microb* **1994,** *60*, (12), 4567-4572.

272. Bagley, D. M.; Sutherland, I. G.; Sleep, B. E., Non-enzymatic degradation of chlorofluorocarbon-113 using cyanocobalamin under anaerobic conditions. *J Environ Eng Sci* **2004,** *3*, (4), 295-299.

273. Noguera, D. R.; Brusseau, G. A.; Rittmann, B. E.; Stahl, D. A., A Unified Model Describing the Role of Hydrogen in the Growth of Desulfovibrio vulgaris under Different Environmental Conditions. *Biotechnol Bioeng* **1998,** *59*, (6), 732-746.

274. Voordouw, G., Carbon monoxide cycling by *Desulfovibrio vulgaris* Hildenborough. *J Bacteriol* **2002,** *184*, (21), 5903-5911.

275. Heidelberg, J. F.; Seshadri, R.; Haveman, S. A.; Hemme, C. L.; Paulsen, I. T.; Kolonay, J. F.; Eisen, J. A.; Ward, N.; Methe, B.; Brinkac, L. M.; Daugherty, S. C.; Deboy, R. T.; Dodson, R. J.; Durkin, A. S.; Madupu, R.; Nelson, W. C.; Sullivan, S. A.; Fouts, D.; Haft, D. H.; Selengut, J.; Peterson, J. D.; Davidsen, T. M.; Zafar, N.; Zhou, L. W.; Radune, D.; Dimitrov, G.; Hance, M.; Tran, K.; Khouri, H.; Gill, J.; Utterback, T. R.; Feldblyum, T. V.; Wall, J. D.; Voordouw, G.; Fraser, C. M., The genome sequence of the anaerobic, sulfate-reducing bacterium Desulfovibrio vulgaris Hildenborough. *Nat Biotechnol* **2004,** *22*, (5), 554-559.

276. Postgate, J. R., Growth of sulfate-reducing bacteria in sulfate-free media. *Research (London)* **1952,** *5*, 189-190.

277. Vosjan, J. H., Respiration and fermentation of the sulfate-reducing bacterium Desulfovibrio desulfuricans in continuous culture. *Plant Soil* **1975,** *43*, 141-152.

278. Bryant, M. P.; Campbell, L. L.; Reddy, C. A.; Crabill, M. R., Growth of Desulfovibrio in Lactate or Ethanol Media Low in Sulfate in Association with H2-Utilizing Methanogenic Bacteria. *Appl Environ Microb* **1977,** *33*, (5), 1162-1169.

279. Fareleira, P.; Legall, J.; Xavier, A. V.; Santos, H., Pathways for utilization of carbon reserves in Desulfovibrio gigas under fermentative and respiratory conditions. *J Bacteriol* **1997,** *179*, (12), 3972-3980.

280. Martin, K. J.; Nerenberg, R., The membrane biofilm reactor (MBfR) for water and wastewater treatment: Principles, applications, and recent developments. *Bioresource technology* **2012,** *122*, 83-94.

281. Lee, K. C.; Rittmann, B. E., A novel hollow-fibre membrane biofilm reactor for autohydrogenotrophic denitrification of drinking water. *Water Sci Technol* **2000,** *41*, (4-5), 219-226.

282. Lee, K. C.; Rittmann, B. E., Applying a novel autohydrogenotrophic hollow-fiber membrane biofilm reactor for denitrification of drinking water. *Water Res* **2002,** *36*, (8), 2040-2052.

283. Rittmann, B. E., The membrane biofilm reactor: the natural partnership of membranes and biofilm. *Water Sci Technol* **2006,** *53*, (3), 219-225.

284. Chung, J.; Nerenberg, R.; Rittmann, B. E., Evaluation for biological reduction of nitrate and perchlorate in brine water using the hydrogen-based membrane biofilm reactor. *J Environ Eng-Asce* **2007,** *133*, (2), 157-164.

285. Chung, J.; Ahn, C. H.; Chen, Z.; Rittmann, B. E., Bio-reduction of N-nitrosodimethylamine (NDMA) using a hydrogen-based membrane biofilm reactor. *Chemosphere* **2008,** *70*, (3), 516-520.

286. Chung, J.; Krajmalnik-Brown, R.; Rittmann, B. E., Bioreduction of trichloroethene using a hydrogen-based membrane biofilm reactor. *Environ Sci Technol* **2008,** *42*, (2), 477-483.

287. Chung, J.; Li, X. H.; Rittmann, B. E., Bio-reduction of arsenate using a hydrogen-based membrane biofilm reactor. *Chemosphere* **2006,** *65*, (1), 24-34.

288. Chung, J.; Nerenberg, R.; Rittmann, B. E., Bio-reduction of soluble chromate using a hydrogen-based membrane biofilm reactor. *Water Res* **2006,** *40*, (8), 1634-1642.

289. Chung, J.; Nerenberg, R.; Rittmann, B. E., Bioreduction of selenate using a hydrogen-based membrane biofilm reactor. *Environ Sci Technol* **2006,** *40*, (5), 1664-1671.

290. Chung, J.; Rittmann, B. E., Bio-reductive dechlorination of 1,1,1-trichloroethane and chloroform using a hydrogen-based membrane biofilm reactor. *Biotechnol Bioeng* **2007,** *97*, (1), 52-60.

291. Chung, J.; Rittmann, B. E., Simultaneous bio-reduction of trichloroethene, trichloroethane, and chloroform using a hydrogen-based membrane biofilm reactor. *Water Sci Technol* **2008,** *58*, (3), 495-501.

292. Chung, J.; Rittmann, B. E.; Wright, W. F.; Bowman, R. H., Simultaneous bio-reduction of nitrate, perchlorate, selenate, chromate, arsenate, and dibromochloropropane using a hydrogen-based membrane biofilm reactor. *Biodegradation* **2007,** *18*, (2), 199-209.

293. Nerenberg, R.; Rittmann, B. E., Hydrogen-based, hollow-fiber membrane biofilm reactor for reduction of perchlorate and other oxidized contaminants. *Water Sci Technol* **2004,** *49*, (11-12), 223-230.

294. Rittmann, B. E.; Chung, J. W.; Wright, W. F.; Bowman, R. H., Remediation of perchlorate and other co-contaminants using the hydrogen-based membrane biofilm reactor. *Abstr Pap Am Chem S* **2005,** *230*, U1548-U1549.

295. Zhao, H. P.; Van Ginkel, S.; Tang, Y. N.; Kang, D. W.; Rittmann, B.; Krajmalnik-Brown, R., Interactions between Perchlorate and Nitrate Reductions in the Biofilm of a Hydrogen-Based Membrane Biofilm Reactor. *Environ Sci Technol* **2011,** *45*, (23), 10155-10162.

296. Ziv-El, M.; Popat, S. C.; Cai, K.; Halden, R. U.; Krajmalnik-Brown, R.; Rittmann, B. E., Managing methanogens and homoacetogens to promote reductive dechlorination of trichloroethene with direct delivery of H2 in a membrane biofilm reactor. *Biotechnol Bioeng* **2012,** *109*, (9), 2200-2210.

297. Rittmann, B. E., The membrane biofilm reactor is a versatile platform for water and wastewater treatment. *Environmental Engineering Research* **2007,** *12*, (4), 157-175.

298. Ontiveros-Valencia, A.; Ilhan, Z. E.; Kang, D.; Rittmann, B. E.; Krajmalnik-Brown, R., Phylogenetic analysis of nitrate- and sulfate-reducing bacteria in a hydrogen-fed biofilm. *FEMS Microbial Ecology* **2013,** *(In press)*.

299. Karamanev, D. G.; Nikolov, L. N.; Mamatarkova, V., Rapid Simultaneous Quantitative Determination of Ferric and Ferrous Ions in Drainage Waters and Similar Solutions. *Miner Eng* **2002,** *15*, (5), 341-346.

300. Cullity, B. D.; Stock, S. R., *Elements of X-ray Diffraction*. 3rd ed.; Prentice Hall: Upper Saddle River, NJ, USA, 2001.

301. Meneses, C. T.; Flores, W. H.; Garcia, F.; Sasaki, J. M., A simple route to the synthesis of high-quality NiO nanoparticles. *J Nanopart Res* **2007,** *9*, (3), 501-505.

302. Hyun, S. P.; Hayes, K. F., Feasibility of using in situ FeS precipitation for TCE degradation. *J Environ Eng-Asce* **2009,** *135*, (10), 1009-1014.

303. Spear, J. R.; Figueroa, L. A.; Honeyman, B. D., Modeling reduction of uranium U(VI) under variable sulfate concentrations by sulfate-reducing bacteria. *Appl Environ Microb* **2000,** *66*, (9), 3711-3721.

304. Sharp, J. O.; Schofield, E. J.; Veeramani, H.; Suvorova, E. I.; Kennedy, D. W.; Marshall, M. J.; Mehta, A.; Bargar, J. R.; Bernier-Latmani, R., Structural Similarities between Biogenic Uraninites Produced by Phylogenetically and Metabolically Diverse Bacteria. *Environ Sci Technol* **2009,** *43*, (21), 8295-8301.

305. Wagner, C. D., *Handbook of X-ray photoelectron spectroscopy*. Perkin-Elmer: Waltham, MA, USA, 1979.

306. Mcintyre, N. S.; Sunder, S.; Shoesmith, D. W.; Stanchell, F. W., Chemical Information From XPS - Applications To the Analysis Of Electrode Surfaces. *J Vac Sci Technol* **1981,** *18*, (3), 714-721.

307. Teterin, Y. A.; Kulakov, V. M.; Baev, A. S.; Nevzorov, N. B.; Melnikov, I. V.; Streltsov, V. A.; Mashirov, L. G.; Suglobov, D. N.; Zelenkov, A. G., A Study Of Synthetic And Natural Uranium-Oxides by X-Ray Photoelectron-Spectroscopy. *Physics And Chemistry Of Minerals* **1981,** *7*, (4), 151-158.

308. Rittmann, B. E.; McCarty, P. L., *Environmental biotechnology : principles and applications*. McGraw-Hill: Boston, 2001; p xiv, 754.

309. Burns, P. C., The Crystal Chemistry of Uranium. *Rev Mineral* <*D*> **1999,** *38*, 23-90.

310. Senko, J. M.; Kelly, S. D.; Dohnalkova, A. C.; McDonough, J. T.; Kemner, K. M.; Burgos, W. D., The effect of U(VI) bioreduction kinetics on subsequent reoxidation of biogenic U(IV). *Geochim Cosmochim Ac* **2007,** *71*, (19), 4644-4654.

311. Komlos, J.; Mishra, B.; Lanzirotti, A.; Myneni, S. C. B.; Jaffe, P. R., Real-time speciation of uranium during active bioremediation and U(IV) reoxidation. *J Environ Eng-Asce* **2008,** *134*, (2), 78-86.

312. Bi, Y.; Hayes, K. F., Nano-FeS inhibits UO2 reoxidation under varied oxic conditions. *Environ Sci Technol* **2014,** *48*, 632-640.

313. Mohagheghi, A.; Updegraff, D. M.; Goldhaber, M. B., The Role of Sulfate-Reducing Bacteria in the Deposition of Sedimentary Uranium Ores. *Geomicrobiol J* **1985,** *4*, (2), 153-173.

314. Ho, C. H.; Miller, N. H., Formation of Uranium Oxide Sols in Bicarbonate Solutions. *J Colloid Interf Sci* **1986,** *113*, (1), 232-240.

315. Kosztolanyi, K.; NGuyen, T. C.; LHote, F.; Vernet, M., Reduction of uranyl complexes and precipitation of uranium oxides by means of hydrogen sulphide gas. *Magy Kem Foly* **1996,** *102*, (4), 180-187.

316. Veeramani, H.; Schofield, E. J.; Sharp, J. O.; Suvorova, E. I.; Ulrich, K. U.; Mehta, A.; Giammar, D. E.; Bargar, J. R.; Bernier-Latmani, R., Effect of Mn(II) on the Structure and Reactivity of Biogenic Uraninite. *Environ Sci Technol* **2009,** *43*, (17), 6541-6547.

317. Tang; Zhou, C.; Van Ginkel, S. W.; Ontiveros-Valencia, A.; Shin, J.; Rittmann, B. E., Hydrogen permeability of the hollow fibers used in H2-based membrane biofilm reactors. *J Membrane Sci* **2012,** *407*, 176-183.

318. Ziv-El, M. C.; Rittmann, B. E., Systematic evaluation of nitrate and perchlorate bioreduction kinetics in groundwater using a hydrogen-based membrane biofilm reactor. *Water Res* **2009,** *43*, (1), 173-181.

319. Ontiveros-Valencia, A.; Ziv-El, M.; Zhao, H. P.; Feng, L.; Rittmann, B. E.; Krajmalnik-Brown, R., Interactions between Nitrate-Reducing and Sulfate-Reducing Bacteria Coexisting in a Hydrogen-Fed Biofilm. *Environ Sci Technol* **2012,** *46*, (20), 11289-11298.

320. Tang, Y.; Zhou, C.; Van Ginkel, S. W.; Ontiveros-Valencia, A.; Shin, J.; Rittmann, B. E., Hydrogen permeability of the hollow fibers used in H-2-based membrane biofilm reactors. *J Membrane Sci* **2012,** *407*, 176-183.

321. Ziv-El, M.; Delgado, A. G.; Yao, Y.; Kang, D. W.; Nelson, K. G.; Halden, R. U.; Krajmalnik-Brown, R., Development and characterization of DehaloR^2, a novel anaerobic microbial consortium performing rapid dechlorination of TCE to ethene. *Appl Microbiol Biot* **2012,** *95*, (1), 273-274.

322. Caporaso, J. G.; Kuczynski, J.; Stombaugh, J.; Bittinger, K.; Bushman, F. D.; Costello, E. K.; Fierer, N.; Pena, A. G.; Goodrich, J. K.; Gordon, J. I.; Huttley, G. A.; Kelley, S. T.; Knights, D.; Koenig, J. E.; Ley, R. E.; Lozupone, C. A.; McDonald, D.; Muegge, B. D.; Pirrung, M.; Reeder, J.; Sevinsky, J. R.; Tumbaugh, P. J.; Walters, W. A.; Widmann, J.; Yatsunenko, T.; Zaneveld, J.; Knight, R., QIIME allows analysis of high-throughput community sequencing data. *Nat Methods* **2010,** *7*, (5), 335-336.

323. Price, M. N.; Dehal, P. S.; Arkin, A. P., FastTree: Computing Large Minimum Evolution Trees with Profiles instead of a Distance Matrix. *Mol Biol Evol* **2009,** *26*, (7), 1641-1650.

324. Spurr, A. R., A Low-Viscosity Epoxy Resin Embedding Medium for Electron Microscopy. *J Ultra Mol Struct R* **1969,** *26*, (1-2), 31-43.

325. Wu, C. G.; Zhang, G. S.; Liu, X. L.; Dong, X. Z., Bicarbonate is a stimulus in the inter-species induced sporulation of strict anaerobic Syntrophomonas erecta subsp sporosyntropha. *Extremophiles* **2007,** *11*, (6), 827-832.

326. Gillan, D. C.; DeRidder, C., Morphology of a ferric iron-encrusted biofilm forming on the shell of a burrowing bivalve (Mollusca). *Aquat Microb Ecol* **1997,** *12*, (1), 1-10.

327. Brown, D. A.; Beveridge, T. J.; Keevil, C. W.; Sheriff, B. L., Evaluation of microscopic techniques to observe iron precipitation in a natural microbial biofilm. *Fems Microbiol Ecol* **1998,** *26*, (4), 297-310.

328. Permpoonpattana, P.; Tolls, E. H.; Nadem, R.; Tan, S.; Brisson, A.; Cutting, S. M., Surface Layers of Clostridium difficile Endospores. *J Bacteriol* **2011,** *193*, (23), 6461-6470.

329. Hofstetter, S.; Denter, C.; Winter, R.; McMullen, L. M.; Ganzle, M. G., Use of the fluorescent probe LAURDAN to label and measure inner membrane fluidity of endospores of Clostridium spp. *J Microbiol Meth* **2012,** *91*, (1), 93-100.

330. Yang, W. W.; Crow-Willard, E. N.; Ponce, A., Production and characterization of pure Clostridium spore suspensions. *J Appl Microbiol* **2009,** *106*, (1), 27-33.

331. Dalla Vecchia, E. C.; Veeramani, H.; Suvorova, E. I.; Wigginton, N. S.; Bargar, J. R.; Bernier-Latmani, R., U(VI) reduction by spores of Clostridium acetobutylicum. *Research In Microbiology* **2010,** *161*, (9), 765-771.

332. Ontiveros-Valencia, A.; Ilhan, Z. E.; Kang, D. W.; Rittmann, B.; Krajmalnik-Brown, R., Phylogenetic analysis of nitrate- and sulfate-reducing bacteria in a hydrogen-fed biofilm. *Fems Microbiol Ecol* **2013,** *85*, (1), 158-167.

333. Zhao, H. P.; Ontiveros-Valencia, A.; Tang, Y. N.; Kim, B. O.; Ilhan, Z. E.; Krajmalnik-Brown, R.; Rittrnann, B., Using a Two-Stage Hydrogen-Based Membrane Biofilm Reactor (MBfR) to Achieve Complete Perchlorate Reduction in the Presence of Nitrate and Sulfate. *Environ Sci Technol* **2013,** *47*, (3), 1565-1572.

334. Martins, M.; Faleiro, M. L.; Chaves, S.; Tenreiro, R.; Costa, M. C., Effect of uranium (VI) on two sulphate-reducing bacteria cultures from a uranium mine site. *Sci Total Environ* **2010,** *408*, (12), 2621-2628.

335. Williams, K. H.; Bargar, J. R.; Lloyd, J. R.; Lovley, D. R., Bioremediation of uranium-contaminated groundwater: a systems approach to subsurface biogeochemistry. *Curr Opin Biotech* **2013,** *24*, (3), 489-497.

336. Bargar, J. R.; Williams, K. H.; Campbell, K. M.; Long, P. E.; Stubbs, J. E.; Suvorova, E. I.; Lezama-Pacheco, J. S.; Alessi, D. S.; Stylo, M.; Webb, S. M.; Davis, J. A.; Giammar, D. E.; Blue, L. Y.; Bernier-Latmani, R., Uranium redox transition pathways in acetate-amended sediments. *P Natl Acad Sci USA* **2013,** *110*, (12), 4506-4511.

337. Gihring, T. M.; Zhang, G. X.; Brandt, C. C.; Brooks, S. C.; Campbell, J. H.; Carroll, S.; Criddle, C. S.; Green, S. J.; Jardine, P.; Kostka, J. E.; Lowe, K.; Mehlhorn, T. L.; Overholt, W.; Watson, D. B.; Yang, Z. M.; Wu, W. M.; Schadt, C. W., A Limited Microbial Consortium Is Responsible for Extended Bioreduction of Uranium in a Contaminated Aquifer. *Appl Environ Microb* **2011,** *77*, (17), 5955-5965.

338. Boonchayaanant, B.; Nayak, D.; Du, X.; Criddle, C. S., Uranium reduction and resistance to reoxidation under iron-reducing and sulfate-reducing conditions. *Water Res* **2009,** *43*, (18), 4652-4664.

339. Sokolova, T. G.; Gonzalez, J. M.; Kostrikina, N. A.; Chernyh, N. A.; Slepova, T. V.; Bonch-Osmolovskaya, E. A.; Robb, F. T., Thermosinus carboxydivorans gen. nov., sp nov., a new anaerobic, thermophilic, carbon-monoxide-oxidizing, hydrogenogenic bacterium from a hot pool of Yellowstone National Park. *Int J Syst Evol Micr* **2004,** *54*, 2353-2359.

340. Junier, P.; Frutschi, M.; Wigginton, N. S.; Schofield, E. J.; Bargar, J. R.; Bernier-Latmani, R., Metal reduction by spores of Desulfotomaculum reducens. *Environ Microbiol* **2009,** *11*, (12), 3007-3017.

341. Wiegel, J.; Tanner, R.; Rainey, F. A., An introduction to the family Clostridiaceae. In *The Prokaryotes, Vol. 6 - Proteobacteria: Gamma Subclass*, Dworkin, M. e., Ed. Springer: USA, 2006; Vol. 6, pp 654-678.

342. Zellner, G.; Neudorfer, F.; Diekmann, H., Degradation of lactate by an anaerobic mixed culture in a fluidized-bed reactor. *Water Res* **1994,** *28*, (6), 1337-1340.

343. Wilkin, R. T.; Barnes, H. L., Formation processes of framboidal pyrite. *Geochim Cosmochim Ac* **1997,** *61*, (2), 323-339.

344. Gramp, J. P.; Bigham, J. M.; Jones, F. S.; Tuovinen, O. H., Formation of Fe-sulfides in cultures of sulfate-reducing bacteria. *J Hazard Mater* **2010,** *175*, (1-3), 1062-1067.

345. McGowan, G.; Prangnell, J., The significance of vivianite in archaeological settings. *Geoarchaeology* **2006,** *21*, (1), 93-111.

346. Schwertmann, U.; Cornell, R. M., *Iron Oxides in the Laboratory*. Verlagsgesellschaft: Weinheim, Germany 1991.

347. Tang, Y. N.; Zhou, C.; Ziv-El, M.; Rittmann, B. E., A pH-control model for heterotrophic and hydrogen-based autotrophic denitrification. *Water Res* **2011,** *45*, (1), 232-240.

348. Snoeyink, V. L.; Jenkins, D., *Water chemistry*. Wiley: New York, 1980; p xiii, 463 p.

349. Li, Y. L.; Vali, H.; Yang, J.; Phelps, T. J.; Zhang, C. L., Reduction of Iron Oxides Enhanced by a Sulfate-Reducing Bacterium and Biogenic H2S. *Geomicrobiol J* **2006,** *23*, (2), 103-117.

350. Lennie, A. R.; England, K. E. R.; Vaughan, D. J., Transformation of Synthetic Mackinawite to Hexagonal Pyrrhotite - a Kinetic-Study. *Am Mineral* **1995,** *80*, (9-10), 960-967.

351. Ohfuji, H.; Rickard, D., High resolution transmission electron microscopic study of synthetic nanocrystalline mackinawite. *Earth Planet Sc Lett* **2006,** *241*, (1-2), 227-233.

352. Wolthers, M.; Van der Gaast, S. J.; Rickard, D., The structure of disordered mackinawite. *Am Mineral* **2003,** *88*, (11-12), 2007-2015.

353. Rickard, D. T., Kinetics and Mechanism of Pyrite Formation at Low-Temperatures. *Am J Sci* **1975,** *275*, (6), 636-652.

354. Luther, G. W., Pyrite Synthesis Via Polysulfide Compounds. *Geochim Cosmochim Ac* **1991,** *55*, (10), 2839-2849.

355. Blumentals, I. I.; Itoh, M.; Olson, G. J.; Kelly, R. M., Role of Polysulfides in Reduction of Elemental Sulfur by the Hyperthermophilic Archaebacterium Pyrococcus-Furiosus. *Appl Environ Microb* **1990,** *56*, (5), 1255-1262.

356. Toniazzo, V.; Mustin, C.; Portal, J. M.; Humbert, B.; Benoit, R.; Erre, R., Elemental sulfur at the pyrite surfaces: speciation and quantification. *Appl Surf Sci* **1999,** *143*, (1-4), 229-237.

357. Butler, I. B.; Bottcher, M. E.; Rickard, D.; Oldroyd, A., Sulfur isotope partitioning during experimental formation of pyrite via the polysulfide and hydrogen sulfide pathways: implications for the interpretation of sedimentary and hydrothermal pyrite isotope records. *Earth Planet Sc Lett* **2004,** *228*, 495-509.

358. Ferguson, J. F.; Jenkins, D.; Eastman, J., Calcium Phosphate Precipitation at Slightly Alkaline pH Values. *J Water Pollut Con F* **1973,** *45*, (4), 620-631.

359. Ferguson, J. F.; Mccarty, P. L., Effects of Carbonate and Magnesium on Calcium Phosphate Precipitation. *Environ Sci Technol* **1971,** *5*, (6), 534-&.

360. Martens, C. S.; Harriss, R. C., Inhibition of Apatite Precipitation in Marine Environment by Magnesium Ions. *Geochim Cosmochim Ac* **1970,** *34*, (5), 621-&.

361. Hansen, H. C. B.; Poulsen, I. F., Interaction of synthetic sulphate "Green rust" with phosphate and the crystallization of vivianite. *Clay Clay Miner* **1999,** *47*, (3), 312-318.

362. Zegeye, A.; Huguet, L.; Abdelmoula, M.; Carteret, C.; Mullet, M.; Jorand, F., Biogenic hydroxysulfate green rust, a potential electron acceptor for SRB activity. *Geochim Cosmochim Ac* **2007,** *71*, (22), 5450-5462.

363. Nriagu, J. O., Stability of Vivianite and Ion-Pair Formation in System Fe3(PO4)2-H3PO4-H_2O. *Geochim Cosmochim Ac* **1972,** *36*, (4), 459-&.

364. Postma, D., Occurrence and Chemical Composition of Recent Fe-Rich Mixed Carbonates in a River Bog. *J Sediment Petrol* **1977,** *47*, (3), 1089-1098.